AD-A243 894

‖‖‖‖‖‖‖‖‖‖‖‖

DTIC
ELECTE
JAN 0 3 1992
S D
D

TENSILE STRENGTH CHARACTERIZATION
OF A METAL MATRIX COMPOSITE
WITH CIRCULAR HOLES

THESIS

Jeffrey Rattray
Captain, USAF

AFIT/GAE/ENY/91D-24

92-00102

‖‖‖‖‖‖‖‖‖‖‖‖

Approved for public release; distribution unlimited

92 1 2 092

TENSILE STRENGTH CHARACTERIZATION OF A

METAL MATRIX COMPOSITE WITH CIRCULAR HOLES

THESIS

Presented to the Faculty of the School of Engineering

of the Air Force Institute of Technology

Air University

In Partial Fulfillment of the

Requirements for the Degree of

Master of Science in Aeronautical Engineering

Jeffrey Rattray

Captain, USAF

December 1991

Accesion For	
NTIS CRA&I	☑
DTIC TAB	☐
Unannounced	☐
Justification	
By	
Dist.ibutio../	
Availability Codes	
Dist	Avaii a..d/or Special
A-1	

Approved for public release; distribution unlimited

Preface

This study investigated the tensile strength and
failure characteristics of a metal matrix composite with
holes of different sizes. This area had not been explored
by anyone and I have always enjoyed breaking things.
Current plans call for using this material as the skin for
the National Aerospace Plane and joining panels with rivets.
This was an opportunity to break things, contribute to the
space program, and fulfill a requirement for a degree all at
the same time.

Many people helped me through this project and I'd like
to thank a few of them. Dr. Ted Nicholas and Dr. James
Larsen of the Materials Directorate of Wright Laboratory
provided the background about SCS-6/Beta 21S. The reading
material helped, but their willingness to answer questions
when I dropped in or called helped even more. Thanks to Dr.
Shankar Mall who advised me in the truest sense of the word.
Without your effort to keep me focused I would have learned
a little about a lot of things, but never would have
completed any of them. Finally, special thanks to my wife
Jane who listened to and cared for me during this time.
Thanks for taking over all the work of caring for Jessica,
Joni, and Janelle while I broke composites.

<div align="right">Jeffrey Rattray</div>

Table of Contents

iii

List of Figures

List of Tables

List of Symbols

A_{ij}	Elements of the stiffness matrix for a laminate
Al	Aluminium
D/W	Diameter to width ratio
dB	Decibel
E	Young's modulus or stiffness
E_1	Stiffness of a lamina in the fiber direction
E_2	Stiffness of a lamina transverse to the fibers
E_f	Stiffness of the fibers
E_m	Stiffness of the matrix
E_y	Stiffness of a laminate in load direction
G	Shear modulus
G_{12}	Shear modulus of a lamina
K_t	Stress concentration factor
Mo	Molybdenum
Nb	Niobium
Si	Silicon
SCF	Stress concentration factor
Ti	Titanium
V_m	Volume fraction for the matrix
V_f	Volume fraction for the fiber
0° fiber	Fiber in the load direction
ν	Poisson's ratio
ν_f	Poisson's ratio for the fibers
ν_m	Poisson's ratio for the matrix

ν_{12} Effective Poisson's ratio of lamina

ξ Fiber reinforcement measure in Halpin-Tsai

ABSTRACT

Static tensile testing conducted at room temperature and 650°C shows notch sensitivity for a quasi-isotropic lay-up of a titanium alloy metal matrix composite. The specific material used was SCS-6/Beta 21S. Some unnotched specimens were tested and then the diameter-to-width ratio was varied from 0.1 to 0.4. The room temperature unnotched strength is 840 MPa, and the strength falls to less than half this value at 650°C. The off-axis plies of the $[0,\pm45,90]_s$ lay-up exhibit debonding of the fibers from the matrix at only ten percent of failure stress. This debonding is shown with acetate replicas and acoustic emission. By modeling the debonded plies with the Halpin-Tsai equations, a modulus is calculated for the debonded material which correlates very well with the experimental modulus. A fiber dominated failure exists at both temperatures, but the fiber pullout exists only at 650°C. Etching away the matrix from the 0° fibers showed a small area near the hole where fibers were damaged. The size of this damage zone correlated very well with the critical distance for the Whitney-Nuismer Point Stress failure prediction method.

TENSILE STRENGTH CHARACTERIZATION OF A
METAL MATRIX COMPOSITE WITH CIRCULAR HOLES

I. Introduction

Tensile strength and failure modes are a major consideration for metal matrix composites (MMCs) with holes. Drilling holes in any material reduces the strength, but the amount of reduction varies with the material. The decrease in tensile strength of composite materials can be drastic and as new materials are evaluated, the notched strength must be determined. The notched strength of a new MMC called SCS-6/Beta 21S is evaluated in this study. This new MMC is a candidate material for the skin of the National Aerospace Plane. In addition the understanding of failure progression at the hole may allow designers to deal more effectively with the reduction in failure strength caused by holes.

The renewed interest in metal matrix composites comes from a desire for low density materials which can handle high stresses at elevated temperatures. The failure strength of some unidirectional metal matrix composites is reduced by only one fifth when the temperature is raised from room temperature to $650^{O}C$ (1). A large program to evaluate the properties of SCS-6/Beta 21S is now in progress

by the National Aerospace Plane Consortium, but one of many properties yet to be addressed is the reduction in strength which results when circular holes are drilled in the material.

Placing holes in a composite can drastically impact failure strength. Brittle materials like graphite-epoxy experience a reduction in strength of more than fifty percent when notches are created, but it is not known how notches will affect the strength of SCS-6/Beta 21S.

Therefore, in this study a quasi-isotropic lay-up of SCS-6/Beta 21S is tested with different hole diameters to provide this information. Since the material is intended for use at elevated temperatures, tests are conducted at 650°C as well as room temperature. The failure progression caused by the hole is also investigated. This research provides data necessary for using this new material for the requirements outlined below.

Background

High Strength-to-Weight Materials Requirement.
Hypersonic flight and radical increases in thrust-to-weight ratio of gas turbine engines require high strength-to-weight ratio materials. For these applications composites must maintain this strength at high temperatures.

Orbiting hypersonic flight will not be attained without an aircraft skin of much higher strength-to-weight than current aerospace materials. The Integrated High Performance Turbine Engine Technology Initiative (IHPTET) has set a goal of doubling the thrust-to-weight ratio of jet engines by the year 2000. While increases in thrust are possible, drastic reductions in component mass must take place to meet this requirement (1).

Metal Matrix Composites. One type of material being looked at for these applications is the metal matrix composite. Boron/aluminum composites were investigated several years ago, but never received widespread use. Since the strength of aluminum decreases rapidly as temperature exceeds 260°C, it is not an attractive candidate for these applications. Many alloys have been formed with titanium and aluminum as the primary elements and examined for potential as a matrix with silicon-carbide fibers. These fibers possess almost constant strength up to 650°C (2). At this temperature, a titanium aluminide MMC with all the fibers in one direction exhibits twice the strength-to-weight ratio of any isotropic material in use (3). Several titanium aluminide alloys have been tried and Titanium 15-3 was investigated as a candidate for the skin of hypersonic flight vehicles. This testing revealed a low resistance to oxidation at higher temperatures and prompted the

development of Beta 21S for NASP. Beta 21S has high strength at up to 650°C and shows excellent oxidation resistance (4).

Unfortunately, the fiber matrix interface and residual stresses are problems with titanium aluminides. The interface between the fibers and the matrix in most composites is very strong. The interface in SCS-6/Ti-15-3 was shown to be very weak in the off-axis plies (5). Stresses as low as twenty percent of failure stress debond the fibers from the matrix and the off-axis plies lose much of their stiffness and strength. Many titanium-aluminide silicon-carbide composites, including Beta 21S, are formed using hot isostatic pressing (HIP). The difference in the coefficient of thermal expansion of the fibers and matrix creates residual stresses in the material when cooled to room temperature. With SCS-6 fibers and a Beta 21S matrix this puts the fibers in compression and the matrix in tension. The matrix then yields at a lower load.

Though the name is usually shortened to Beta 21S, the titanium alloy matrix used here is Ti-15Mo-2.7Nb-0.2Si-3Al by percent volume (4). SCS-6 is a particular silicon carbide fiber with a diameter of 142 microns. These materials have been combined to create the material SCS-6/Beta 21S for use in intermediate temperature ranges. This work investigates the tensile strength and failure modes of

SCS-6/Beta 21S at room temperature and 650°C when various

hole sizes are created.

II. Literature Review and Theory

A review of the literature and a theoretical summary make up this section. The background specific to the material under investigation was addressed in Chapter I and here the view is far more general. A review of pertinent MMC studies and a summary of applicable concepts from laminated plate theory are provided to help the reader follow later discussions.

Literature Review

Failure strength of notched materials is related to an elevation of stress and thus strain near the notch. This is referred to as a stress or strain concentration. Much of the literature addresses how the stress concentration around the hole is related to failure strength.

Isotropic Materials. Stress concentration around a hole and strength reduction due to the hole is characterized well for many materials. Timoshenko showed that for any isotropic material the stress at $\theta = \pi/2$ from the top of the hole is three times greater than the far field tensile stress for an infinite plate. He also established that at $\theta = 0$ a compressive stress exists equal in magnitude to the far field tensile stress (6).

Orthotropic Materials. For orthotropic materials the maximum stress can vary widely, as shown by Lekhnitskii. He

6

developed equations for the stress distribution around the hole in a lamina for an infinite plate (7). Greszczuk extended this to plate theory and further developed methods for predicting stress concentrations around the hole. He also compared the stress concentrations of several different unidirectional composites. They showed many different values for the highest stress concentration with the greatest value of nine given by graphite-epoxy (8).

Metal Matrix Composites. Since titanium aluminide MMCs are relatively new, little work is available. Research linked to the IHPTET has created some data for fatigue and thermal cycling along with tensile testing. A search of the literature found very limited static tensile testing of titanium aluminides with open holes and some work done with boron/aluminum several years ago.

The boron/aluminum material parallels SCS-6/Beta 21S in that the matrix is much more ductile than the fibers. Heat treatment of the matrix can reduce this difference in ductility, but for our tests the material was stressed in the as received condition. In the as received condition Beta 21S fails at twenty times the failure strain of the SCS-6 fibers.

Mar and Lin found that boron/aluminum composites were sensitive to the presence of notches, but that the size of the notch, not the shape, dominated. They note that the

specimens fail catastrophically and no visible damage
precedes ultimate failure (9). After testing five different
lay-ups of boron/aluminum, Poe and Sova concluded that the
strength was almost entirely a function of the fibers in the
principal load carrying direction. They developed a failure
theory using a strain concentration factor, which worked
well in predicting failure stresses even in nonlinear
materials (10). Johnson agreed with Mar and Lin concerning
lack of effect of the shape of the notch in boron/aluminum.
Johnson's work goes on to state that laminate failure
occurred soon after the first fiber failure. Fiber failure
was detected by acoustic emission as well as examining
specimens which were loaded to portions of failure stress
and then destructively evaluated (11).

Johnson also tested a titanium aluminide composite
called SCS-6/Ti-15-3 in fatigue, and did a few static tests
to verify the fatigue results. His work shows a debonding
of the fibers from the matrix at only twenty percent of
failure stress. He demonstrated this characteristic of the
material using an acetate replica technique (5). During
fatigue research work using Ti-15-3 with an open hole, Naik
and Johnson tested a few specimens to failure statically.
All holes were the same size and the failure mechanism was
not investigated for the static case (12).

Terminology. The literature contained several different methods for distinguishing between the region containing the hole and the rest of the specimen. The terms net section area and notched area were both used to describe the cross section containing the hole. The rest of the specimen was referred to as the unnotched or remote area. Throughout this document the terms local, section, and notched stress will be used to mean the stress computed by dividing this reduced area into the load. The notched area is computed by subtracting the diameter of the hole from the specimen width and then multiplying the result by the thickness. The remote stress or unnotched stress is simply the load divided by the product of the width and the thickness. When no distinction is made, the stress or strain can be assumed to mean the unnotched value.

The research detailed herein addresses the reduction in strength induced by creating various diameter to width ratios using circular open holes. The impact of varying the ratio of hole size to specimen width was not addressed for MMCs in any of the previous reports.

Theory

The theoretical basis for the comparison of results and failure prediction methods is based on laminated plate theory. The assumptions used in laminated plate theory are reviewed here along with a brief summary of the process used

to predict laminate properties on a macromechanical scale. The micromechanical ideas of volume fraction and the theories of laminate properties proposed by Halpin and Tsai are examined as well.

Laminated Plate Theory. The earliest structural material which can be considered orthotropic was wood. The prediction of laminated wood or plywood strength led to the development of classical laminated plate theory. Whenever this theory is applied, perfect bonding between thin lamina is assumed. The laminate stiffnesses are based on the initial stiffness of the material in each ply so when the stiffness of any ply changes the stiffness of the laminate changes. Failure prediction methods which rely on the initial laminate stiffness would then be successful in predicting the failure of brittle materials, but questionable for any material where the stiffness changed well before failure. Jones and others present the method for calculating the laminate properties, but a few specific properties of the SCS-6/Beta 21S lay-up used for these tests will be reviewed (13).

The $[0,\pm45,90]_s$ laminate used here has four special characteristics, which simplify the calculation of laminate properties. This lay-up is symmetric, balanced, regular, and quasi-isotropic. An orthotropic lamina, which is loaded in tension with fixed grips, sometimes realizes internal

stresses not seen in isotropic materials. When the fibers are not aligned with the load the orthotropic properties create these stresses. Special configurations of laminates cancel the forces which create this effect and cause the plate to behave more like an isotropic material. This laminate can be stressed in along any of the fiber directions and show the same properties. If stressed at some angle between $0°$ and $45°$ to the closest fibers, it will behave only slightly differently than an isotropic material. This then is a very special composite designed to act like an isotropic material, but provide high strength at high temperature.

Micromechanics. Considering the micromechanics of a composite enables approximation of properties when the material is not well characterized. Halpin and Tsai developed a set of equations which predict the properties of lamina using the properties of the fibers and the matrix (14). Later the moduli of nonlinear SCS-6/Beta 21S will be modeled using the ideas of Halpin and Tsai. Central to the use of these equations is the concept of the volume fraction.

Continuous fiber composite materials have the stiffness and strength of the fibers and the matrix. The fiber volume fraction(V_f) is simply the portion of the material occupied by the fibers. The remainder of the material is assumed to

be taken up by the matrix so that the sum of the matrix volume fraction(V_m) and V_f is always one. Several techniques exist for calculating V_f and a rectangular representative volume element was chosen for this research. The cell contains one circular fiber and the dimensions of the rectangle are determined by the fiber spacing and the lamina thickness. Figure 1 shows a rectangular volume element.
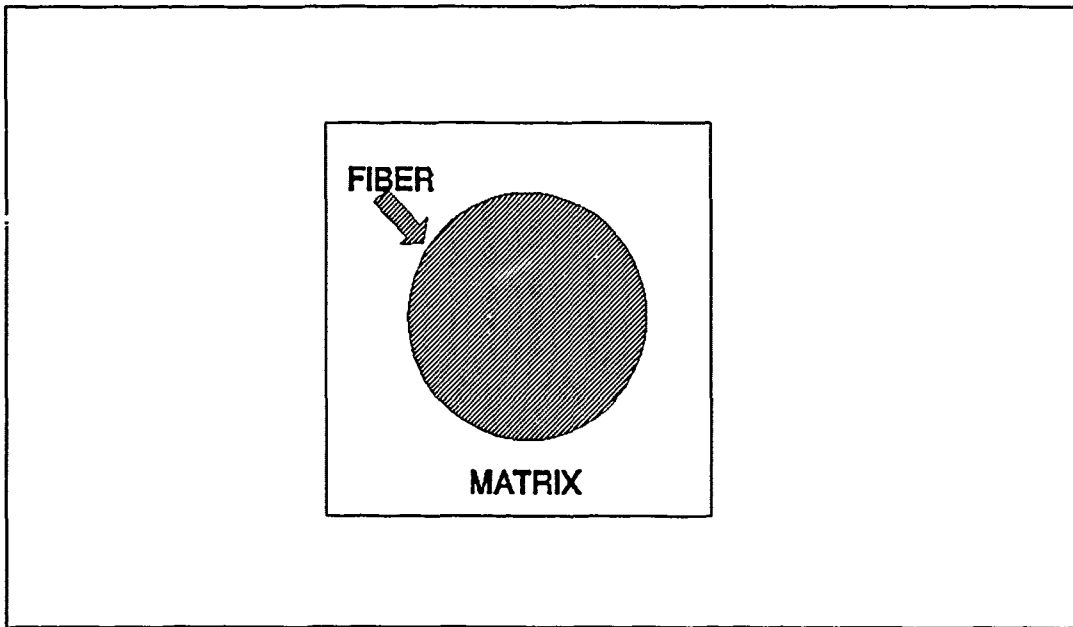
Figure 1   Representative Volume Element

As with other materials concepts, volume fraction calculations require assumptions about the composite. The fibers and matrix are assumed to be homogeneous, elastic, and isotropic. Exact alignment and spacing are also required of the fibers. Jones lists other stipulations for the material including perfect bonding of the matrix and

fibers (13). When these criteria are not met the solutions may not be valid.

Halpin-Tsai Equations. Halpin and Tsai used volume fractions to calculate the moduli of lamina based on the volume fractions and the moduli of the fibers and matrix. The first two equations are the same as the traditional rule of mixtures calculations.

$$E_1 = E_f V_f + E_m V_m \tag{1}$$

This equation gives the upper bound for stiffness in the direction of the fibers. The same type of calculation gives a value for ν_{12}.

$$\nu_{12} = \nu_f V_f + \nu_m V_m \tag{2}$$

The traditional rule of mixtures calculations had separate developments to produce the other moduli. Halpin and Tsai used an interpolation technique to generate all the moduli beyond E_1 and ν_{12} with a single equation (13). Not only did this reduce the abundance of equations in micromechanics, it provided a new means for modeling some behaviors in composites. The remaining moduli are calculated using

$$\frac{M}{M_m} = \frac{1 + \xi \eta V_f}{1 - \eta V_f} \tag{3}$$

13

where M_m represents the modulus of the matrix which corresponds to the lamina modulus being calculated. ξ represents the degree of fiber reinforcement for a composite. The symbol η is given by

$$\eta = \frac{(M_f/M_m) - 1}{(M_f/M_m) + \xi} \qquad (4)$$

where Mf is the fiber modulus corresponding to the lamina modulus being calculated. The value of ξ is chosen based on the type of cross section used in calculating the volume fraction.

Applying these equations yields very acceptable results and reduces the complexity of the micromechanical approach. The adjustment of constituent stiffnesses allows modeling of some changes to the material.

III. Experimental Procedure

This study was conducted using the facilities of the Air Force Institute of Technology (AFIT) with some assistance from Wright Laboratory (WL). The testing took place at AFIT, but portions of specimen preparation and examination were accomplished through equipment and personnel of WL. This section discusses specimen preparation, outlines the test set-up and procedures for conducting the tests, and describes the techniques for the various methods of post-test analysis. In cases where procedures differ for room temperature and elevated temperature tests, a separate section addresses each.

Note that all tests conducted here used SCS-6/Beta 21S with the material in the as delivered condition. Beta 21S was developed to enable the properties of ductility and stiffness to be tailored through aging. Since the specific use motivates the choice of these properties, it was decided that this study would collect data for the as-delivered material. All elevated temperature tests were completed within 30 minutes to reduce the potential for unintentional aging.

Specimen Preparation

Specimen preparation for all tests involved cutting to size

15

and drilling holes. For room temperature tests it was also
necessary to apply tabs and strain gages, and in some cases
polish the edges to enable the taking of edge replicas.

Each specimen was cut to a length of 15.4 cm and width
of 1.27 cm using diamond impregnated blades. The plate was
cut such that the plies with the fibers in the loading
direction were the outside plies of each specimen. Less
than 2 percent variation was found in the dimensions of the
coupons.

Holes were formed using a Bendix ultrasonic drill. A
rod slightly smaller than the desired hole size was soldered
to an appropriately sized mandrel. After gluing the coupon
to a half centimeter thick glass plate, a thin glass cover
slip was glued over the top surface to reduce any extra
chipping of the matrix. The rod and mandrel were attached
to the mechanism. A powerful amplifier then vibrated the
specimen as the frequency was adjusted to create resonance.
A slurry of boron-carbide particles poured on the cover slip
worked between the rod and the specimen to slowly drill a
very smooth hole. In no case was the failure of a specimen
seen to occur at a point far from the predicted highest
tensile stress point. This indicates that no large cracks
with unwanted stress concentrations were created by this
drilling technique. Figure 2 contains two photographs. The
top photograph shows a typical ultrasonically drilled hole.

16

The other shows the actual surface inside the hole and was taken using electron microscopy. The surface shows no large scratches and a very smooth texture.

Preparation Specific to Room Temperature Coupons. Fiberglass tabs and strain gages were applied to room temperature specimens.

To show the debonding of the fibers from the matrix the edge of some specimens were ground flat and polished.

To distribute the stress created by the grips on the specimen, fiberglass tabs were applied. The tab material was a continuous glass fiber crossweave in a phenolic sheet. The tab length and gripping distance was 2.54 cm with the last 0.5 cm toward the center of the specimen beveled to further distribute the stress. The thickness was 1.6 mm. After applying solvent, the Beta 21S was sanded and the plastic roughened to ensure a sound bond. Tabs were applied with epoxy and cured at 78°C for two hours. No specimen failed at the grips nor did any tabs slide off during the testing so this bonding technique is very effective for this matrix.

Two strain gages were used to measure tensile strain for the room temperature tests. A Micromeasurements CEA-06-032UW-120 gage was mounted close to the hole. This has a gage length of 0.8 mm, a gage factor of 2.05, and a resistance of 120 ohms. A 350 ohm gage with a gage length
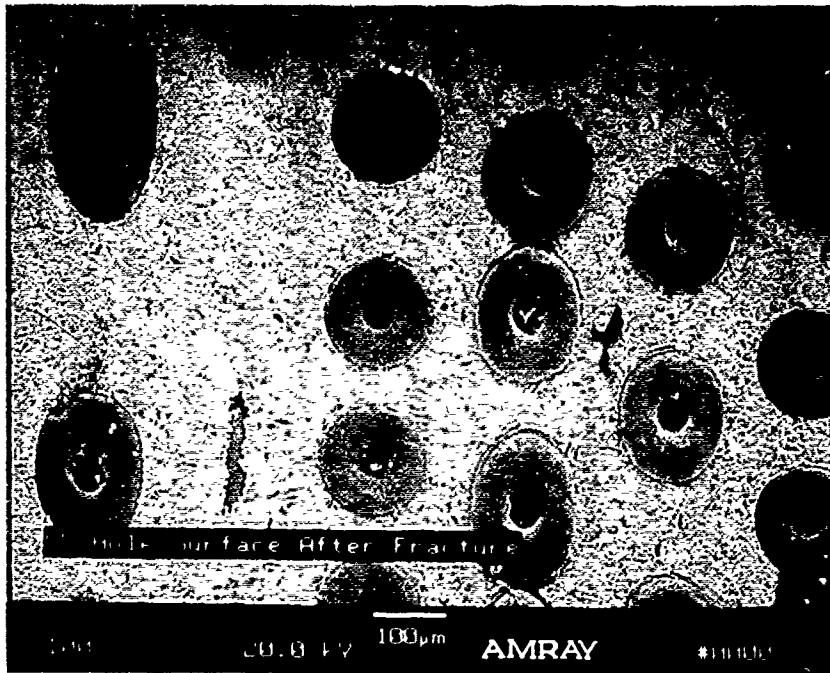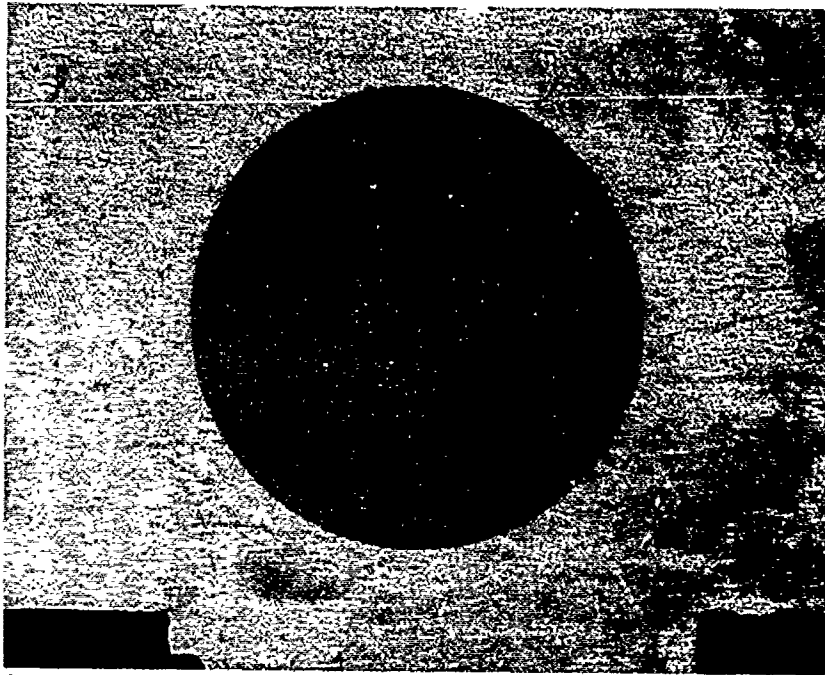
Figure 2 Typical Hole Shape

18

of 6.4 mm was located over two hole diameters away from the expected failure zone. This Micromeasurements CEA-03-250UW-350 has a gage factor of 2.075 and provided remote strain data. While the entire effect of the stress concentration created by the hole can only be seen by placing a gage on the surface inside the hole, some increase in strain could be seen with the local gage. Removing the extra foil nearest the hole allowed the placement of the gage less than 1 mm from the hole edge. Both gages were affixed using standard techniques. Figure 3 shows the placement of the gages.

350 OHM GAGE →

120 OHM GAGE →
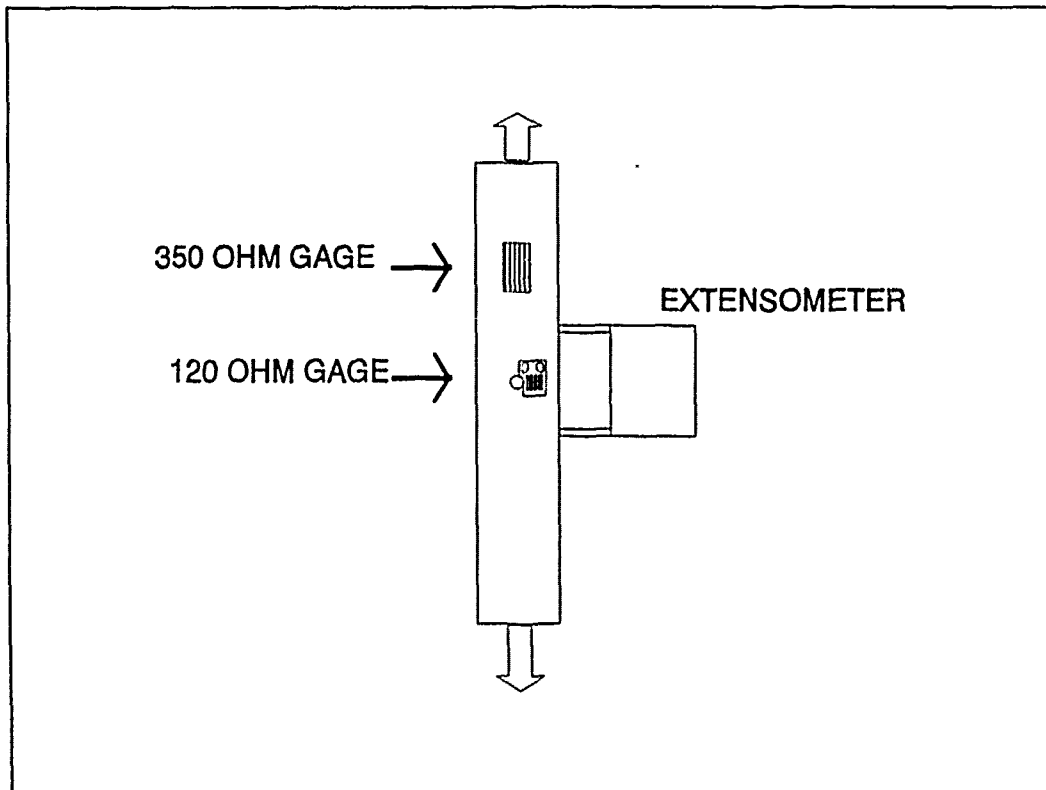
EXTENSOMETER

Figure 3   Strain Gage and Extensometer Location

Specimen Polishing. For some of the room temperature tests the edge of the specimens were polished to enable the formation of acetate replicas showing fiber matrix debonding. The specimens were ground and polished with varying diameters of diamond particles beginning with 45 microns and stepping gradually down to 3 microns. The larger particles flattened the edge and removed most of the scratches and some of the fiber damage caused by the diamond cutting blade. Gradually the size of the grit was reduced to create a very smooth surface. A Metlap® #8 wheel was used on a Buehler Maximet® Specimen Preparation System.

Test Details

The topics of tensile testing technique, data collection, temperature elevation, acoustic emission, and acetate replica technique are addressed below. After the initial discussion of the tensile tester, the room temperature and elevated temperature procedures are addressed independently.

Load Rate Testing. The specimens were tested on a Material Testing System 810 controlled tensile tester under load control. Hydraulic pressure powered both the grips and the loading head. Pre-load of 30 to 60 newtons was used for early tests and then eliminated, since the grips and system were well controlled and stress versus strain data was consistent with or without pre-load. The MTS system

performed well providing very consistent load rates with no problems of slipping or failing at the grips. Line pressure for the grips varied from 4 MPa to 11 MPa. The actual pressure on the specimen was approximately double the line pressure. All tests were run at constant load control of between 15 and 35 newtons per second.

Room Temperature Set-up and Procedures. The data collection for the room temperature tests consisted of strain gages and extensometer with amplifiers, the load cell of the MTS tensile tester, and the acoustic emission equipment. Figure 4 shows a specimen in the grips with the extensometer mounted. The two strain gages were connected through Micromeasurements 2300 Strain Gage Conditioning Amplifiers to a Quatech ADM-12 analog to digital conversion board. The MTS 632-20b clip gage extensometer used the same type of amplifier. A fourth port on the Quatech board received the data from the MTS 810 load cell output and the data was all stored in a single file using a personal computer.

The extensometer used a one inch gage length and was mounted to surround the hole. This provided a total of three strain information sources for the tests. The strain into the extensometer included some strain similar to the 350 ohm remote gage and the strain reflected by the 120 ohm local gage. It then provided a check on strain gage

21
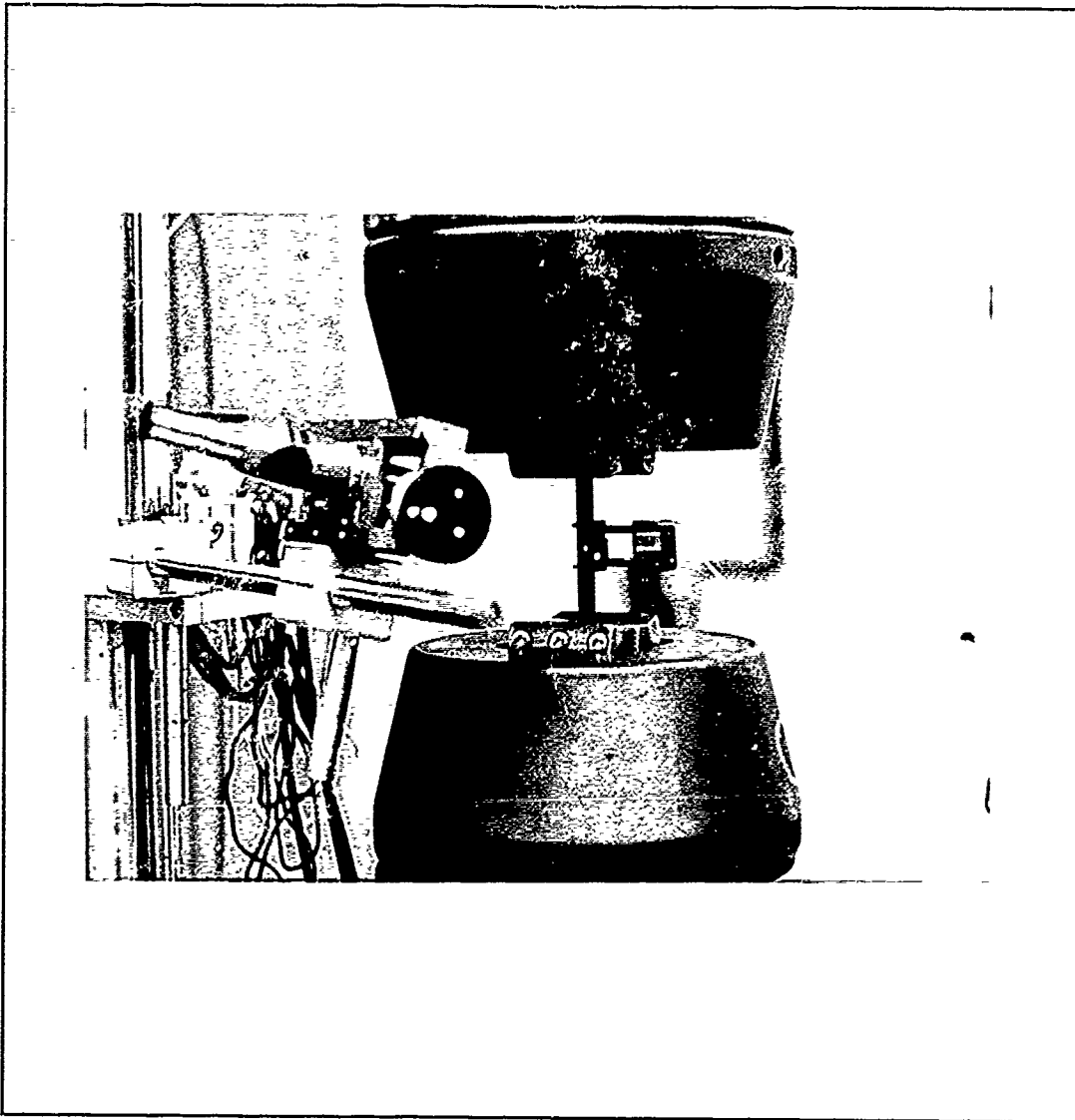
Figure 4   Room Temperature Set-up

installation, since the value of the extensometer strain should be between the values of the two strain gages. The clip gage also served as a comparison to the type of curve expected from the extensometer at elevated temperature where strain gages could not be used.

The MTS 810 equipment included a microprofiler which was used to set the load rate for each test. While the load rate was varied slightly from test to test, for any programmed load rate the MTS equipment maintained that rate until the operator stopped the test or the specimen failed. When desired, the test was held at any load while acetate replicas were taken of the specimen or while dye was applied to the hole area to enhance X-Ray evaluation.

X-ray Procedure. In an attempt to reveal any cracks in the matrix or the debonding of the fibers from the matrix, incrementally loaded specimens were exposed to X-rays. A Phillips 160 kVP unit exposed the type R film from a distance of one meter. Specimens received exposure for four minutes with 75 kV potential and 5mA of current.

Acoustic Emission. A Physical Acoustics Corporation LOCAN AT was used for acoustic emission collection. All tests used the Micro 30 sensor with a model 1220A preamplifier set at 40dB. The frequency band monitored was 100 to 300 KHz. The required data had high amplitudes so a high threshold was set to minimize collection of unwanted data. Size of the data files still exceeded a megabyte in some cases due the tremendous amount of acoustic activity in the off-axis plies. The hydraulic machines used had noise thresholds around 58 and 65 dB. The room temperature tests using the 500 kilonewton machine employed a threshold of 60

dB. The elevated temperature tests used 68 dB as a threshold, since the noise level on the 100 kilonewton tester was higher.

To accurately relate different AE tests some comparison of installation of sensors must be made. Sensors placed directly on the specimens detected the acoustic emission information for room temperature tests. The elevated temperature test data had to be measured with a sensor on the cooled grips, since damage to the sensor would result well below 650°C. A single test at room temperature with the sensor on the cooled grips showed no significant · deviation from the other data collected.

Acetate Replicas. The nonlinearity of the stress vs. strain curve from the first test reflected the debonding of the fiber from the matrix as seen by Johnson. Johnson used acetate replicas to take an imprint of the edge of the specimen, while it was under load (5). Obtaining useful replicas from MMCs is a tedious process requiring good technique. The method described below was not always successful, but it did provide the required evidence.

A flat smooth surface with some contrast between fibers and matrix and a method of minimizing the trapped air bubbles are the critical points to obtain quality replicas. The specimen must have a smooth surface for the replica to show the small changes which occur during loading, but a

very smooth surface will not produce a pre-load replica to compare with later replicas. This difficulty was overcome by lightly etching the matrix with an acidic solution. Dipping the polished specimen for less than five seconds, immediately rinsing with water, and neutralizing with sodium bicarbonate provides the contrast required. The etching solution used for this study contained 33% H_3PO_4, 34% H_2O, 22% HF, and 11% HNO_3 by volume. Etching only a portion of the specimen edge and taking replicas across the boundary of the sections has some advantages. The etched portion provides the easily recognizable no load replica and the non-etched section shows the small initial changes better.

The following steps provided the best results in obtaining high quality replicas. The acetate tape was hinged at one end with transparent tape to hold it in place on the edge of the specimen. The surface of the acetate next to the specimen edge was well moistened with acetone. Doing this step first allows a few seconds for the acetate to absorb the liquid and become soft. A pass of the swab over the specimen wets it immediately before the acetate is applied to the area. The acetate is pressed on beginning at one end and sweeping to the other. This forces the most of the air out and minimizes bubbles. The best results for this study were obtained by rolling a small metal cylinder along the acetate beginning at the end. This pressed the

acetate firmly on the specimen pushing it into any cavities and forced out many remaining bubbles.

Elevated Temperature Set-up. The $650^{\circ}C$ tests required different strain instrumentation and a controllable heating mechanism. Since the coupons were not heat treated, care was taken to conduct tests quickly and record the times for each segment of the test. Radiant energy from quartz lamps heated the specimens to $650^{\circ}C$. Lamps were placed about two cm from each face of the specimen. Two thermocouples welded to the specimen provided feedback to a Microcon 823 system, which controlled the current to the lamps. The Microcon system is built by Research Incorporated. Additional thermocouples utilized in the early tests showed a relatively constant $650^{\circ}C$ over a 4-5 cm length including the hole. A five minute gradual increase programmed into the Microcon raised the specimens to temperature. Eight to ten minutes of stabilization time reduced the fluctuation of the thermocouple temperature below two degrees. Elevated temperature tests were conducted with load rate around 23 Newtons per second, so testing to failure took about five minutes. In all cases the tests were completed within 30 minutes from the time the lamps were activated.

An MTS 632-50b high temperature extensometer using quartz rods provided strain data for the elevated temperature tests. The gage length for this extensometer

was one-half inch. The data from the load cell and extensometer were fed into an analog to digital conversion board, as for the room temperature tests. Since only one strain device was possible for each test, some tests measured the strain with the gage length including the hole and some measured the unnotched strain. This provided some indication of the additional strain near the hole.

Tabs were not applied to the elevated temperature specimens. The failures occurred in the heated section even when no hole was present in the specimen. The stress elevation caused by the grips did not cause any failures outside the gage length.

Post-test Analysis Specimen Preparation

Following the tests, evaluation using SEM and optical magnification required some preparation. Cutting, cleaning, and polishing of the specimens was accomplished.

A few specimens were cut one centimeter from the fracture surface with a low speed diamond saw. The fracture surfaces were rinsed with acetone and cleaned in freon using an ultrasonic bath. This prepared them for carbon coating to enhance SEM work. A few specimens were sectioned longitudinally and transversely for post-test evaluation. These were mounted in Epomet® molding compound and ground in the same manner as described above for the edges. After grinding they received polishing at one micron and 0.5

27

microns for several hours on Buehler circular polishers. Cleaning with acetone and freon prepared these for optical microscopic investigation. A carbon coating was applied later to allow SEM examination.

Like most research, much more time was spent in the processes which prepared for and analyzed the tests than in actual testing. The methods of specimen preparation, test set-up, and post-test analysis described here were essential to the production of quality data.

IV. Properties of SCS-6 Beta 21S in a $[0,\pm45,90]_S$ Lay-up

This section investigates the properties of SCS-6/Beta 21S without holes. The integrity of the material used in this study is examined. The change in laminate stiffness during tensile loading is shown to be related to a debonding of the fibers and matrix in off-axis plies. The chapter concludes with an examination of failure surfaces and acoustic emission data for no hole specimens failed in tension.

Material Integrity

Manufacturing processes for silicon carbide fibers in titanium aluminide matrices and other metal matrix composites are still being refined. To insure the integrity of the material used in this study several steps were taken. The plates were X-rayed and checked with C-scans to check for places where delamination or other defects might have occured. No evidence of delamination was found, but one section of the plate contained a gap between the fibers. This section was not used for tests.

Chemistry Investigation. An investigation of the chemical content of the matrix was conducted using a scanning electron microscope (SEM). Wavelength dispersive spectrometry was used to find the concentrations of elements as compared to a calibrated sample. The reader can find a

29

summary of this technique in Williams (15). Three separate
surveys from different areas of the sample were averaged.
The results showed strong correlation with the component
percentages between the actual and expected values (4).
Table I gives the percentages found in the SEM work and the
goal values of the fabrication process. These results
combined with the high failure stresses of specimens with no
hole show that the material used for these tests is sound,
and of good quality.

Table I Beta 21S Chemistry Comparison

Element	Bania Data in %	SEM Results in %
Titanium	78.95	78.5
Molybdenum	15.0	13.9
Niobium	2.7	3.0
Aluminum	3.0	2.8
Silicon	.2	.2
Oxygen	.15	1.6

Laminate Properties

Since this material is so new and manufacturing
processes are still developing, the properties of moduli and
Poisson's ratio for the lamina were calculated using volume

fractions and the Halpin-Tsai equations. These values were
compared with the limited data available. With these values
for the lamina the properties of the composite were
calculated using classical laminated plate theory.

Halpin-Tsai Calculations. SCS-6 fibers are well
characterized, but the matrix material is not. Young's
modulus was obtained for Beta 21S (4), but no value for
Poisson's ratio was available. Ti-15-3 has a ν of 0.3.
Assuming this same value for Poisson's ratio of Beta 21S
gave enough input data to apply the Halpin-Tsai equations.
Assuming this value for ν is reasonable, since the other
properties of Beta 21S follow Ti-15-3 closely (17). The
material used for these tests contains 35% fibers by volume.
This value was determined through an actual count of several
different samples and computing the area of the fibers based
on an SCS-6 mean diameter of 142 μm. Therefore,
V_f = 0.35 and V_m = 0.65. The E_1 modulus of the lamina is
given by

$$E_1 = V_f E_f + V_m E_m \qquad \textbf{(5)}$$

Since E_f is 414 GPa and E_m is 76 GPa, the upper bound of the
E_1 modulus is 194 GPa. The value of ν is found in the same
manner to be 0.27. The matrix is considered isotropic, so
G_m is calculated as 29.2 GPa using $G = E/(2+2\nu)$. The fiber

shear modulus is known to be 160 GPa. The Halpin-Tsai
equations for G_{12} and E_2 are

$$\frac{M}{M_m} = \frac{1 + \xi \eta \, V_f}{1 - \eta \, V_f} \qquad (6)$$

and

$$\eta = \frac{(M_f / M_m) - 1}{(M_f / M_m) + \xi} \qquad (7)$$

The coefficient ξ determines the fiber reinforcement. Two
was used for ξ in the E_2 calculation and one was used for
the G_{12} calculation. Halpin found these values appropriate
for ξ using a circular fiber in a square matrix cell at
about the same volume fraction used here (14). With the
values above, G_{12} = 48 and E_2 = 136 GPa. These calculated
values compare well with recent results at Wright
Laboratory. They found E_1 of about 190 and E_2 of about 130
(17).

Laminate Calculations. Appendix A shows the
calculations used to find the laminate properties for
$[0, \pm 45, 90]_s$. The E_y or Young's modulus for the laminate in
the load direction was calculated as 150 GPa which is very
close to the experimental values seen. The measured modulus

32

of individual specimens ranged from 133 GPa to 147 GPa. In most cases the experimental values are lower than the Halpin-Tsai value by less than ten percent. Since the volume fraction calculations provide the upper bound for the stiffnesses, the Halpin-Tsai equations and the values selected for ξ work very well for this material.

Stress vs. Strain Nonlinearity Indicates Debonding

At about fifteen percent of failure stress the modulus of the laminate changes. Figure 5 shows a typical stress vs. strain curve to forty percent of ultimate load. The slope before the bend corresponds to a Young's Modulus of 140 GPa and the slope after the bend corresponds to E_y of 86 GPa. These two linear portions preceding and following the knee in the curve are not typical of matrix yielding. Evidence indicates that the fiber-matrix interface fails in the off-axis plies at these low stresses.

Yield Stress Calculation. While the shape of the curve is not typical of matrix yielding, the residual stresses in some metal matrix composites cause yielding at very low mechanical loads. The possibility of matrix yielding must be addressed. Figure 6 shows the remote stress plotted against remote strain for four different room temperature tests. The specimens had different hole sizes so the curves end at different ultimate stresses. Note that in each case the plot is linear to about 60 MPa and then curves until
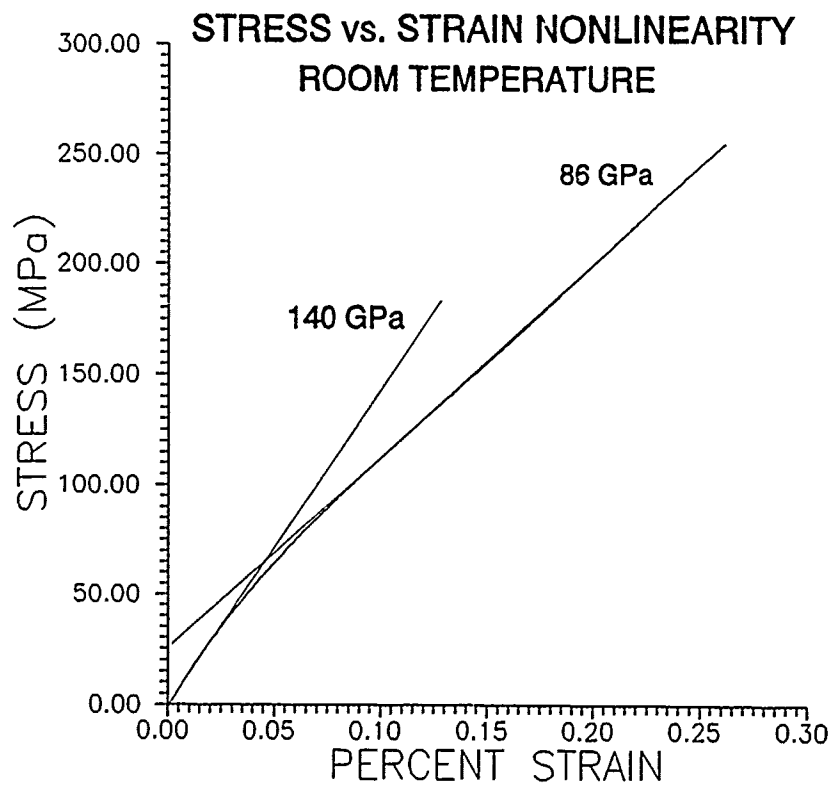
Figure 5 Stress vs. Strain Showing Nonlinearity at Room Temperature

34

REMOTE STRESS VS REMOTE STRAIN
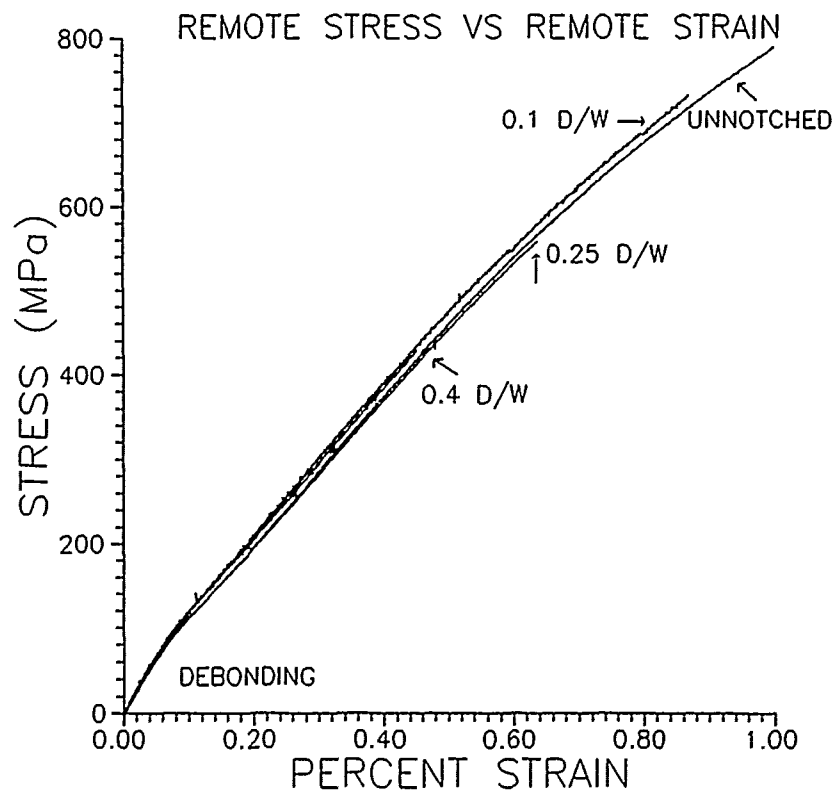
Figure 6 Nonlinearity Consistent for Four Separate Tests

35

about 120 MPa. The plot is linear from this point all the way up to 500 MPa. The largest tensile residual stress for any off-axis laminae in this material and lay-up is 270 MPa. This was calculated using a program called METCAN, which was developed at NASA by Murthy (16). It is a micromechanics analysis which has been developed to calculate the microstresses in metal matrix composites. The first evidence of debonding shown is in the 90° ply so the sum of mechanical and residual stresses is examined there. The mechanical stress in the 90° plies is less than 100 MPa for a 140 MPa stress on the laminate. The value of 140 MPa is used because Figure 5 shows the stress vs. strain linear again by that stress. The sum of the 100 MPa mechanical stress and the 270 MPa residual stress totals less than half of the 840 MPa yield stress of Beta 21S (4). This shows that the nonlinearity is not due to yielding of the matrix.

Acetate Replicas Show Debonding. Using acetate replicas, the stresses associated with this change in slope were correlated with stresses where debonding of the off-axis plies of the laminate occurs. Incremental loading of the specimens showed the gradual change of the material edge, as revealed by the acetate replicas. Figures 7 through 11 show the progression of the debonding and the associated stresses.

Figure 7 shows the fiber before loading and no acetate
has collected at the interface region. Figure 8 shows the
beginning of debonding. This replica was taken on an
unnotched specimen at less than 10% of the room temperature
failure stress. The arrow points to the bright region at
the lower left where the acetate which penetrated between
the fiber and the matrix is shown. Notice that only one
portion of the fiber is debonded allowing the acetate to
penetrate.

As the stress increases, the interface continues to
crack and the matrix pulls away more. The replica shown in
Figure 9 is typical of the type of acetate penetration at
16% of failure stress. The white region showing a
collection of acetate is longer and thicker for most fibers
at this load than at 10 percent of load. Some 90° fibers
are totally surrounded by acetate and very few do not show
some debonding.

The next replica has a significant amount of acetate
near the edge of the fiber. The jagged edge of the fiber
shows clearly against the bright acetate. Figure 10 is a
typical example for 20% of failure stress, but some
variation existed. There were no 90° fibers which did not
show at least partial debonding at 20% of failure stress.

The final replica shows the clumps of acetate which
surround the 90° fibers at 90% of failure stress. The high
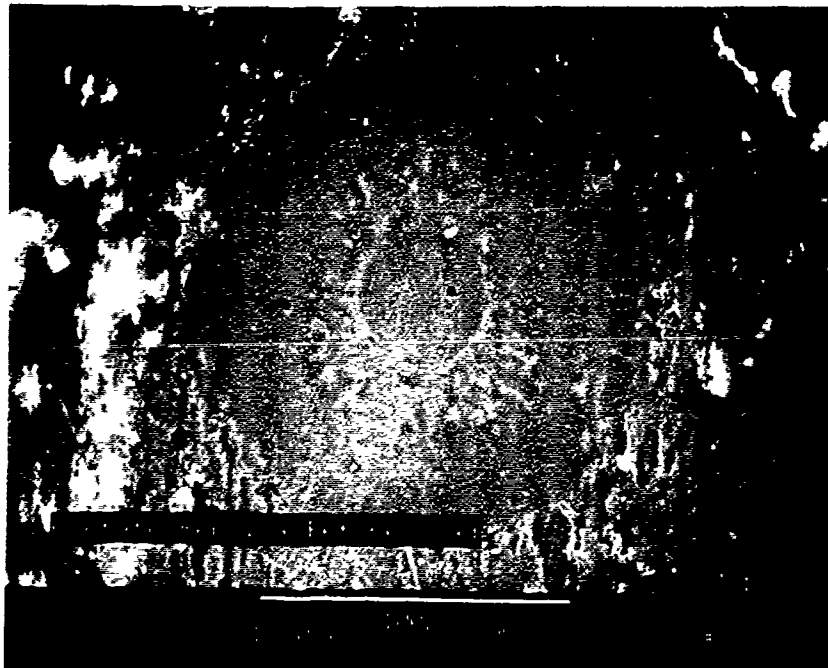
Figure 7   Acetate Replica of Fiber Before Load
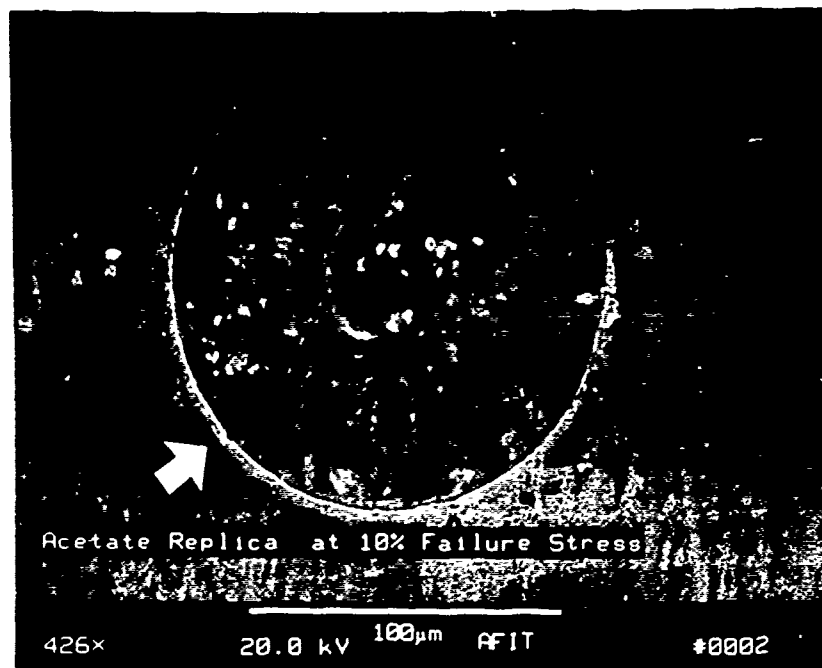
Figure 8 Acetate Replica for 10% of Failure Stress
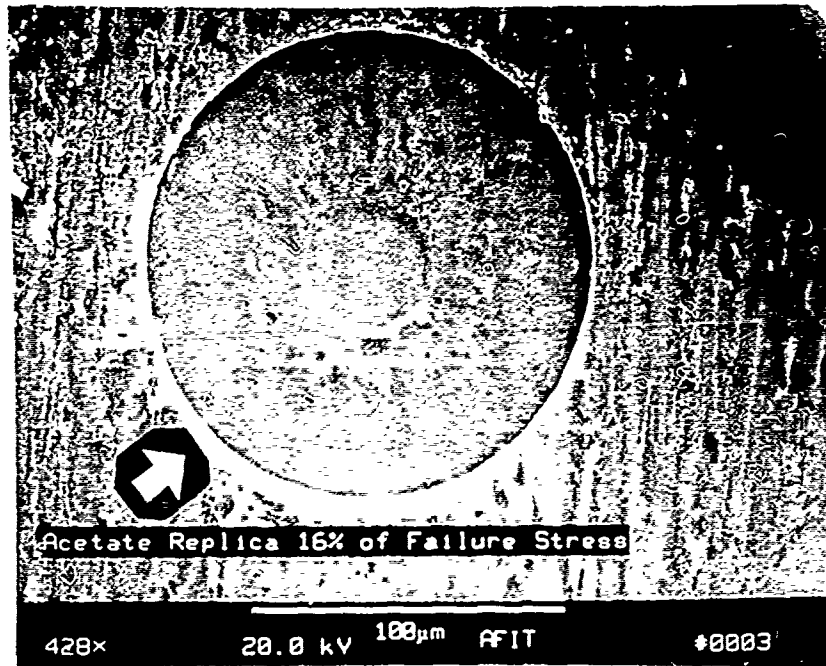
Figure 9   Acetate Replica at 16% of Failure Stress

40
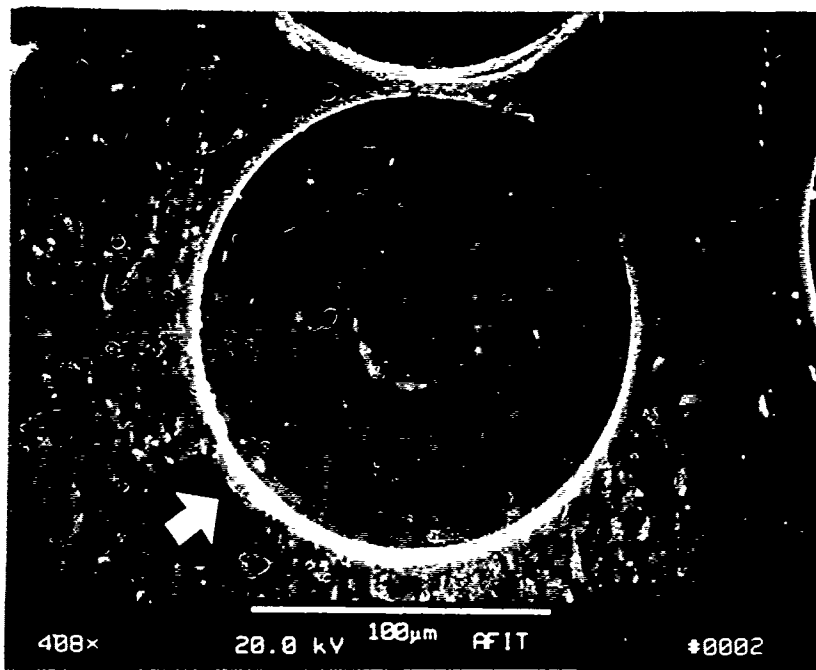
Figure 10 Acetate Replica at 20% of Failure Stress

41

modulus debonded fibers extend beyond the matrix during loading, since the Poisson effect pulls the matrix in. The effect is most prominent in the 90° fibers, since transverse stresses easily pull the matrix directly along the fibers. At higher stresses the transverse strain of the matrix is greater and near failure stress the fibers protrude significantly. The acetate gathers around the rim on the surface of the matrix, as seen in Figure 11. Very little acetate is seen surrounding the 45° fibers, but further evidence and analytical work show that they are debonded as well.

Failed Specimens Show Debonding. Figure 12 shows protruding fibers on the edge of a failed specimen. This SEM photograph is of an area 0.5 cm from the fracture surface. When the matrix yielded and the specimen failed the protruding fibers were left exposed. As discussed above, the replicas showed that this effect began at very low loads and this example shows the amount of fiber protrusion. The lack of acetate surrounding the 45° fibers is explained in part by this photograph. The 90° fibers stick out so far that the acetate never gets pressed around the 45° fibers.

Acoustic Emission. Acoustic emission data for all specimens tested showed tremendous activity at the same stress levels where the replicas show debonding. Figure 13
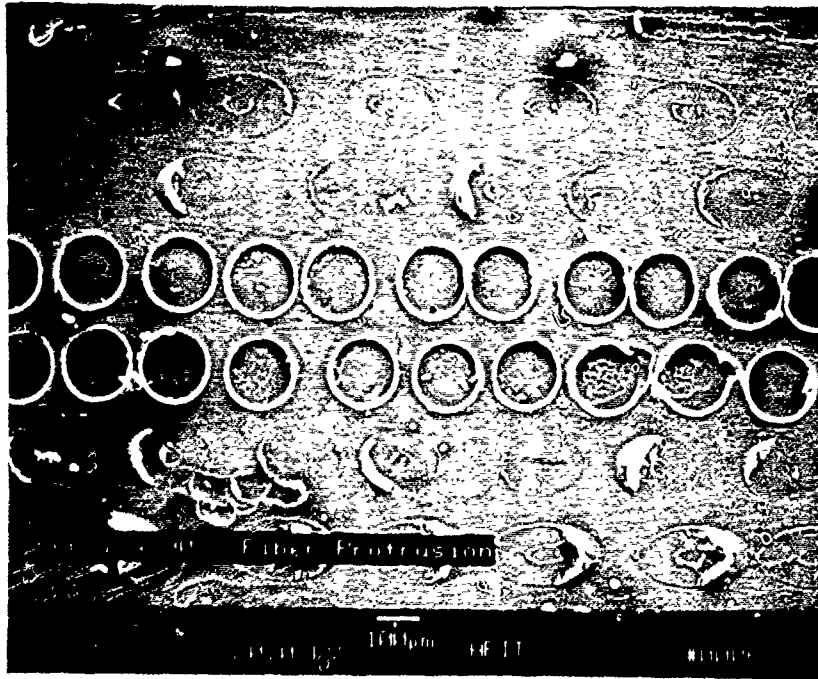
Figure 11 Acetate Replica at 90% of Failure Stress

43
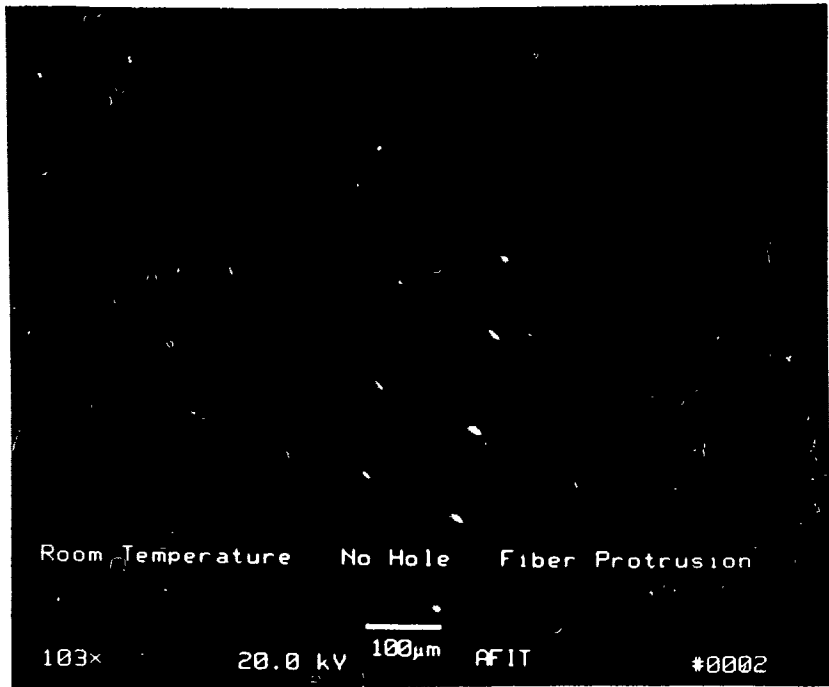
Figure 12 Off-axis Fibers Protruding From a Failed Specimen

44

is a histogram of hits vs. load. Surprisingly, the peak
activity zone is not near the failure load. The large
number of hits between 10% and 20% of failure stress
corresponds to the nonlinearity of the stress vs. strain
curve and the evidence shown by the replicas. This acoustic
activity is the result of the matrix pulling away from the
fibers and cracking the interface zone.

Laminate Modeling

The replicas and photographs clearly show extensive
debonding occurs in the 90° plies, but it is not as obvious
that the 45° fibers debond. To evaluate the extent of
debonding in the 45° fibers the Halpin-Tsai equations and
total discount method were used to model the laminate and
calculate the Young's modulus.

One method for modeling a laminate where significant
loss in modulus or strength has occured is the total
discount method. As the name implies, all of the strength
and stiffness due to the discounted plies are removed. When
only the 90° plies were discounted, the modulus became 115
GPa. If all the 90° and 45° plies are discounted, the
modulus falls to 48 GPa. This brackets the typical
experimental value of 86 GPa, but neither one is very close.
The total discount model assumes zero stiffness contribution
for the discounted plies, but in this case the matrix
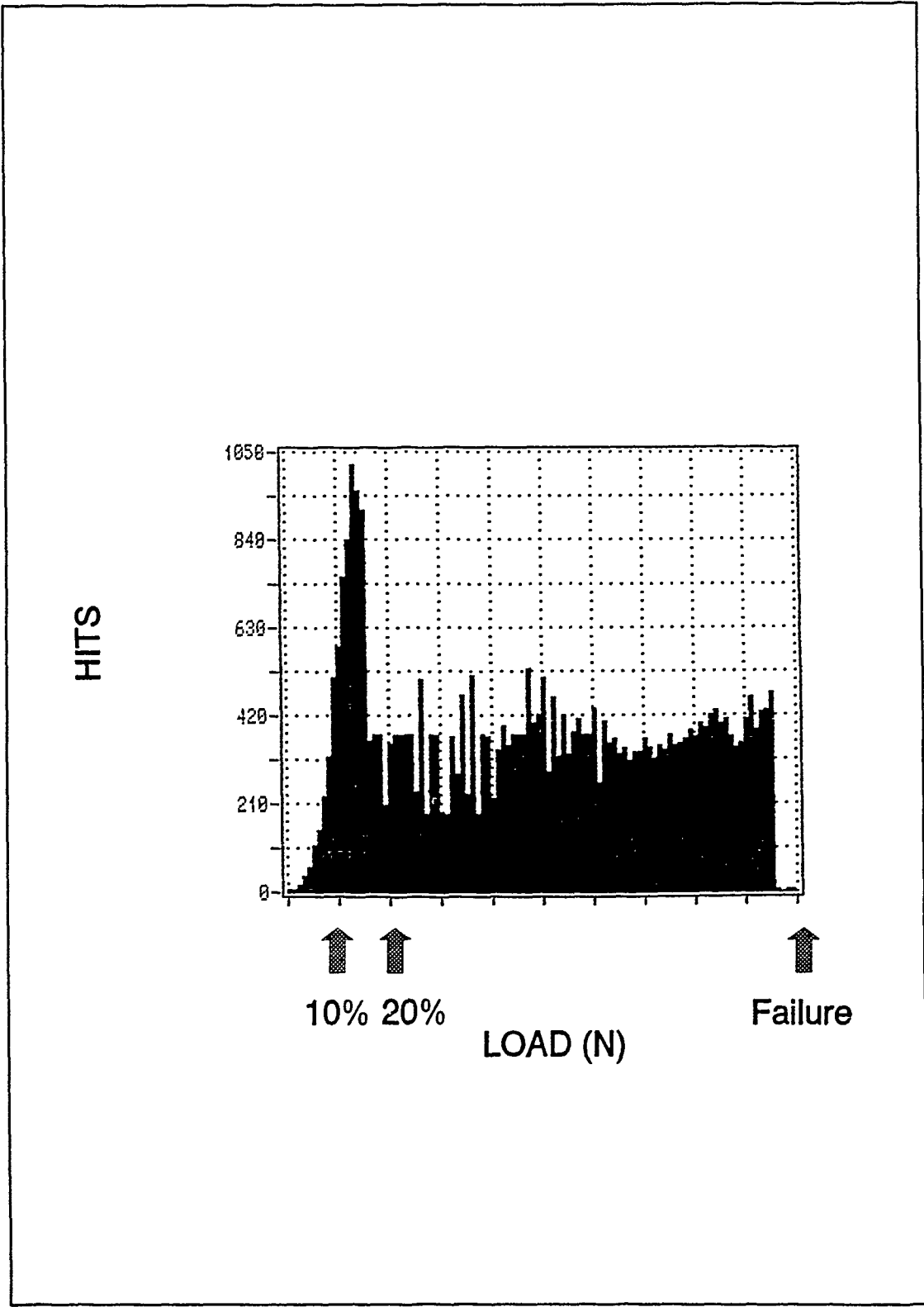
Figure 13 Acoustic Emission Plot of Hits vs. Load Showing Debonding

46

stiffness remains. Halpin and Tsai have provided a means to model the off-axis plies with only the matrix stiffness.

Jones addresses the use of Halpin-Tsai for discounting the fiber contribution. The moduli of the fibers in the off-axis plies are set equal to zero, since they no longer act to strengthen or stiffen the laminate (13). E_1 and G_{12} are calculated by letting V_f equal zero. Letting $E_f = 0$ in Equation 3 results in a value of $-\frac{1}{2}$ for η, since $\xi = 2$. Then $E_2 = E_m(1 - V_f)/(1 + \frac{1}{2} V_f) = 60$ GPa. The same type of calculation shows the shear modulus $G_{12} = 14$ GPa, when $\xi = 1$. Table II gives all values for the bonded and debonded lamina.

Table II   Lamina Properties From Halpin-Tsai

	LAMINA BEFORE DEBONDING	LAMINA AFTER DEBONDING
E IN LOAD DIR	194 MPA	46 GPA
E TRANSVERSE	136 MPA	40 MPA
POISSON'S RATIO	0.27	0.16
SHEAR MODULUS	48 MPA	14 MPA

Calculating laminate stiffnesses using these values for the off-axis plies gave a value of 80 GPa for the loading direction. This calculation is presented in Appendix A. The

47

experimental data for the second linear slope in Figure 5 is
86 GPa. Combining this close agreement with the other
information shows that all of the off-axis plies debond at
around 15% of the failure stress. The great majority of the
load in the laminate must be absorbed by the fibers in the
loading direction. The other plies in the laminate only
provide the strength and stiffness of the matrix. Table III
contains the stiffnesses for the bonded and unbonded
laminate. The laminate modulus in the loading direction
decreased from 150 GPa to 80 GPa. The debonding of the off-
axis plies will impact the maximum stress concentration
around the hole and the failure pattern.

Table III Quasi-isotropic SCS-6/Beta 21S Laminate
Properties

	$[0,\pm45,90]_S$ LAMINATE	DEBONDED LAMINATE
E IN 0° FIBER DIR (GPA)	140	80
E TRANSVERSE (GPa)	140	45

Elevated Temperature Stress-Strain Curves

When same type of non-linearity of the stress vs.
strain curves showed at elevated temperature, the same type

of laminate model was used to calculate the stiffness. The highest initial experimental modulus seen during loading was only about 80 GPa. Appendix B shows the laminated plate calculation of the as delivered composite stiffness as 130 GPa. This shows a major discrepancy. When the modulus for the debonded material was calculated for only the 90° fibers debonded, the resulting value was about 105 GPa. If all off-axis fibers are debonded, Halpin-Tsai predicts a modulus of 68 GPa.

The matrix modulus was iterated to determine what matrix modulus would create the laminate modulus corresponding to 80 GPa. The fiber modulus remained at 414 GPa for this calculation, since the SCS-6 fiber modulus varies very little with temperature (2). The value of matrix modulus which gives 80 GPa for a laminate modulus was only 7 GPa and the calculation is shown in Appendix C. This modulus is far below any experimental modulus seen by Khobaib in his research with fiberless Beta 21S (18). It is possible that the material partially debonds as the temperature is raised to 650^OC. Since the material further debonds under mechanical load anyway, this does not invalidate the failure stresses recorded in this study.

Unnotched Tensile Tests

To verify material integrity and gather baseline data for the varying size hole tests, several specimens were

failed with no hole. Table IV gives the results of these tests.

Table IV. Results of Tensile Tests With No Hole

Room Temperature

Specimen #	Width (cm)	Thickness (cm)	Strength (MPa)	Modulus (GPa)
3	1.31	0.184	846	143
17	1.28	0.183	837	147

Elevated Temperature

| 2 | 1.29 | 0.183 | 409 | 80 |
| 20 | 1.27 | 0.184 | 385 | 70 |

Unnotched Fracture Surfaces and Acoustic Emission. The fracture surface appearance and acoustic emission output differ for the room temperature and 650°C tests. While these differences are present many similiarities exist as well. The high modulus fibers bear most of the load and their lower failure strain causes them to fail before the matrix at both temperatures.

Acoustic Emission. Failure of the SCS-6 fiber creates an acoustic event with long duration and high amplitude. Many events of greater than 90 dB amplitude and with duration exceeding 1 millisecond were observed.

Roman's recent work at Wright Laboratories with single SCS-6 fibers failed in tension indicates that events of this amplitude and duration are indicative of fiber failure (19). The fibers were imbedded in a metal matrix for the test so the same values should apply for this study.

The acoustic emission data showed activity typical of fiber fracture at very different percentages of specimen failure for the two temperatures. For the room temperature tests, many hits with amplitude greater than 90 dB and longer than 1 ms occured at less than fifty percent of failure stress. For the $650^{\circ}C$ tests very few of these significant events took place until 90% of failure load. The acoustic data were filtered to include only the activity exceeding 90 dB and 1 ms. These data are presented as histograms in Figure 14. The top figure is the room temperature test and shows less than ten percent of these hits in the last 5% of the load. The bottom figure shows that about 90% of the fiber breaks happened in the last 5% of load for the elevated temperature test.

Fracture Surfaces. Three major differences exist between the two surfaces. The high temperature specimens show necking near the fracture, less large dimpling in the matrix fracture surface, and much more extensive fiber pullout.
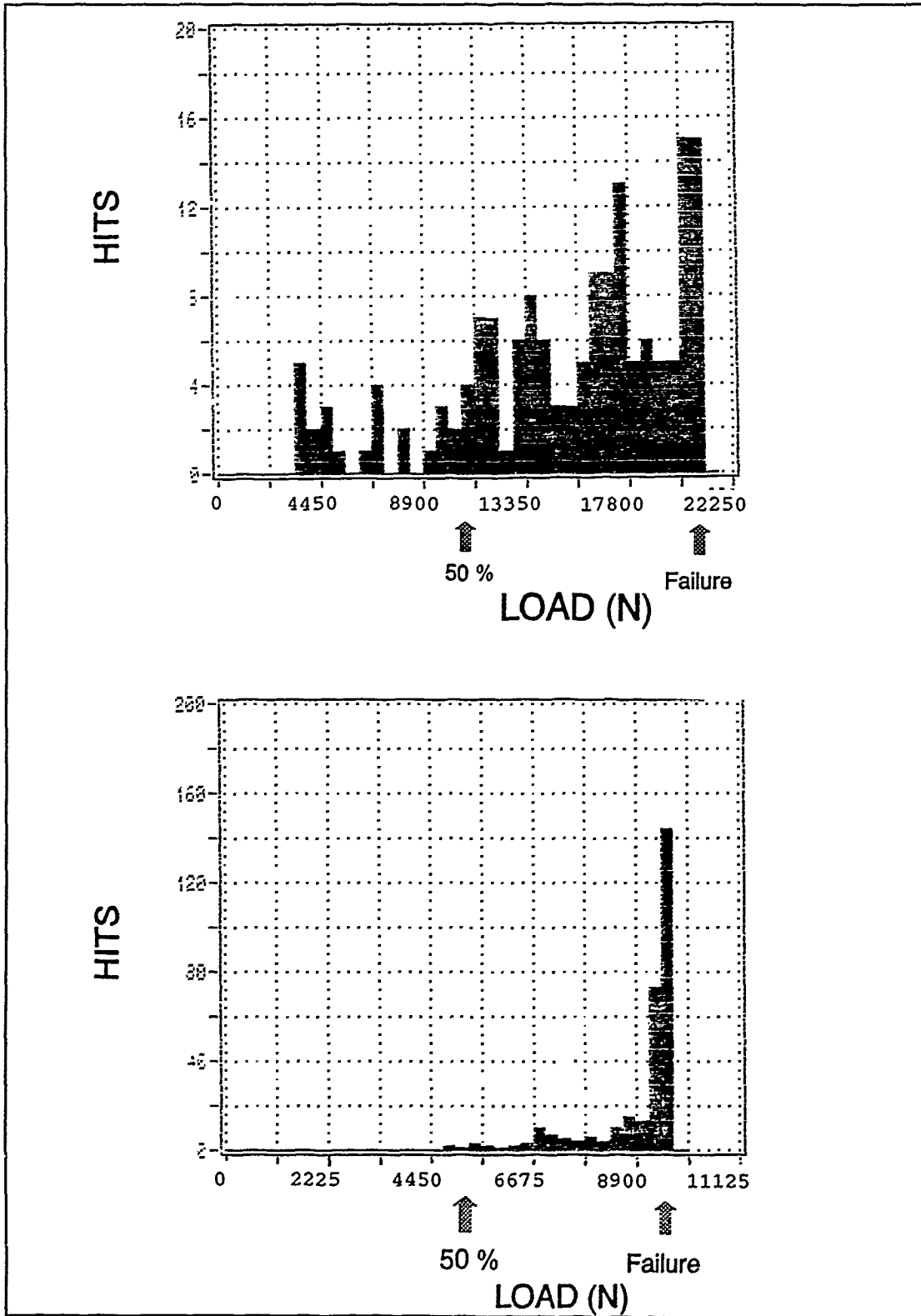
Figure 14 Acoustic Emission Data For Unnotched Tests at Room
Temperature
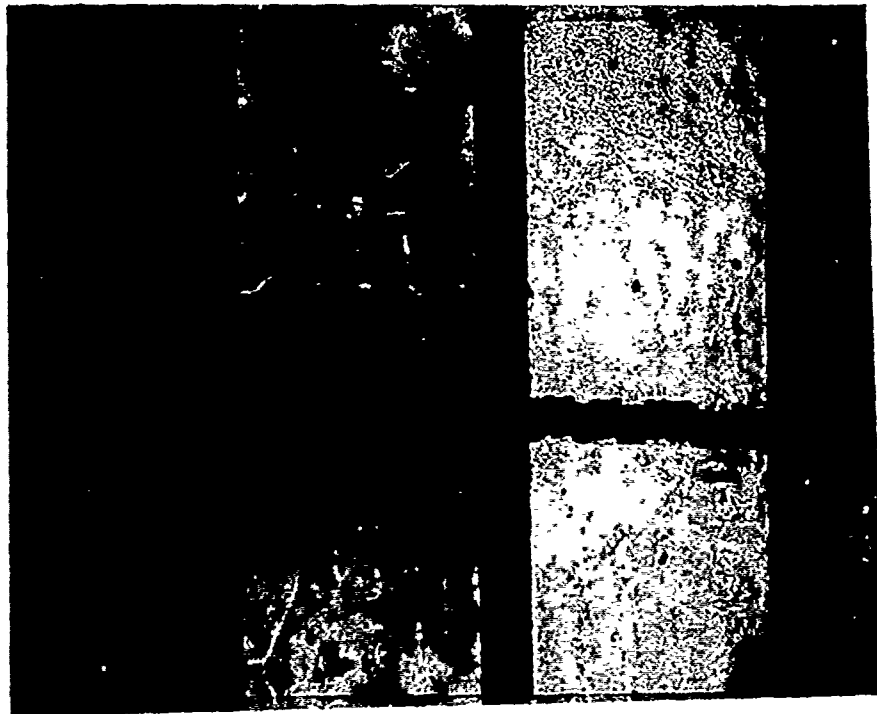
Figure 15   Unnotched Specimens For Room Temperature and 650°C

53

Figure 15 displays a room temperature and an elevated temperature specimen in a top view. The high temperature coupon is next to the ruler. The room temperature specimen failed perpendicular to the load with almost no fiber pullout. By looking at the $650^{\circ}C$ specimen and the dark lines, the reader can see some necking in the matrix of the elevated temperature specimen. The off-axis fibers protrude from the matrix as seen in Figure 12 making the reduction in matrix width a little difficult to see.

The SEM photographs in Figure 16 shows the type of fracture surfaces seen in the matrix of the $650^{\circ}C$ specimen. The top photograph was taken near the 0° fibers. This type of ductile fracture was seen over most of the surface, especially near the fibers. In a few cases the cleavage fracture shown in the bottom picture was seen. Even for this picture higher magnification shows that it is primarily a ductile fracture. Photographs of room temperature specimens with holes shown below have obvious dimpling in the fracture surfaces. Higher magnification of the apparently flat surfaces in the bottom photograph of Figure 16 revealed dimples here as well. The weaker matrix at elevated temperature allows initiation of dimpled fracture at small particles as well as large ones. This results in a flatter surface, but the fracture is still primarily

Ductile Fracture of Unnotched Specimen
High Temperature
496× 20.0 kV 10µm AMRAY #0003

520 Fracture Surface Between 90 Degree Fibers
600 20.0 kV 10µm AFIT #0004
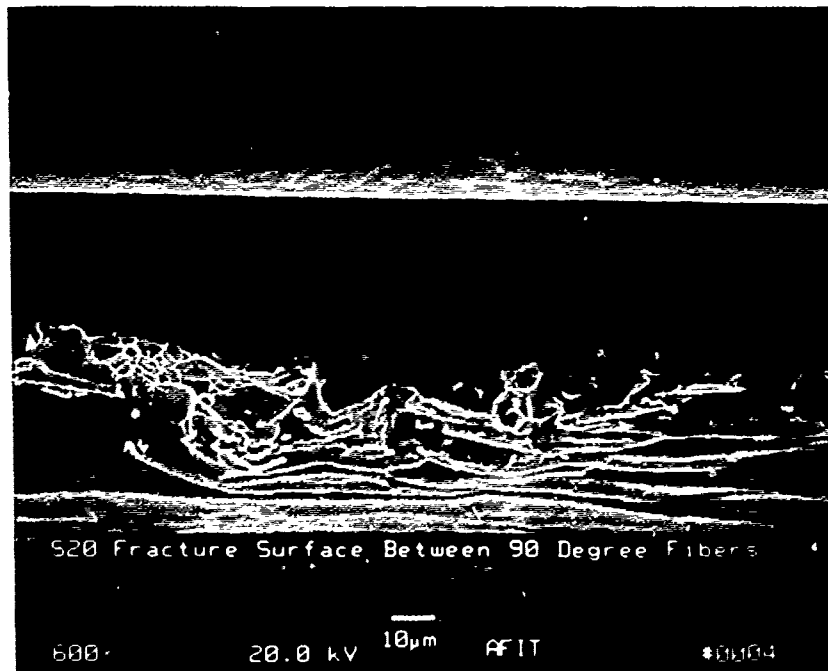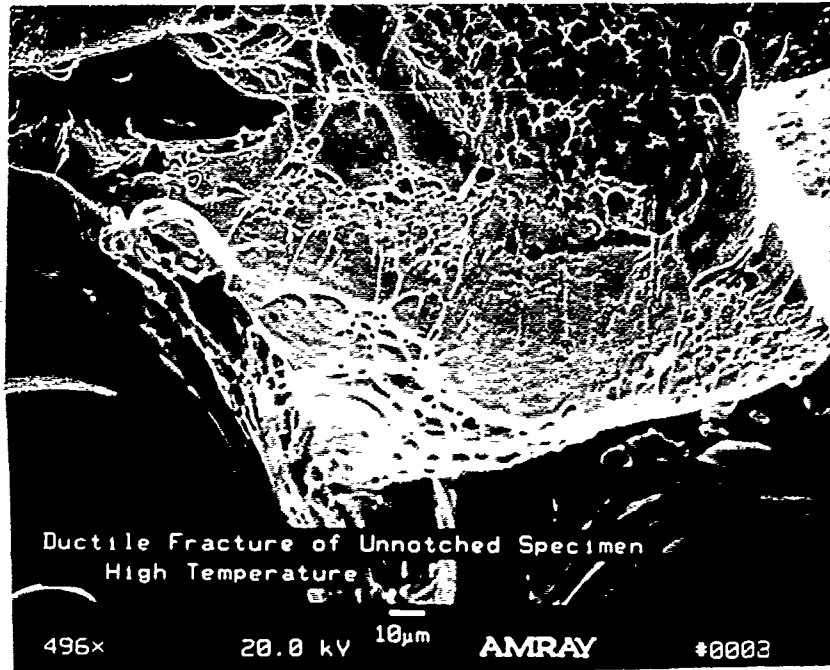
Figure 16   Fracture Surface of Unnotched Specimen at 650°C

55

ductile. A far more in depth discussion of the fracture mechanism is given below for the specimens with holes.

Summary

This part of the study revealed several properties of SCS-6/Beta 21S which will impact the characterization of failure stresses with holes. First, the moduli of the composite were calculated using Halpin-Tsai. A review of stress vs. strain data showed a nonlinearity caused by debonding of the fibers from the matrix. Modeling this behavior with the Halpin-Tsai equations showed that all the off-axis plies were debonded, leaving the composite as two 0° lamina surrounding six layers of Beta 21S. Examination of acoustic emission data showed many large events at loads below 90% of failure stress for room temperature tests, but almost all the large events for elevated temperature occured in the final 10% of load. Finally, the fracture surfaces differ for the two temperatures with a lot of fiber pullout at 650^OC. With this information the study of holes, was undertaken as discussed in the next chapter.

V. Results and Discussion of Tensile Tests With Holes

This section addresses the effect holes have on failure stress at both temperatures and the impact holes have on failure modes. The objective is to establish whether or not SCS-6/Beta 21S is a notch sensitive material. The term notch sensitivity as used here implies a reduction in strength above the reduction expected simply due to the reduced area bearing the load. All materials have a stress concentration at a notch, but extensive yielding or longitudinal cracks can negate the effect of the stress concentration and make the material notch insensitive. The area near the hole where fiber damage occurs is called the damage zone in this study, even when damage to the matrix is not observed. The chapter concludes with a comparison to an existing failure prediction method to see if it can predict the behavior of tested specimens with different D/W ratios.

The discussions which follow are based on a stress concentration existing at the hole, so the stress concentration factors were calculated for the bonded (undamaged) and unbonded (damaged) material. The stress concentration factor is the ratio of the highest stress at the notch to the far field stress. Greszczuk showed that once laminated plate theory produces the laminate properties, a theoretical stress concentration factor for an

infinite plate can be calculated (8). In terms of the stiffness matrix developed in Appendix A the stress concentration factor is

$$K_t = 1 + \left\{ \frac{2}{A_{22}} + \left[\sqrt{A_{11}A_{22}} - A_{12} + \left(\frac{A_{11}A_{22} - A_{12}}{2A_{66}} \right) \right] \right\}^{\frac{1}{2}} \qquad (8)$$

The A_{ij} represent elements of the A matrix given in Appendix A. The reader is reminded that the composite notation used to write eq (8) denotes the (3,3) element of the A matrix as A_{66}. Before debonding the lay-up is quasi-isotropic and the infinite plate stress concentration factor is 3. After the debonding, new material properties develop, a new matrix is formed, and the stress concentration factor becomes 3.18 according to this equation. Because of the finite width of the specimen, the reduction in area by the removal of the material for the hole elevates the stress as well. The larger the hole the larger this factor becomes. Tan developed a finite width correction factor (FWC) for orthotropic plates, which converts the stress concentration values for infinite width to finite width. Tan's FWC is applied to the failure prediction so that specimens of different hole sizes and widths can be compared (20).

Metal matrix composites rarely display delamination and no evidence of delamination was seen during this study.

58

When there is no delamination, all the plies in the laminate see the same strain. The stiffest laminae by far are those with 0° fibers, since the other six plies provide only the stiffness of the matrix. The matrix has twenty times more elongation to failure than the fibers, so the fibers should fail before the matrix. Due to the stress concentration at the hole the fibers in the 0° laminae near the hole will realize more strain and will fail first.

Room Temperature Results and Discussion

This section addresses stress vs. strain for the different strain locations and the failure data for the room temperature tests. The discussion includes evidence of stress concentration and general descriptions of the failure.

Stress vs. Strain Data for a Single Specimen. The three sources of tensile strain data from specimens should give an indication of the stress concentration at the hole. For a given load the remote gage will indicate the lowest strain, since the area is greater there and the same load will produce less deformation. The gage near the hole will indicate the highest strain and the extensometer should fall somewhere in between the two strain gages, since the gage length includes the hole. Figure 17 displays the strain data for a test using a D/W ratio of 0.4. In all three

cases the stress is calculated using the unnotched area.
The plot supports the preceding observations.

Some of the increase in strain near the hole is simply
a result of the reduced area of the section including the
hole, since the same load on the specimen creates a larger
strain for the smaller area. To show the existence of a
stress concentration due to the hole, we plot the local
stress against local strain and remote stress against remote
strain. As a worst case scenario, assume the cross-
sectional area seen by the entire local gage is the minimum
area of the specimen. The minimum area is calculated by
subtracting the diameter of the hole from the width and then
multiplying by the thickness. The local stress is then
calculated by dividing this reduced area into the load.
This stress is plotted in Figure 18 against the strain of
the local gage. The upper curve on the plot shows remote
stress against remote strain. Since the local strain plot
still shows more strain for a given stress, the local gage
is certainly experiencing an increase in strain and stress
due to the hole and not just from the reduction in area. It
is significant to note that the curves diverge as the load
increases. This indicates the difference in strain
increases with the load and this increase is probably due to
the fiber damage near the hole which is discussed later.
This again implies that the failure would begin at the edge

THREE STRAINS FOR 0.4 D/W
ROOM TEMPERATURE

LOCAL GAGE

EXTENSOMETER

REMOTE GAGE
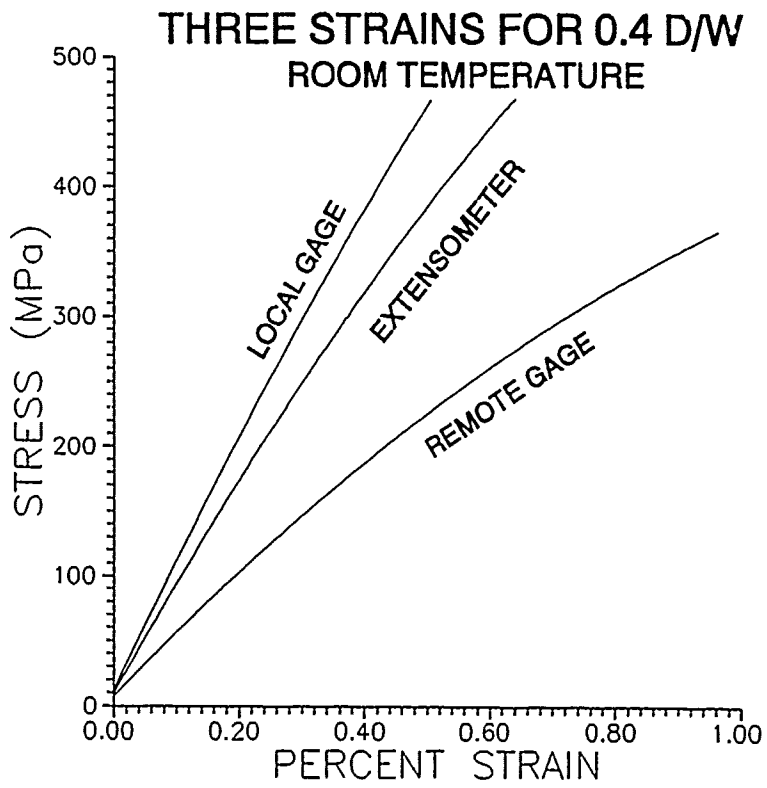
Figure 17   Three Strains for a Single Room Temperature Test

61
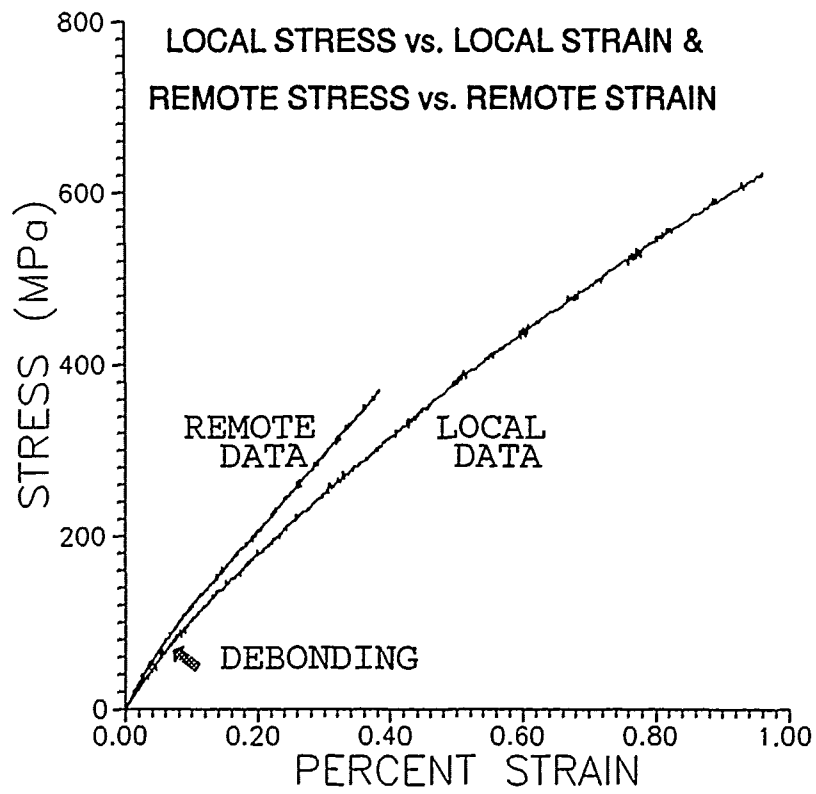
Figure 18 Local σ vs Local ϵ & Remote σ vs Remote ϵ

of the hole and the specimen should fracture at the maximum tensile stress point of $\theta = \pi/2$.

Stress vs. Strain for Different Hole Sizes. The remote stress is plotted against local strain for three hole sizes and an unnotched specimen in Figure 19. The four tests show different amounts of local strain due to the difference in size of the net section area and the stress distribution in front of the hole. Whitney and Nuismer developed a failure criterion based on the idea that the hole size impacts the stress distribution in front of the hole (21). For an infinite plate the stress at the 90° point of the hole is the same for all hole sizes. For larger holes though, the maximum stress directly at the hole falls off more slowly than for small holes. Their point stress criterion uses the concept that for any size hole there is a critical distance in front of the hole where the stress reaches the strength of the unnotched material. When the stress at this point reaches the unnotched strength value, failure occurs. This method will be applied for this study (21).

General Fracture Properties. In every test the failure occurred at the 90° point, but the fracture was so rapid that no small crack at the hole could be seen. If tests were stopped to examine the specimen, the ductile matrix exhibited no cracks before failure. Even with a microscope
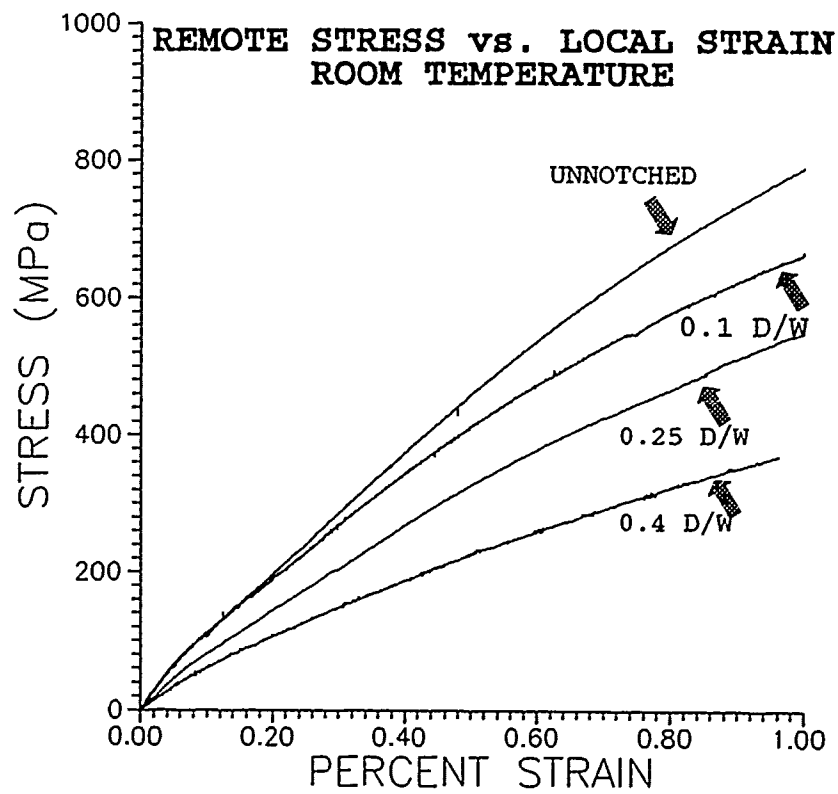
Figure 19 Remote Stress vs Local Strain at Room Temperature

64

mounted on the test machine to examine the hole all the way to failure, no cracks were seen.

X-rays taken to look for debonding provided an excellent opportunity to look for cracks as well. The X-rays did not show the debonding even using dye penetrant and they did not show cracks in the matrix either. Figure 20 shows an X-ray taken after the specimen was loaded to 93% of failure stress. No cracks are visible.

Failure Data For Room Temperature. Figure 21 shows the failure stresses plotted as a function of diameter-to-width ratio. All the points fall below the diagonal line representing the net section strength. This indicates the effect of the stress concentration caused by the hole. The failure strength of the 0.4 D/W samples is less than half the strength of the samples without a hole. Table V summarizes the strength data for the room temperature tests.

To accentuate the effect of the stress concentration at the hole, Figure 22 plots the same data as before, but with the section area stress at failure. The stresses are normalized by the average strength of the unnotched specimen tests. If there was no effect from the hole, the points would cluster around the normalized value of one. Since all points are below that value and the strength continues to decrease as the D/W increases, the room temperature tests show notch sensitivity.
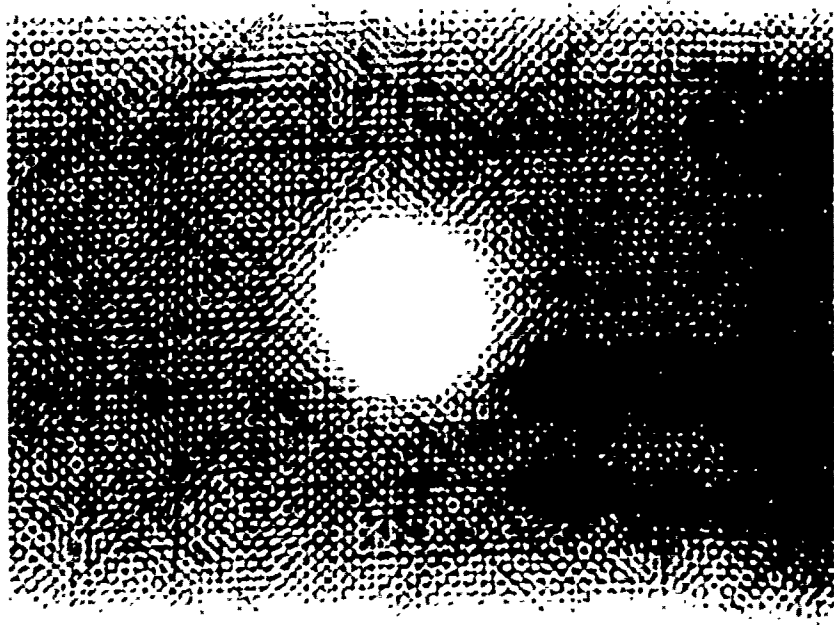
Figure 20   X-ray of Partially Loaded Specimen

STRENGTHS BASED ON
REMOTE AREA
ROOM TEMPERATURE

NET STRENGTH LINE

STRESS (MPa)

DIAMETER / WIDTH
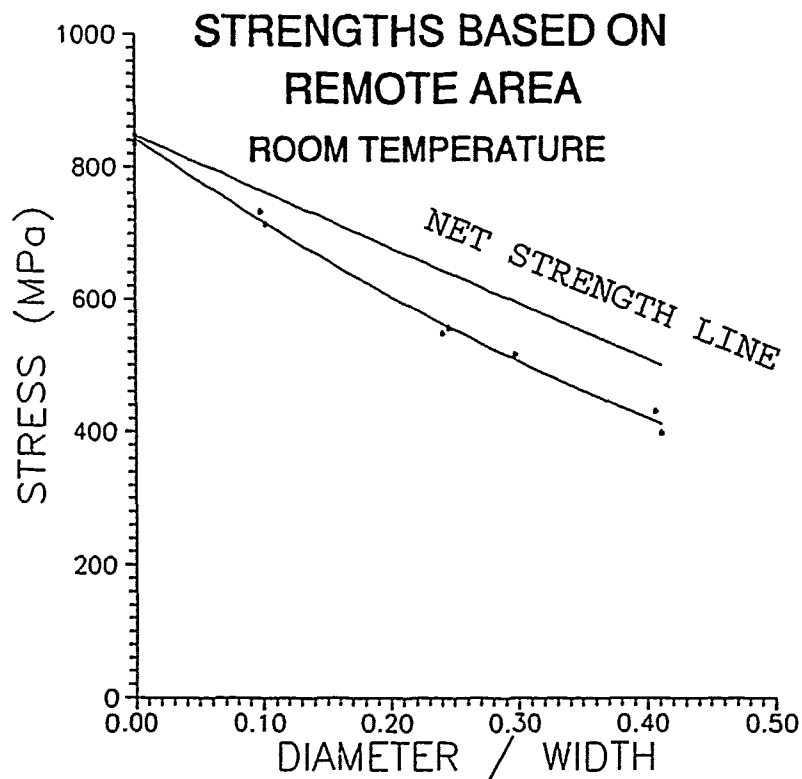
Figure 21   Failure Stresses as a Function of D/W

Table V Room Temperature Tensile Test Data

NUMBER	LOAD (N)	DIAM (CM)	WIDTH (CM)	D/W	DEPTH (CM)	REMOTE STRESS (MPa)
3	20370	0.0000	1.3056	0.0000	0.1842	847.3
17	19510	0.0000	1.2751	0.0000	0.1834	834.4
9	17210	0.1253	1.2852	0.0975	0.1829	732.2
8	16500	0.1295	1.2690	0.1021	0.1824	713.0
5	12990	0.3099	1.2878	0.2406	0.1838	548.5
4	13310	0.3200	1.3051	0.2452	0.1834	556.1
18	11980	0.3787	1.2751	0.2970	0.1824	515.2
12	9964	0.5156	1.2700	0.4060	0.1824	430.2
10	9207	0.5207	1.2675	0.4108	0.1829	397.2

Elevated Temperature Results and Discussion

The matrix strength at $650^O C$ drops to about one-fourth
of the strength at room temperature (18), but the fibers
lose only about five percent of their corresponding strength
(2). The 0° fibers bear almost the entire load after
debonding occurs. Using the data from Appendix B and Eq (8)
the stress concentrations are 3 and 3.28 for the bonded and
debonded models. Therefore, a higher stress concentration
exists near the hole at failure and notch sensitivity should
be seen in this case also.

Stress vs. Strain Data for $650^O C$. For the elevated
temperature tests only one strain measuring device was

Normalized Failure Stress

Room Temperature
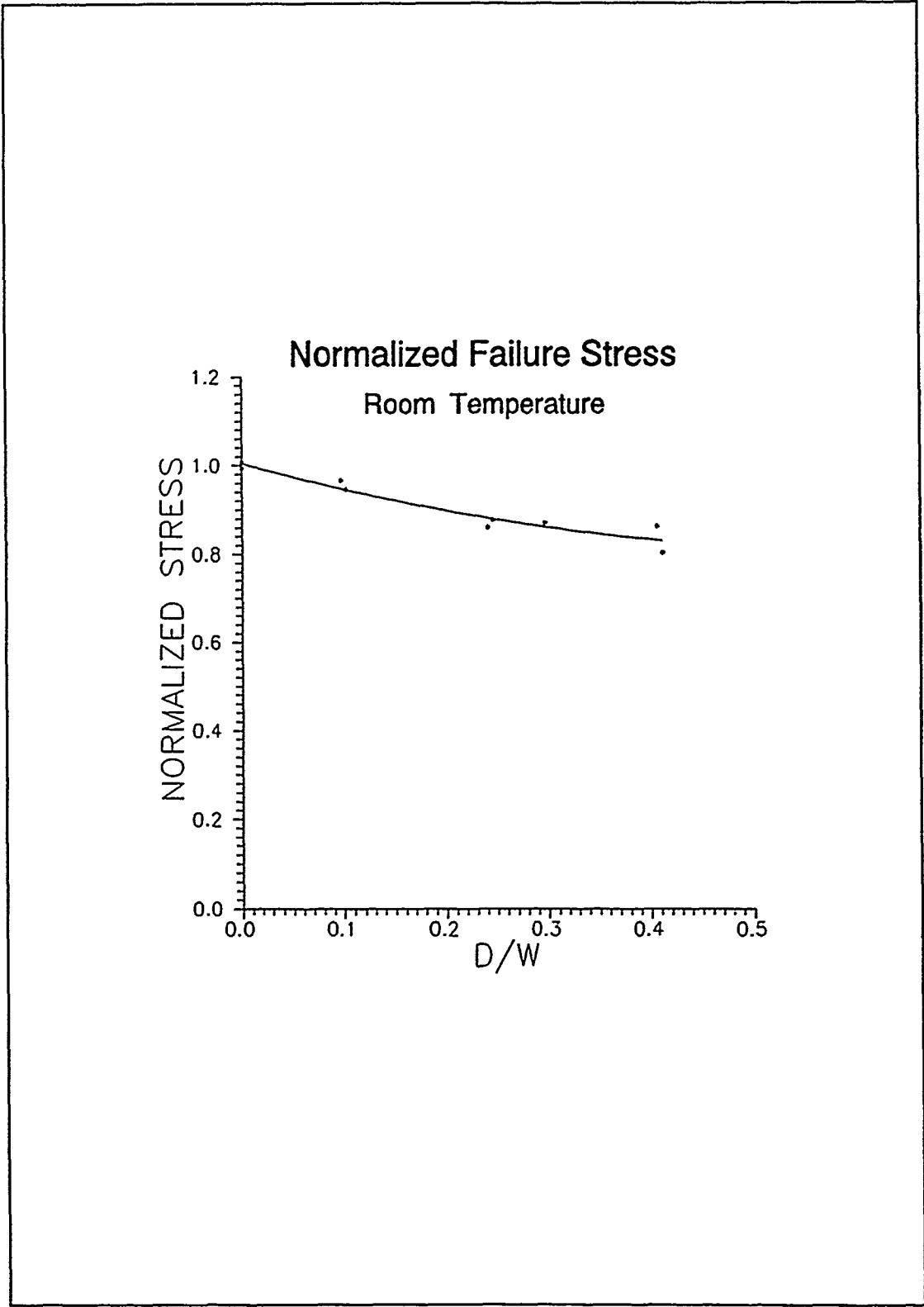
Figure 22   Normalized Section Area Stress at Failure

available. The extensometer was mounted away from the hole
in some tests and in others it was mounted such that the
gage length included the hole. The results for remote
strain and local strain are presented in Figures 23 and 24
respectively. Figure 23 shows very little yielding prior to
failure. The yielding is taking place at the hole and is
outside the gage length of the extensometer when the
extensometer is located to measure far field strain. Figure

650C REMOTE STRESS VS REMOTE STRAIN

UNNOTCHED

0.1 D/W

0.25 D/W

0.4 D/W

STRESS (MPa)

PERCENT STRAIN
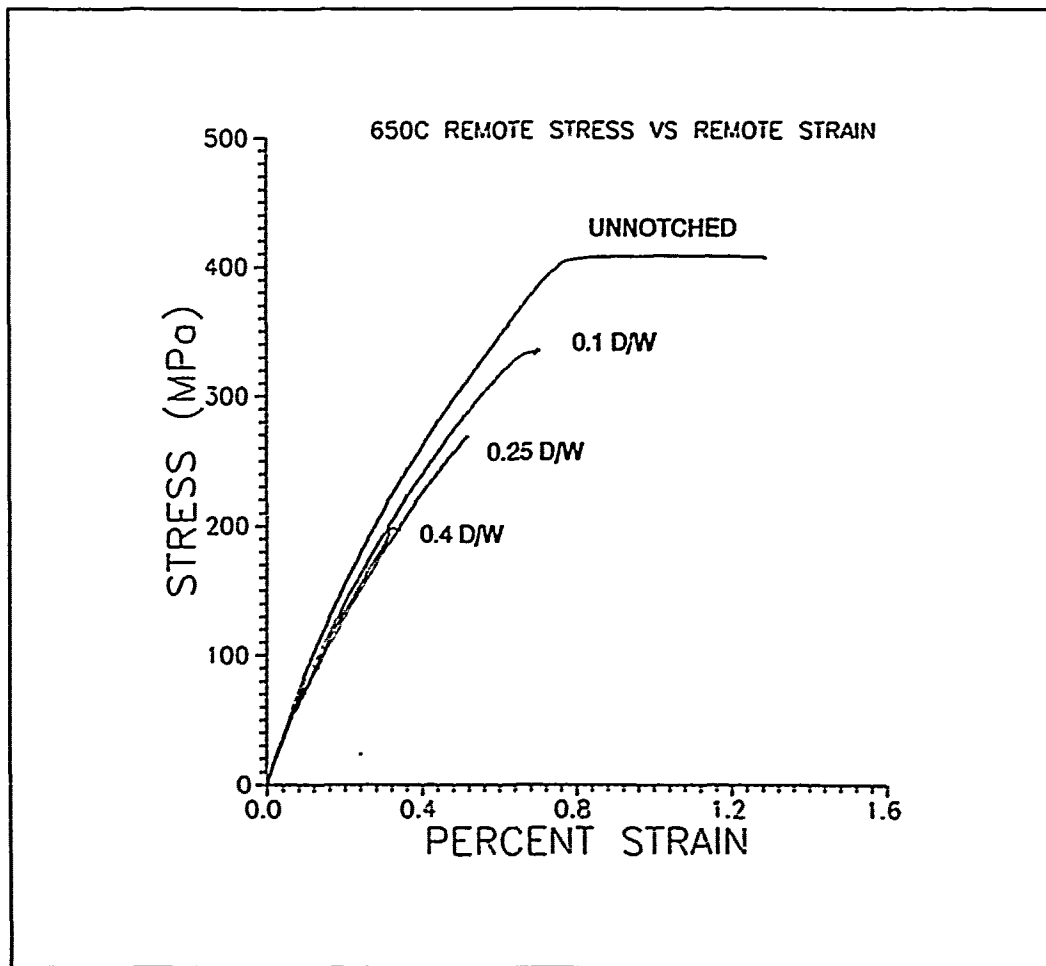
Figure 23   Remote Stress vs Remote Strain - 650°C

70

24 shows a drastic change in behavior just prior to failure. This last portion of the curve is plastic behavior of the matrix after the fibers have failed and are pulling out of the matrix. Figure 16 and other photographs below with necking of the failed elevated temperature specimens also show this plastic behavior.

The nonlinearity due to debonding seen at room temperature was present at elevated temperature as well. Figure 25 shows that the change began at a stress of 50 MPa. This is about the same stress at which the debonding was seen at room temperature.

650°C Failure Stresses. Figure 26 shows failure stresses plotted against D/W ratio for the elevated temperature tests. The format is the same as Figure 21 and the data follows the same trend as well. The complexity of testing at 650°C has introduced a little more scatter in the data, but the values are within 12% of the average stress for each hole size. All data points are again below the line for net section strength showing that the material is notch sensitive.

Table VI presents the data for all the elevated temperature tests. Note that these failure stresses are far below the corresponding D/W values seen at room temperture. To clearly show the difference between the strengths at the
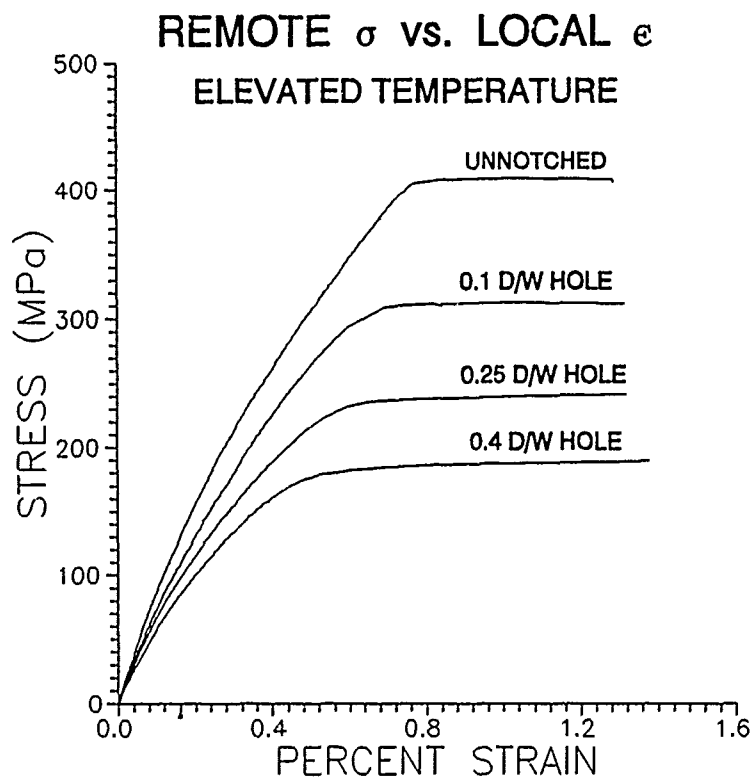
Figure 24 Remote Stress vs Local Strain – 650°C
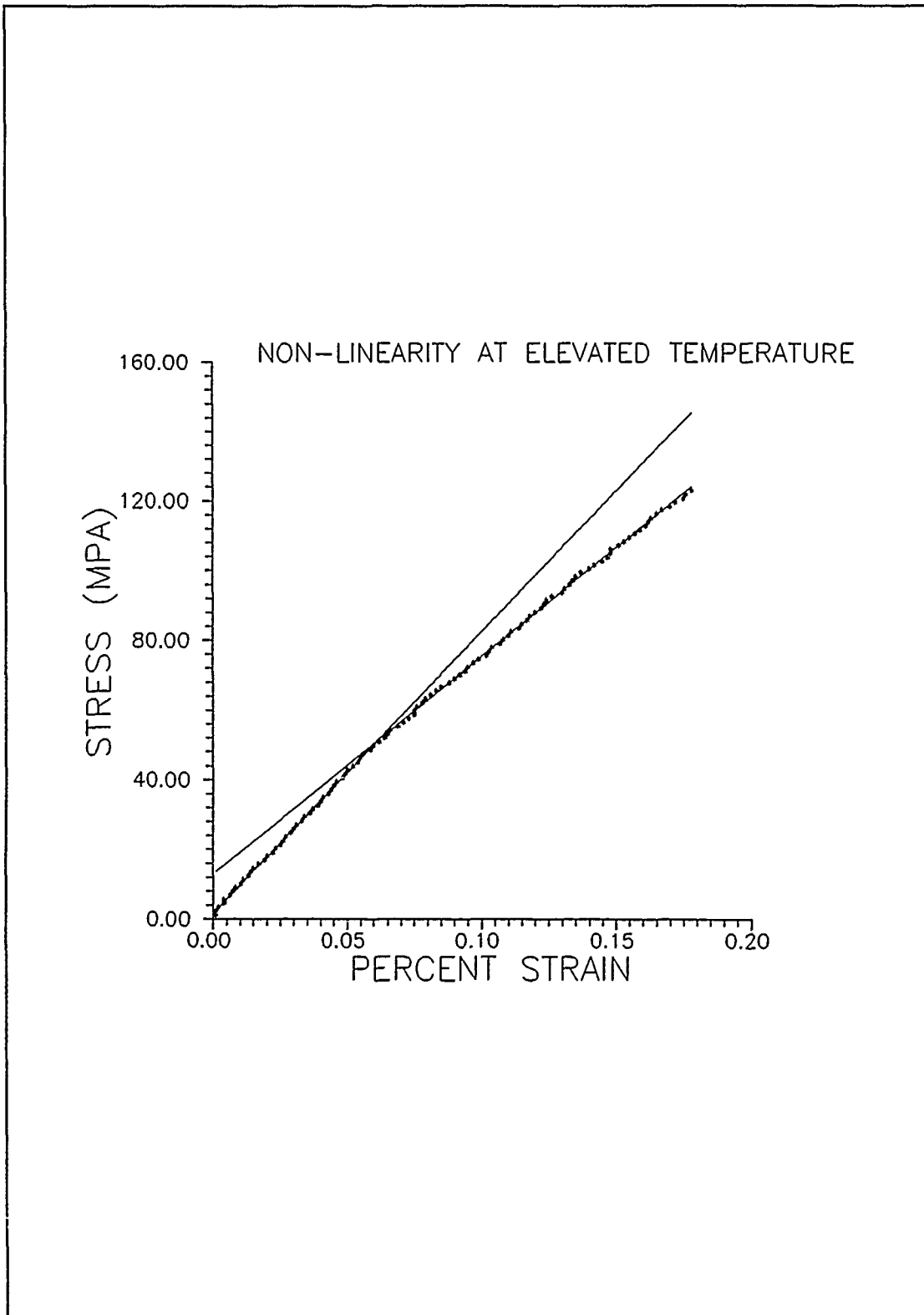
Figure 25 Nonlinearity of Rem. Stress vs. Rem. Strain 650°c

73
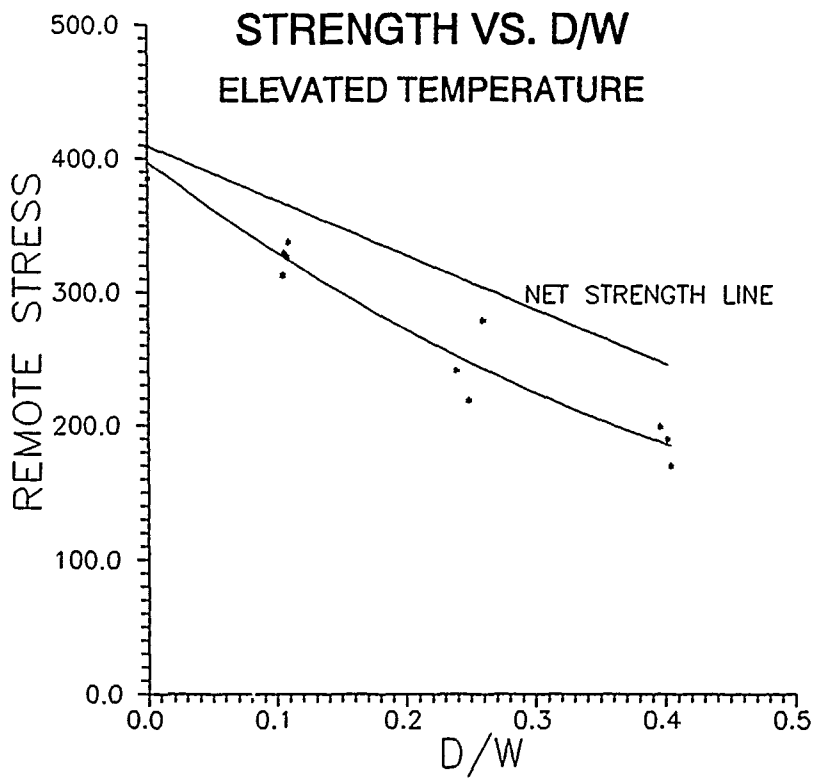
Figure 26 Failure Stresses vs. D/W for 650°C Tests

74

Table VI Elevated Temperature Tensile Test Data

SPECIMEN	LOAD (N)	DIAM (CM)	D/W	AREA (CM)	STRESS (MPa)
#2	9786	0.000	0.0000	0.2390	409.4
#20	8985	0.000	0.0000	0.2334	385.0
#26	7326	0.132	0.1043	0.2345	312.5
#7	7722	0.136	0.1089	0.2289	337.4
#24	7664	0.133	0.1054	0.2329	329.0
#13	7562	0.137	0.1080	0.2316	326.5
#14	5071	0.315	0.2482	0.2320	218.5
#23	5622	0.302	0.2391	0.2334	240.8
#22	6490	0.328	0.2596	0.2331	278.4
#27	4417	0.508	0.4019	0.2334	189.2
#15	4595	0.502	0.3958	0.2315	198.5
#16	3928	0.513	0.4040	0.2316	169.6

two temperatures Figure 27 presents absolute failure strengths for both temperatures. The normalized section area stresses are presented in Figure 28. The normalized section area strengths show a pattern similar to Figure 22 for the room temperature normalized strengths.

The difference in tensile strength at 650°C is primarily caused by the weaker matrix. Investigation of failure progression will show further effects caused by the weakened matrix at the higher temperature.

Failure Progression

This section examines the failure progression of specimens containing holes. Fracture surfaces and acoustic emission are first addressed independently. The room temperture and elevated temperature tests are discussed separately for each case and then a comparison is made. After the evidence is examined a discussion of the failure sequence at each temperature is presented. Remember that the first step in the failure is the debonding which was discussed in the previous chapter. If the interface for the off-axis fibers did not fail, the 45° fibers would certainly contribute much more to the strength at both temperatures and influence the fracture process.

The disparity in the ductility of the matrix and fibers was discussed above. As-delivered SCS-6/Beta 21S has a matrix with 20% failure strain and fibers which fail at less
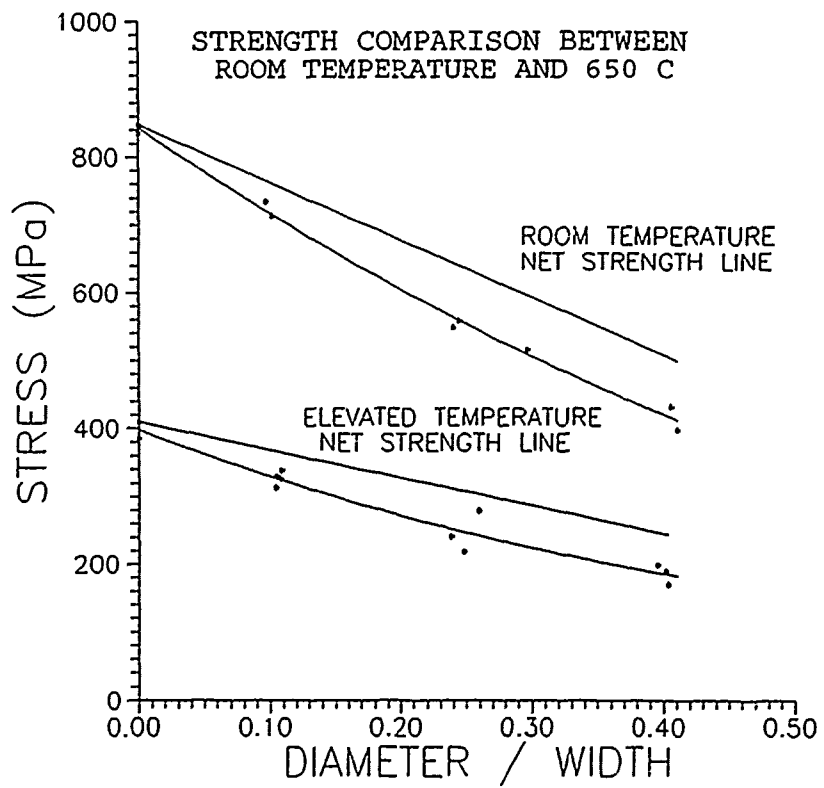
Figure 27   Absolute Strengths for All Tensile Tests

77

LOCAL STRENGTH vs. D/W
ELEVATED TEMPERATURE
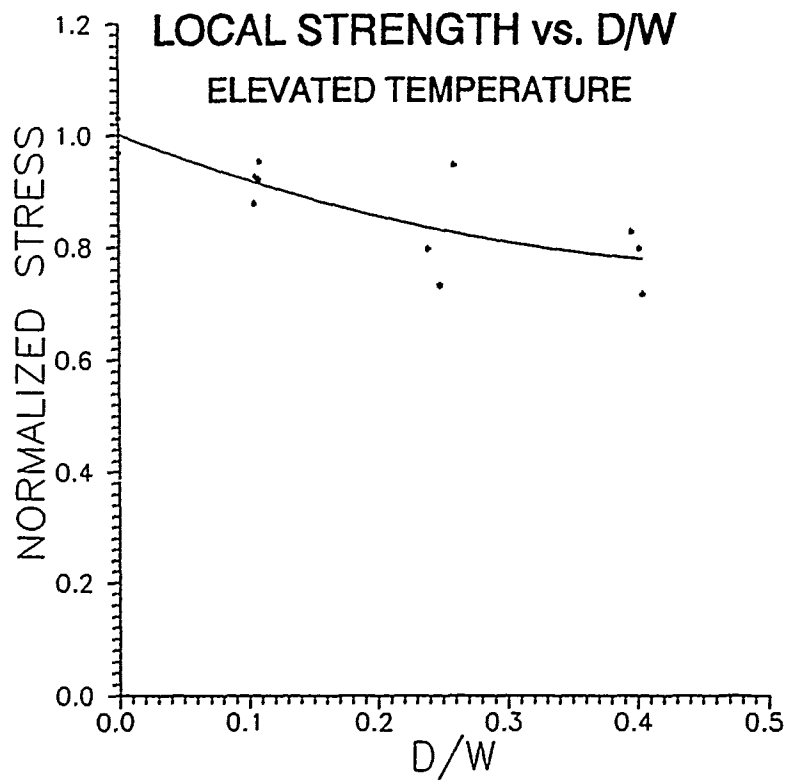
Figure 28 Normalized Section Area Strengths at $650^{\circ}C$

EXTENSOMETER STRAIN
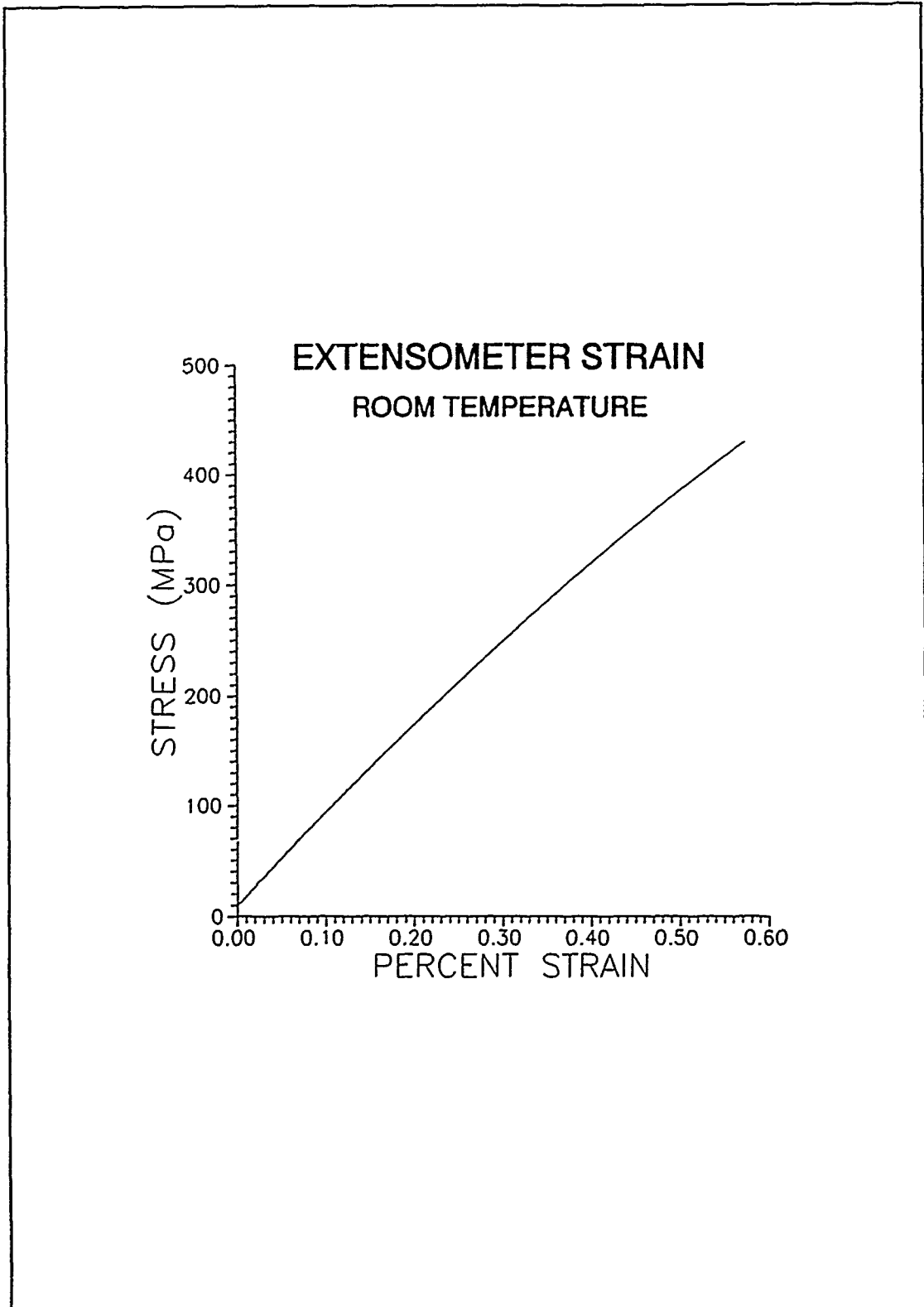
ROOM TEMPERATURE

Figure 29   Stress vs. Extensometer Strain Around the Hole

than 1% strain. Figure 29 shows the remote stress vs. the strain of an extensometer surrounding the hole for a room temperature test. The curve is not perfectly linear to failure after the debonding, but it is close. Certainly it does not look like a typical stress vs. strain curve for a metal specimen taken all the way to failure. The flattening of the curve which is typical of metals as they yield near failure is not observed. The photograph in Figure 30 shows a failed room temperature specimen, which has a D/W of about 0.25. Notice that specimen does not reduce in area near the fracture surface, as one would expect if a material yielded significantly. The hole is circular or very nearly so even after fracture.

Fracture Surfaces

Fracture Surfaces for Room Temperature. Selected samples of fractured specimens were carbon coated and examined using a scanning electron microscope. The fracture surfaces of the largest and smallest hole sizes are reviewed.

Figure 31A shows the fracture surface for the D/W of 0.4 specimen. The hole is at the very left of the picture. The only evidence of fiber pullout is seen in the 45° fibers which are debonded long before failure. The arrow shows the location for the higher magnification picture presented in Figure 31B.
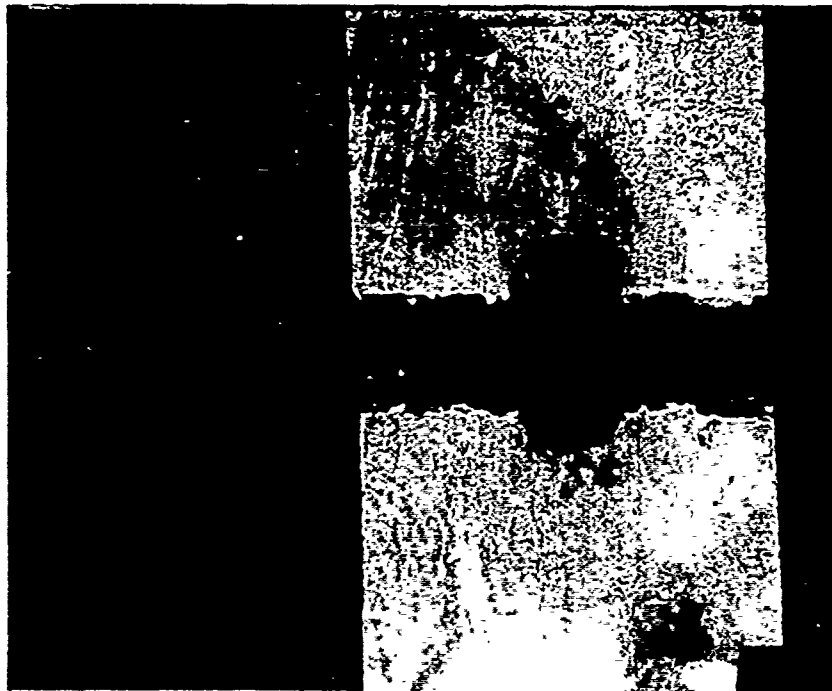
Figure 30   Photograph of Fractured Room Temperature Specimen
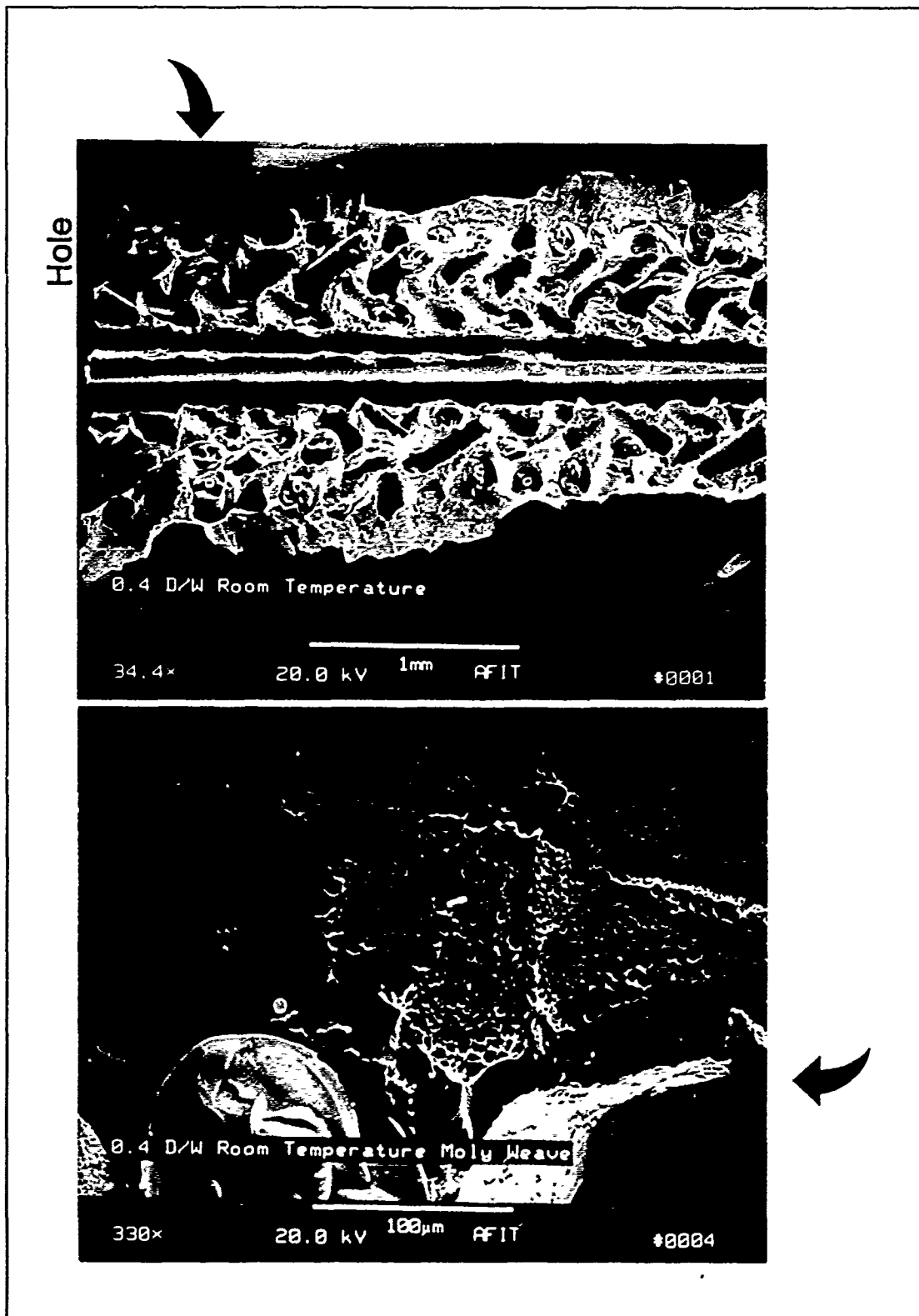
Figure 31 A (TOP) & B Fracture Surface of 0.4 D/W Specimen RT

Figure 31B shows several characteristics typical of the room temperature fracture surfaces. The arrow points to the light colored material near the fibers. This is the molybdenum wire used to hold the SCS-6 fibers in place during manufacturing. Many fracture surfaces showed this wire around the zero degree fibers. Khobaib and others have documented molybdenum as a weak point in metal matrix composites (22). Overall, the dimpled ductile fracture seen here dominates the room temperature fracture surfaces.

Figure 32 A & B show the same type of photographs for a 0.1 D/W specimen. There is very little fiber pullout and the fracture surface in Figure 32B again shows primarily ductile fracture.

While the room temperature tests showed very little yielding, the elevated temperature tests showed necking near the failure region. Examination of the failure surfaces and acoustic emission data indicates that the weaker matrix at 650°C changes the failure pattern although similarities exist at the two conditions.

Figure 33 compares two typical failed specimens for room temperature and elevated temperature at about two times magnification. The elevated temperature specimen on the right shows a small amount of necking and an elliptical hole, while the room temperature specimen has a nearly circular hole with no noticeable yielding.
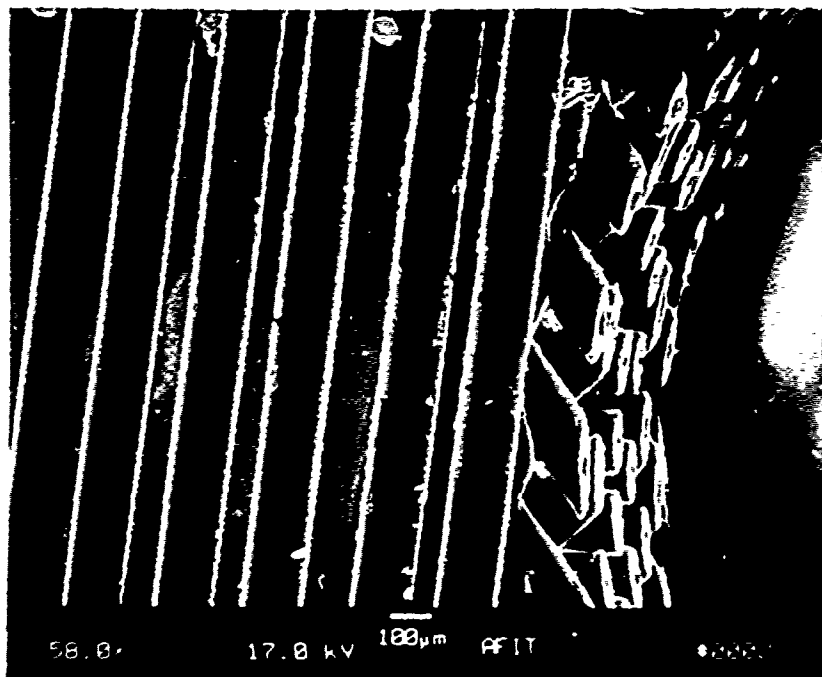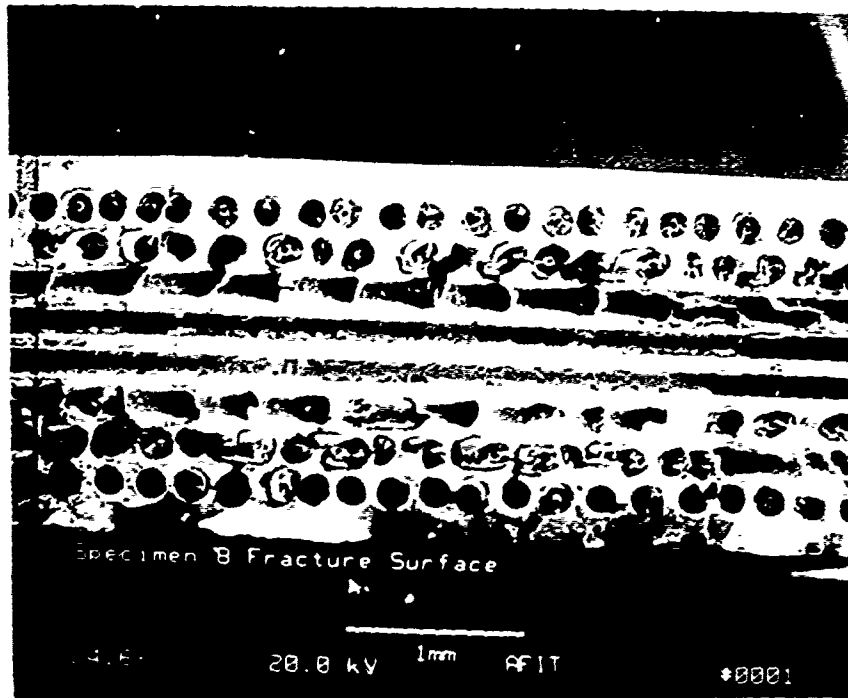
Figure 32 A (Top) & B Fracture Surface for 0.1 D/W 20°C

Figure 33 Comparison of 650°C and 20°C Failures - 0.25 D/W

650°C Fracture Surfaces. SEM photographs similar to those shown for the room temperature specimens show some difference in fracture surfaces. Figure 34 A & B contains both the overall and close-up view of the 0.4 D/W test. The higher magnification photograph shows more flat surfaces, but elongation of the specimen before failure would indicate a ductile fracture. This difference in texture was discussed above and is a function of the matrix being softer when heated to 650°C.

A 4X optical photograph presented in Figure 35 shows the increase in fiber pullout seen when a smaller hole size is tested at elevated temperature. Note that the hole is elliptical and the arrow points to protruding 90° fibers.Necking of the specimen is not obvious, but it is discernible with the aid of the vertical lines in the photo.

Acoustic Emission and Destructive Evaluation

The observations below which deal with progression of fiber failure were based in part on acoustic emission data and examination of specimens which were loaded to a certain level and then unloaded. The matrix was removed from specimens stressed to 60 and 90 percent of expected failure stress.

Room Temperature Acoustic Emission. During loading many acoustic events of greater than 90 dB amplitude and with duration exceeding 1 millisecond were observed. For
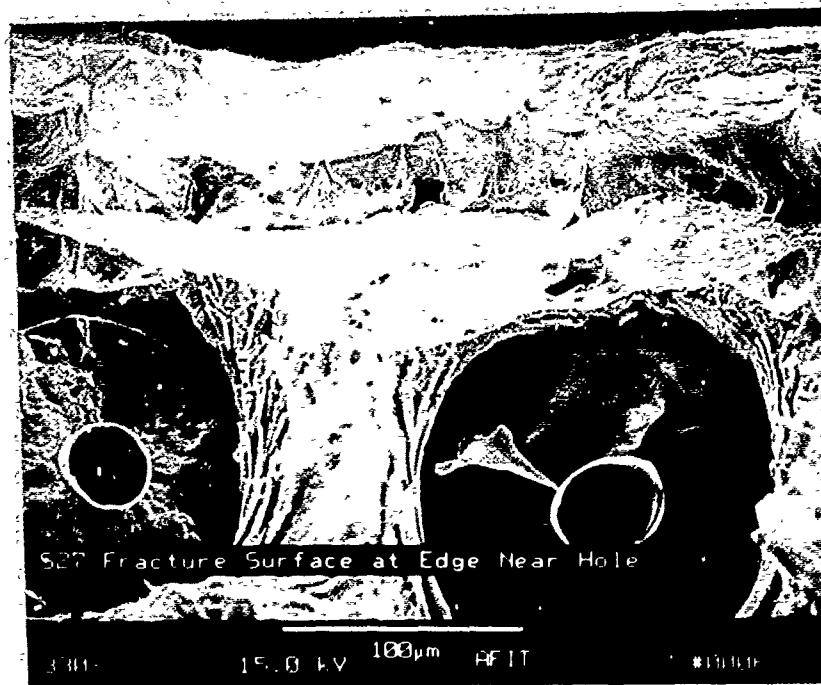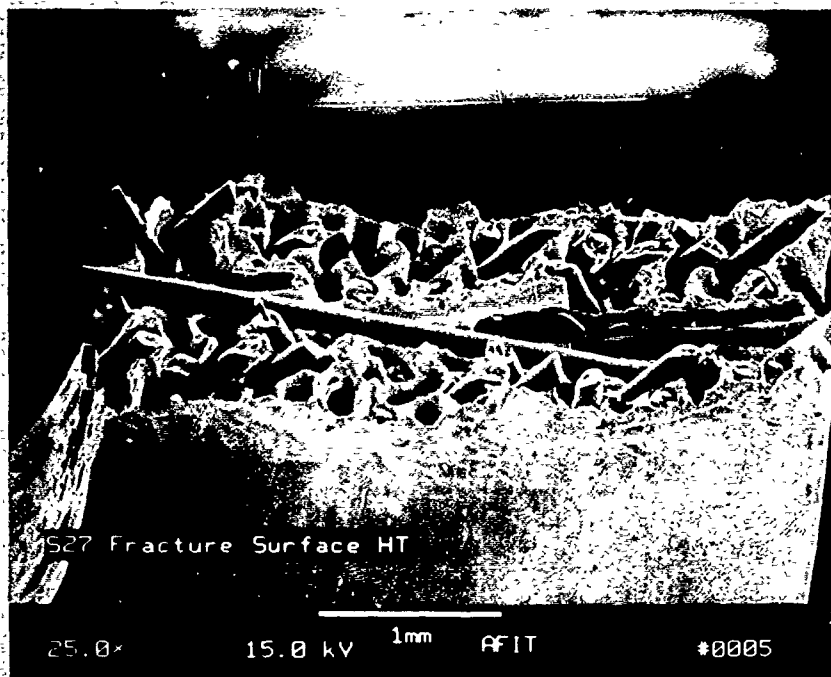
Figure 34 A (Top) & B Fracture Surface of 0.4 D/W at 650°C

Figure 35 Photograph of 0.1 D/W 650°C Specimen (4X)

88

specimens with holes these types of events are seen at below

fifty percent of the maximum load and the frequency of

occurrence increases until about 2/3 of the failure load.

The number of events is then constant or decreases until

near failure when many very large events ensue between 90

and 100 percent of load. Figure 36 shows a histogram of

hits vs. load for a specimen with a hole tested at room

temperature. The only hits shown are those above 90 dB and

duration longer than 1 ms.

Destructive Evaluation Tests. To verify the acoustic

emission data and aid in location of fiber failures,

specimens with holes were loaded to 60% and 90% of failure

stress and the matrix was electropolished away from the 0

degree fibers. Examination of the specimen loaded to 90% of

failure showed damage to only the four fibers nearest to the

hole. Figure 37 presents the hole with a view of the

damaged fibers. Notice that the extent of damage is most

significant near the 90° point of the hole and decreases for

the fibers farther from the hole. Since there are four

places on the specimen where longitudinal fibers border the

hole, each was examined. This pattern was consistent except

that damage to the fourth fiber varied. No cracks were

found beyond the fourth fiber from the hole.

Figure 38 shows two SEM photographs of the fibers at

higher magnification. The relatively equal spacing of the
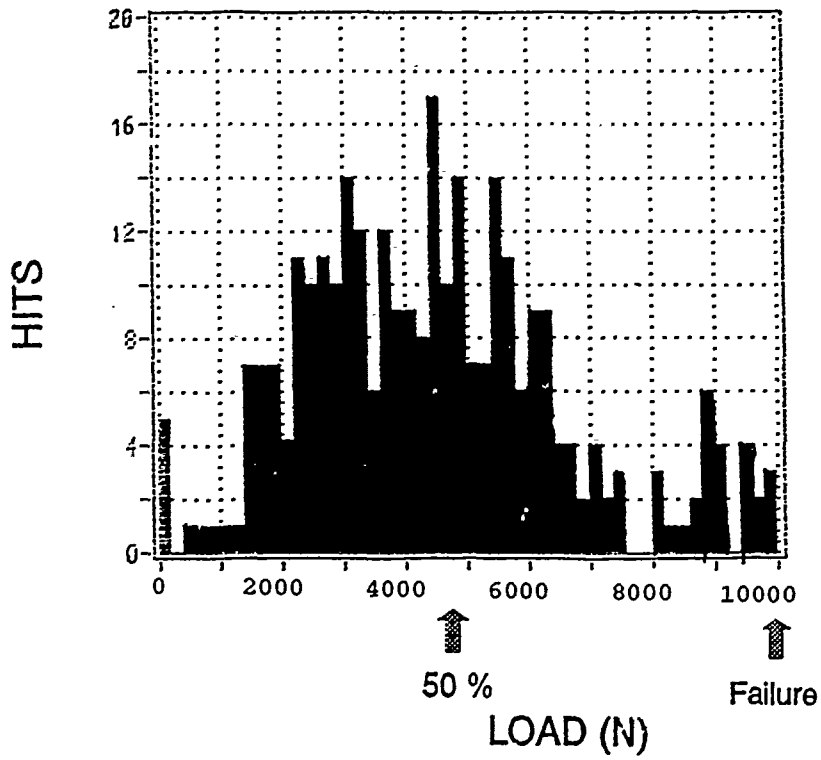
Figure 36 Acoustic Emission of Hits vs. Load at Room Temp.
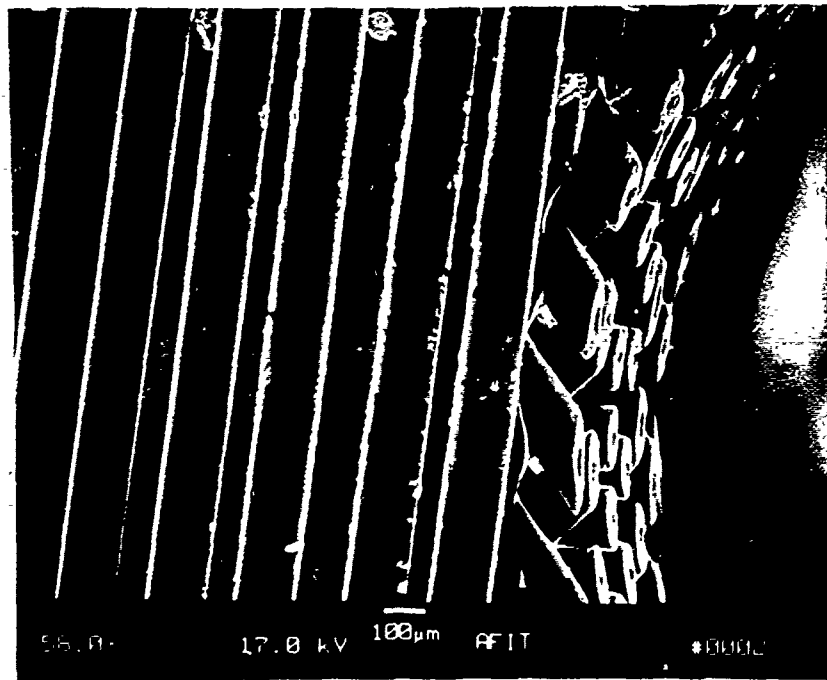
Figure 37 Damage to Fibers Near the Hole for 90% Failure

91
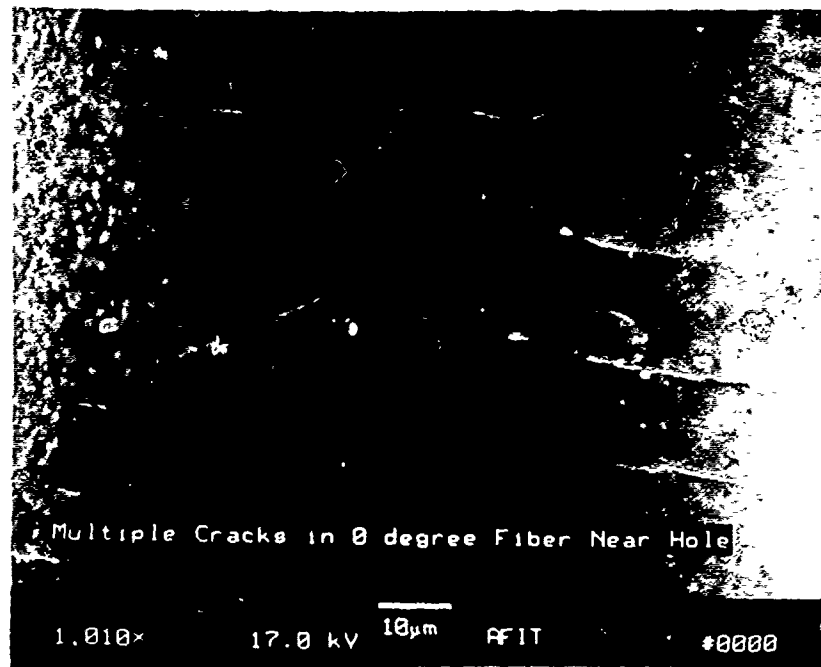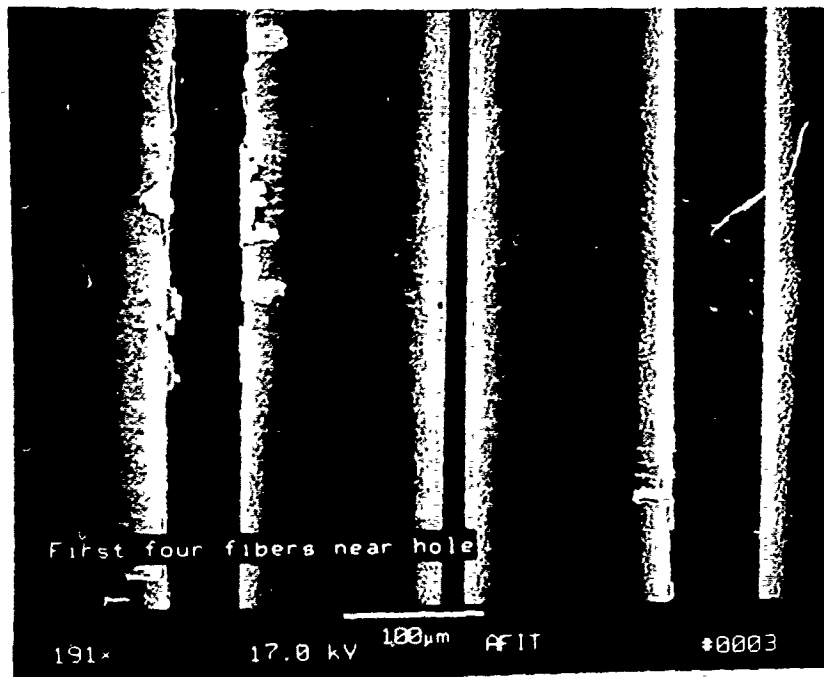
Figure 38 Fiber Damage and Equally Spaced Cracks

cracks is worth noting. These multiple cracks show that the
0° fibers are certainly not debonded. The stress to fail
the fiber at multiple sites has to come from an intact
interface. The fourth fiber shows no damage in this
section.

The partial loading up to 60% of failure stress brought
the specimen through most of the first cluster of high
amplitude hits seen in Figure 37. Soon after this point the
number of large events in a given time decreases or remains
constant. Examination with SEM revealed many fractures of
the single fiber next to the hole. No other fibers showed
cracks. Figure 39 shows several cracks in a single fiber
next to the hole. The difference in damage between these
two tests strongly supports notch sensitivity. Apparently
the fibers next to the hole fail first and then as the load
increases each successive fiber fails as the damage zone
enlarges away from the hole. The stress concentration acts
to continue the damage away from the hole.

Elevated Temperature Acoustic Emission. Acoustic emission
data was collected for elevated temperature tests and showed
a different pattern for the long duration high amplitude
events. High temperature tests show a very large number of
huge events in the 10% of load preceding failure, as shown
in Figure 40. The stress concentration at the hole creates
more events at lower loads than the specimen without a hole
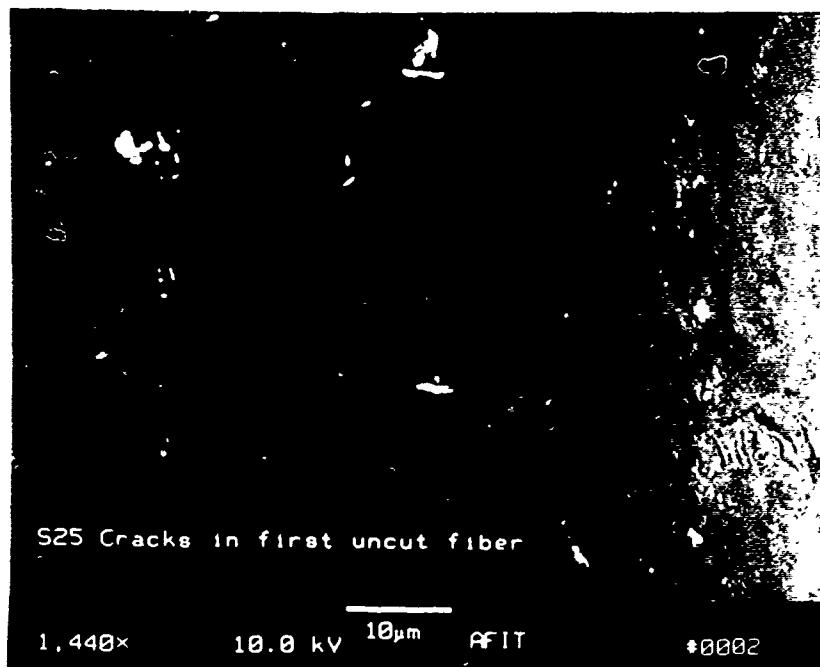
Figure 39 Cracks in Single Fiber Next to the Hole

94

showed, but most of the significant events occurred in the last 10% before failure.

Acoustic Emission Comparison. In the room temperature tests the number of fiber hits in the last 5% of load preceding failure is about one tenth the number of hits due to fiber failure for the $650^{O}C$ tests. For both tests these large events begin at a remote stress of about 200 MPa. For the room temperature test this is less than half the failure stress, but for the $650^{O}C$ test 200 MPa is close to failure. This indicates that even though the first fibers fail at roughly the same stresses for the $20^{O}C$ and $650^{O}C$ tests, the matrix absorbs the extra load at room temperature and is unable to at high temperature. In $650^{O}C$ tests this results in a high percentage of 0 degree fibers failing in a short time causing failure of the 0 degree ply and the specimen.

Discussion of Failure Progression. The discussion which follows explains the fracture sequence at both temperatures. The difference in fracture appearance is addressed including the fiber pullout. In every test the fracture began at the maximum tensile stress point of 90 degrees from the top of the hole. This indicates that a stress concentration is indeed present and creates failure of the fibers close to the hole. The strong matrix prevents failure of the specimen from just the failure of these few fibers.
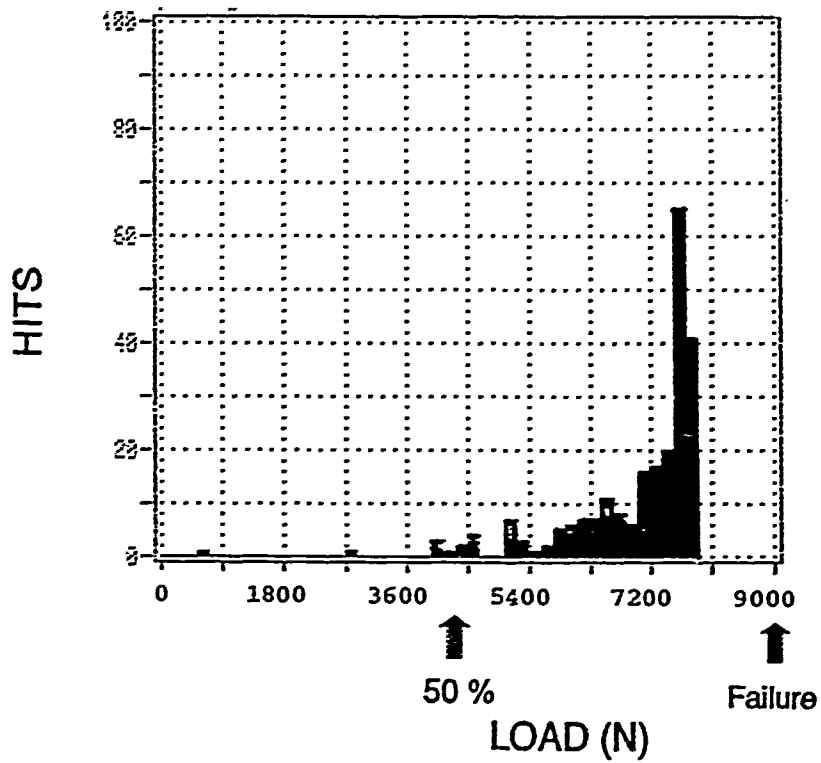
Figure 40   Acoustic Emission for 650°C With a Hole

96

Garrett and Harmon categorize failures of metal matrix composites with holes based on the strength of the matrix relative to the fibers. They divide materials into weak matrix and strong matrix systems (23). In weak matrix systems they predict failure of the first fiber will result in the failure of the ply. In strong matrix systems many fibers must fail before the ply fails because the matrix is strong enough to bear the additional load and prevent further deformation. In their work they categorized titanium matrix composites as strong matrix systems (23).

The constant or decreasing frequency of fiber failures between 60 percent and 90 percent of load supports the strong matrix argument discussed by Garrett and Harmon. The stress concentration near the hole creates local strains well above the far field strain, as shown earlier in Figure 18. These local strains reach a point exceeding the 0.8 percent required to fail the SCS-6 fibers near the hole. The laminate does not fail because Beta 21S is strong enough to absorb the load as the strain increases. The investigation of partially loaded specimens showed that these failures at low loads begin at the fiber nearest to the hole and progress outward. As the size of the damage zone grows with increasing load the matrix bears more and more load by deforming a greater distance. This process goes on until the stress concentration has created multiple

fractures of the fibers in the damage zone. At this point of the loading, the stress in the small damage zone is carried almost entirely by the matrix and few fibers are failing anywhere in the material.

Figure 41 shows the AE hits vs. load for the test to 90% of failure load discussed above. The data was filtered to show only the hits typical of fiber fracture. Note the decrease in activity at 7000 N and increase in the number of hits just before the test was stopped. The early activity is the damage to the fibers near the hole, as seen above in Figure 37. The stress concentration fails the fibers near the hole, but the strain in the remaining cross section is not high enough to fail the other fibers. The decrease in acoustic activity reflects the end of fiber damage near the hole. The matrix is now carrying the load near the hole. The increase in acoustic activity at 10,500 N may be the onset of fiber failures farther from the hole. As the load increases, the entire section area eventually reaches the failure strain of the fibers.

Figure 36 shows the same pattern for acoustic emission activity, but since the specimen is tested all the way to failure there are more hits at the end of the test. The fiber hits in the final 10% of the load reflect damage far from the hole. Many fibers in the rest of the cross section must fail at that time. After many fibers have failed, the
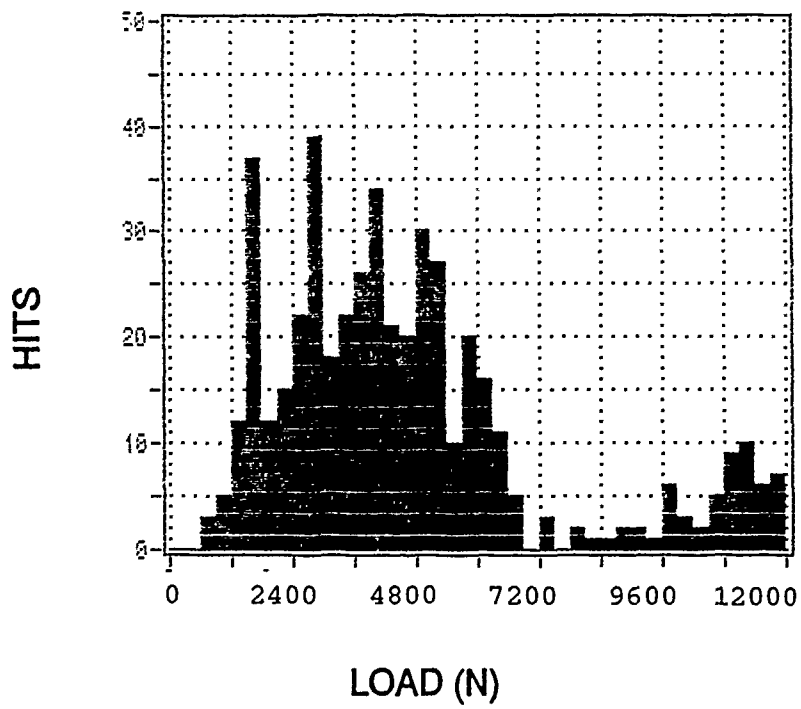
Figure 41 Acoustic Emission for Test to 90% of Failure Stress

matrix at the hole reaches failure stress. The matrix rapidly fractures at right angles to the load direction. For fibers which have multiple fractures already, the fiber crack closest to the matrix failure becomes the fiber failure surface. The multiple fractures of single fibers shown in Figure 38 were caused by the strong fiber-matrix interface of the 0° fibers. As fracture occurs the strong matrix and interface enable a straight fracture surface. If no crack exists in the fiber near the path of the failure surface, the matrix and interface are strong enough to hold the fiber and break it in the plane of the matrix fracture surface. Therefore, little fiber pullout is seen at room temperature and the fractures are very straight as seen in Figure 42.

The matrix is much weaker at elevated temperature, but acoustic emission data indicate that SCS-6/Beta 21S is still a strong matrix system at 650^OC. As noted earlier, only 25% of the strength remains at 650^OC. One-fourth of the major acoustic events occur well before failure, so by Garrett's definition a strong matrix system exists. At room temperature when the fibers fail they are held from significant deformation by the matrix stiffness. This results in multiple fractures of the fiber as the load continues to increase. At elevated temperature much more deformation in the matrix is required to absorb the extra
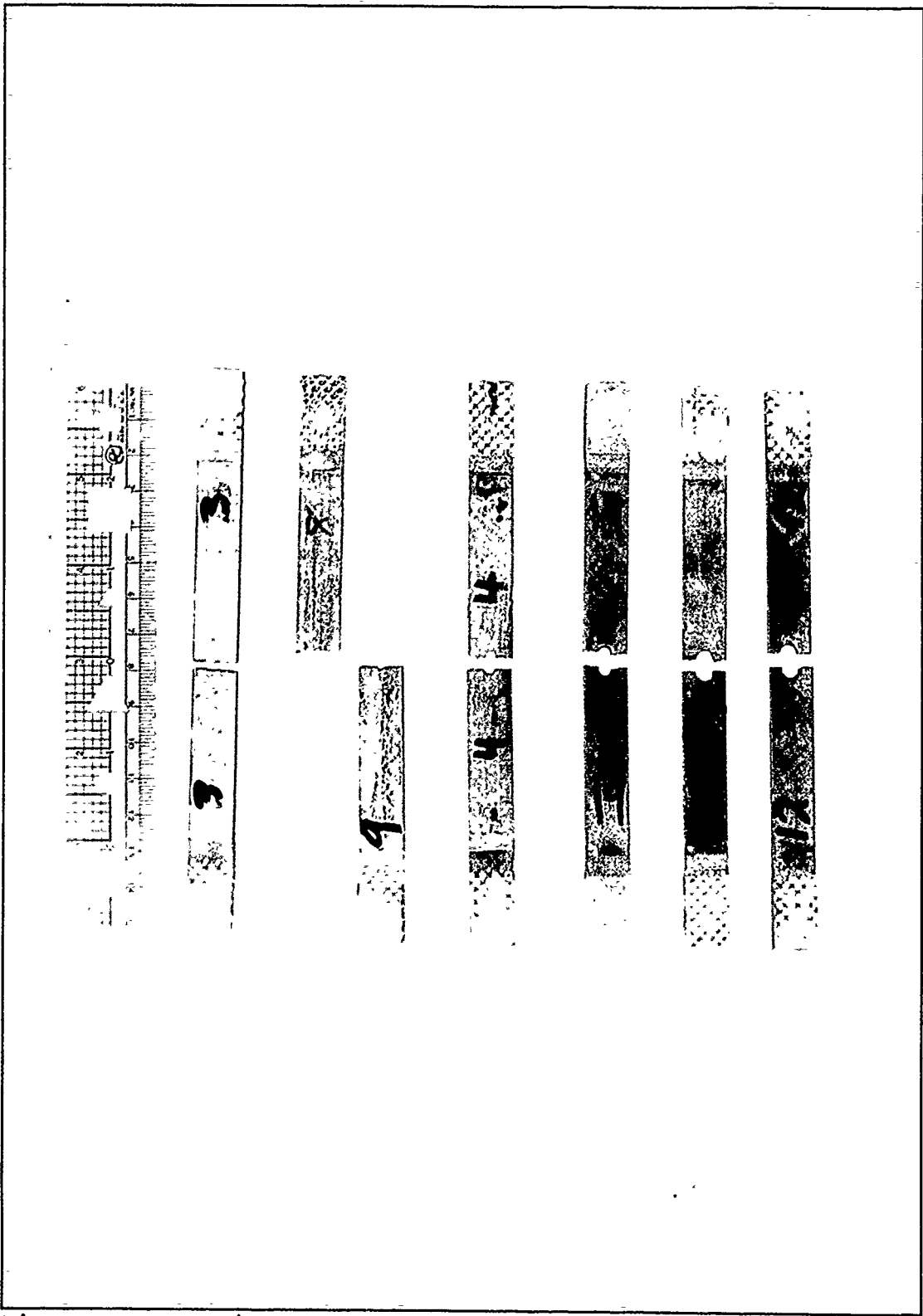
Figure 42 Specimens Fractured at Room Temperature

101

load when a fiber fails. This additional deformation means there is less stress on the failed fiber. At room temperature the fibers fractured many times at small intervals, because the matrix was stiffer. A long portion of matrix is required at elevated temperature to create the stress required to fail the fiber a second time, so many fibers fail at only one point along their axis. Figure 43 shows several specimens which were failed at 650°C. The following paragraphs describe why the path of the fracture is so jagged and why fiber pullout occurs.

Specimens with larger holes failed at lower stresses and show far less fiber pullout and necking than specimens with small holes. In the large hole sizes the failure of only a few fibers at the stress concentration quickly raised the stress in the remaining fibers to the failure level. The relative size of the stress concentration is greater for two reasons. The section area is less, just because of the larger hole, and the size of the stress concentration zone increases with hole size. For a smaller hole the stress concentration occupies a far smaller portion of the cross section. This means that the rest of the section area sees higher stresses for a longer period of time and yielding of the matrix occurs. This results in fiber pullout and the jagged fracture surface.
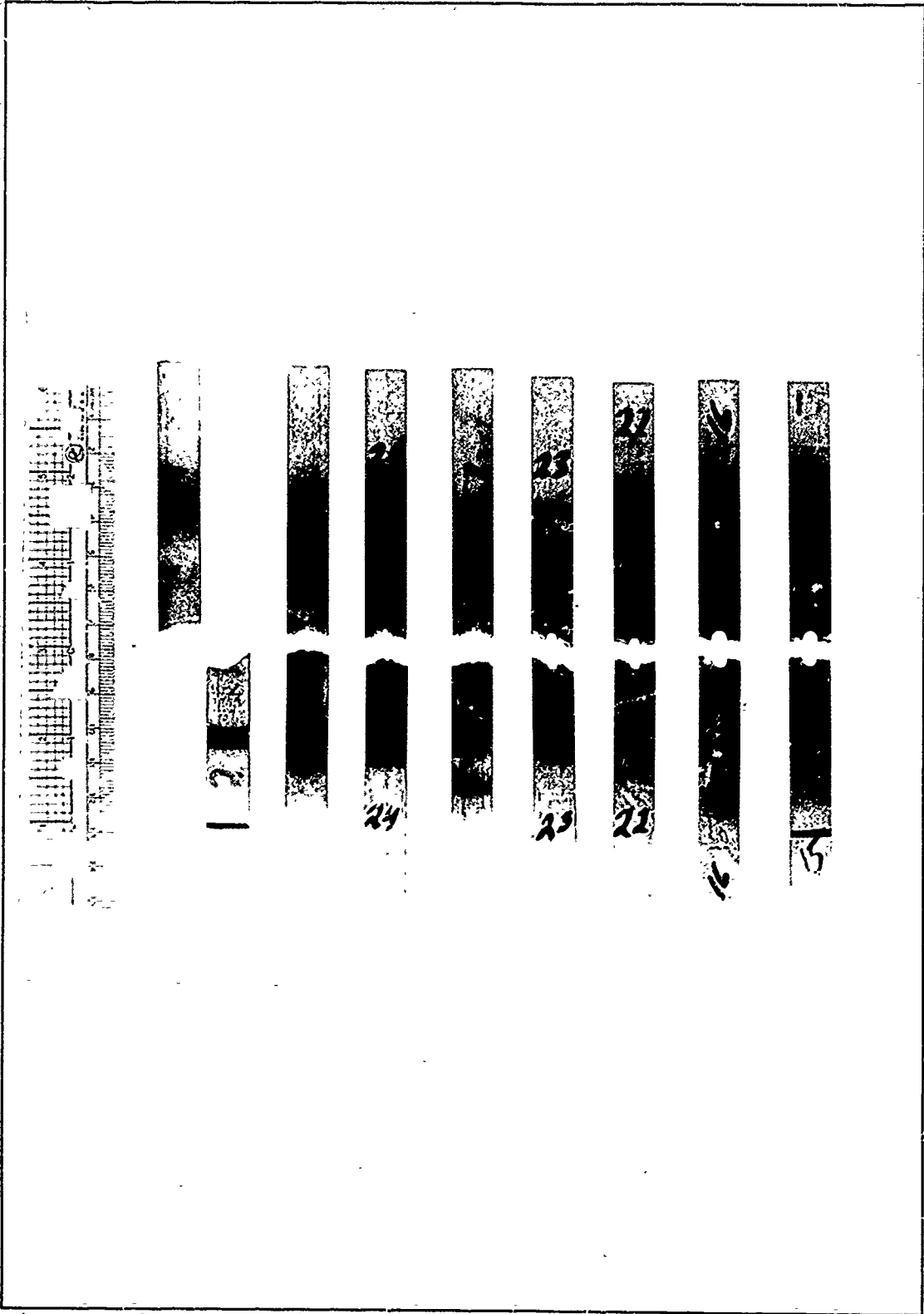
Figure 43 Specimens Fractured at Elevated Temperature

103

The weaker matrix causes the jagged fracture surface at elevated temperature. The matrix deforms readily when fibers fail near the hole and the remaining fibers realize an increase in stress. Since the fibers fail at the weakest point, the fibers far from the hole fail at some point in the area of elevated stress. This failure point may not be along the straight line perpendicular to the load direction seen for the room temperature test. Unlike room temperature, most fibers do not crack in multiple locations. The single fracture points of the failed 0° fibers determine the path of the specimen fracture surface. The fracture begins at the 90° maximum stress point of the hole. When the failed fibers are not in the plane perpendicular to the load direction containing the maximum stress point, the crack deviates from this plane. The crack grows rapidly to a fiber fracture near this plane and the matrix and off-axis fibers fail. The path between the broken 0° fibers usually follows on of the sets of 45° fibers. The path of the fracture surface continues to follow the 0° fiber failures and creates the jagged surface.

The weaker matrix also allows the fiber pullout. The rapidly advancing crack cannot follow the path to every failed fiber. The fibers which failed far from the path of the failure surface are pulled out of the matrix. At 650^oC

104

the matrix is not strong enough to hold and break a fiber which failed at some point not in the plane of fracture.

This description is supported by the stress vs. strain curves in Figure 24. The flat plastic portion of these curves indicates that the matrix is yielding rapidly after the fibers have failed. The strain where the plastic region begins is near the failure strain of the fibers. This shows that fibers are failing first, then the matrix deforms quickly and fibers pull out of the matrix and the matrix yields and fails.

Summary of Failure Progression. The stress concentration damages the fibers near the hole at both temperatures. This damage occurs well before failure of the specimen. At room temperature many other fibers fracture over the last 25% of the loading. Multiple fiber fractures and a stronger matrix at room temperature create a straight fracture surface. The weaker matrix and single fractures of fibers at elevated temperature cause a jagged fracture surface and fiber pullout.

Failure Prediction Comparison

The point stress method developed by Whitney and Nuismer was applied to analyze the failure strength data of this study (21). Tan's FWC was used. Both of these equations require a stress concentration factor. Both the bonded and unbonded stress concentrations were used and the

results are shown. Sample calculations for the finite width correction and Whitney's point stress method are presented in Appendix D.

Figure 44 shows the room temperature data with a stress concentration factor of 3.0. The critical distance is 0.98 mm. Figure 45 applies a stress concentration of 3.18 and the results are changed only slightly. The small elevation in the theoretical stress concentration factor caused by modeling the debonding has very little effect on the curve fit. The critical distance changed to 0.96 mm.

The elevated temperature data was normalized and plotted separately. The failure values at a given hole diameter are plotted in Figure 46 with the Whitney-Nuismer curve of $d_o = 0.79$ mm. Figure 47 shows the same data fit with the stress concentration set equal to 3.28 when $d_o = 0.76$ mm. The small variation of stress concentration factor seems to have very little effect on the ability of Whitney's method to fit the data.

The difference in d_o between room temperature and elevated temperature shows again the effect of the weaker matrix at 650°C. A smaller number of fiber failures near the hole creates failure of the specimen. The weaker matrix cannot absorb as much of the load as at room temperature. **Whitney-Nuismer and Destructive Evaluation**. The Whitney-Nuismer critical distance corresponds very well with the

106

WHITNEY-NUISMER POINT STRESS
ROOM TEMPERATURE SCF = 3.0
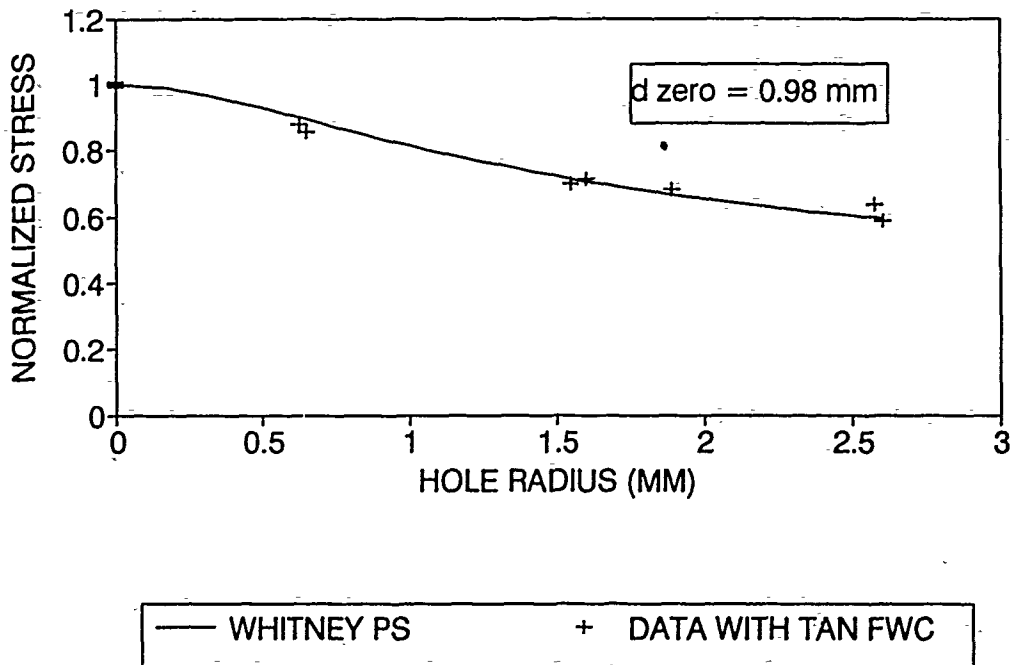
Figure 44 Whitney-Nuismer for Stress Concentration of 3.0
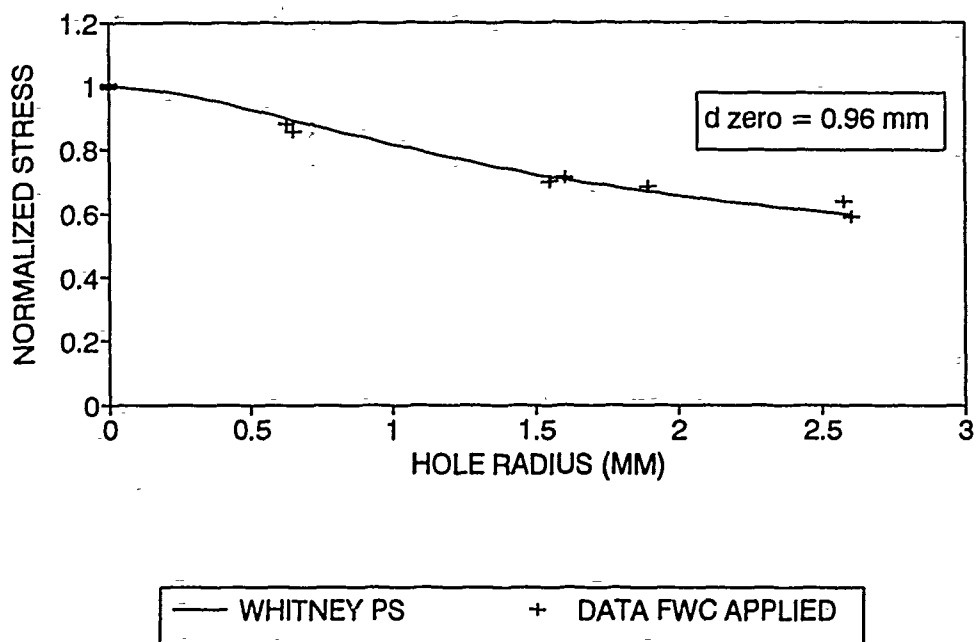
Figure 45 Whitney-Nuismer with Stress Concentration of 3.18

WHITNEY-NUISMER POINT STRESS
ELEVATED TEMPERATURE   SCF = 3

d zero = 0.79 mm

WHITNEY PS   +   DATA, WITH TAN FWC
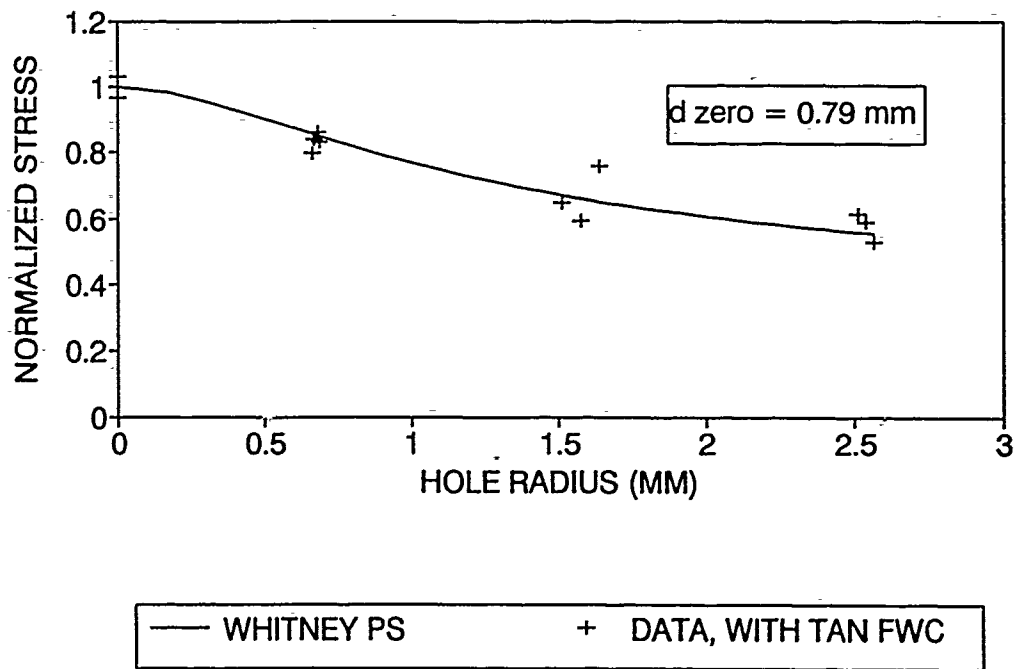
Figure 46   Whitney-Nuismer for SCF = 3 at 650°C

109

WHITNEY-NUISMER POINT STRESS
ELEVATED TEMPERATURE SCF = 3.28
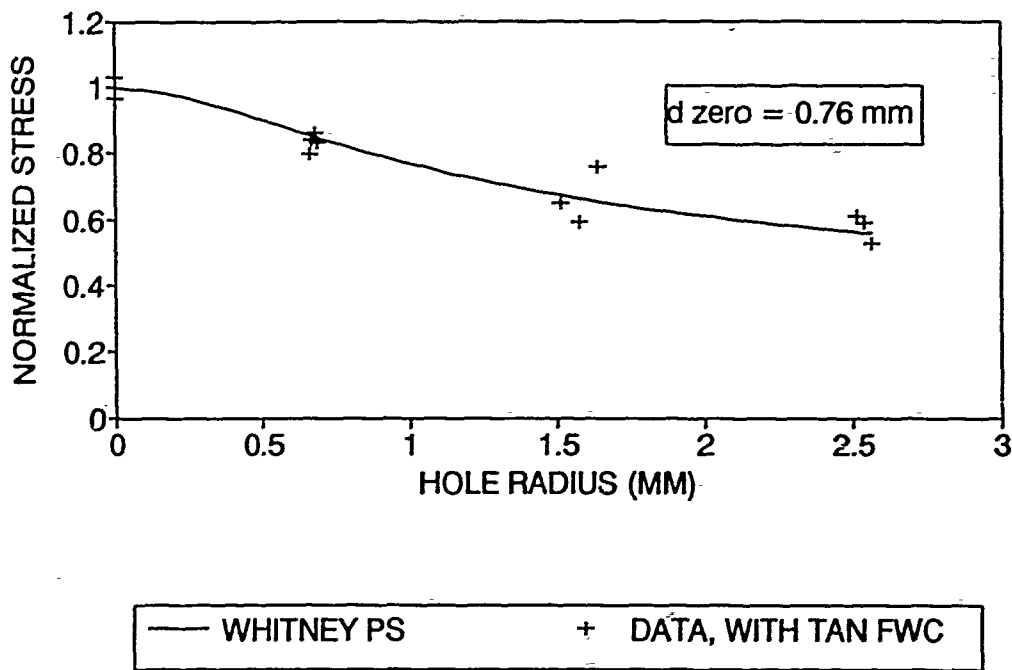
Figure 47   Whitney-Nuismer for   SCF = 3.28   650°C

damage seen in the specimen loaded to 90% of failure stress. The fiber spacing for this material is about 200 microns. This puts the fourth fiber at about 800 microns from the hole. The Whitney-Nuismer critical distance is about 960 microns from the hole edge. This means that at 90% of failure the damage zone is over 80% of the required size to fail the specimen. The fifth fiber may be the point where the stress in the damage zone and the rest of the fibers reaches the critical stress causing extensive fiber fracture and failure of the specimen. This corresponds well with the acoustic emission plots showing the increase in large acoustic events just before failure. These large acoustic events probably reflect the catastrophic failure of previously undamaged fibers outside the damage zone near the hole. These last few events often lasted more than three times the duration of any previous event with amplitudes approaching 100 dB.

The damage zone size at elevated temperature is about 80% of the value at room temperature. This correlates well with the damage progression discussions above. The damage begins at the fiber nearest the hole and progresses outward. The weaker matrix at elevated temperature would imply a smaller damage zone. The investigation earlier showed that damage to four fibers did not cause failure for the room temperature specimen which was examined. A d_0 of 0.76 mm

111

implies that damage to the fourth fiber would create failure in a specimen at 650°C. Further work may prove the Whitney-Nuismer point stress method a consistent predictor of notch effects in SCS-6/Beta 21S.

Summary

This chapter showed that SCS-6/Beta 21S is notch sensitive for both room temperature and elevated temperature. Exposing the outside fibers of specimens loaded to different percentages of the failure stress, showed that fibers fail well before the matrix shows any signs of damage. Combining this with AE data shows that at both temperatures the material can be characterized as a strong matrix system. Finally, calculation of the Whitney-Nuismer failure prediction shows that the failures of this material can be predicted quite well using the Whitney-Nuismer Point Stress technique.

VI. Conclusions and Recommendations

The following conclusions are drawn from this study:

1. The off-axis plies in SCS-6/Beta 21S $[0,\pm45,90]_s$ experience debonding of the fibers from the matrix. This occurs at stresses as low as 10% of the ultimate failure stress of an unnotched specimen.

2. For unnotched specimens and all notched specimens tested in this study the failure strength at 650°C is about half the corresponding strength at room temperature.

3. SCS-6/Beta 21S is notch sensitivite at room temperature and at elevated temperature.

4. The acoustic emission data and notch sensitivity indicate that this material is a strong matrix system both at room temperature and at 650°C. Failure of a single fiber does not cause catastrophic failure of the matrix.

5. The Whitney-Nuismer point stress failure criterion fits the failure data well when the critical distance is 0.96 mm for room temperature and $d_0 = 0.76$ mm for 650°C.

7. Exposing the fibers of specimens which had been loaded to portions of failure stress, showed a small damage zone around the hole even up to 90% of failure stress. The critical distance of the Whitney-Nuismer point stress criterion corresponds very well with the size of this damage zone.

The following recommendations are submitted as a result of this study:

1. Any additional studies with this matrix should age the material before tests begin at room temperature or elevated temperature. There is a possibility that the fiber-matrix interface was damaged by reaching temperature in only 5 minutes.

2. A similiar study with SCS-6/Beta 21S $[0,90]_{2S}$ could provide a solid basis for choosing between the two lay-ups for aerospace applications.

3. Work in the field of strengthening the interface for silicon carbide/metal matrix composites should continue.

Bibliography

1. Gambone, Mary L. _Fatigue and Fracture of Titanium Aluminides_. Allison Gas Turbine Division Final Report for Contract #F33615-85-C-5111. Materials Laboratory Wright Research and Development Center, Feb 1990.

2. Schoenberg, Ted. _Titanium Aluminide Composites - Workshop Proceedings_. "Status of CVD SiC Monofilament at Textron Specialty Materials," 7-16. WL-TR-91-4020, Materials Directorate Wright Laboratories, 1991.

3. Larsen, James J. et al. "Titanium Aluminides for Aerospace Applications," _High Temperature Aluminides & Intermetallics_, edited by S.H. Whang et al., TMS/ASM International, USA: 521-556 (1990)

4. Bania, P. J. and Parris, W. M. "Beta 21S: A High Temperature Metastable Beta Alloy," _119th TMS Annual Meeting_, Anaheim, Ca. (Feb 1990)

5. Johnson, W. S. et al. "Mechanical Characterization of Unnotched SCS-6/Ti-15-3 Metal Matrix Composites at Room Temperature," _Thermal and Mechanical Behavior of Ceramic and Metal Matrix Composites_, 193-218, ASTM STP 1080, Kennedy, Moeller, and Johnson, Ed., American Society of Testing and Materials, Philadelphia, 1990.

6. Timoshenko, Stephen P. and John N. Goodier. _Theory of Elasticity_ (Third Edition). New York: Mcgraw and Hill, 1970.

7. Lekhnitskii, S.G. _Anisotropic Plates_. Translated from the Second Russion Edition by S.W. Tsai and T. Cheorn. New York: Gordon and Breach, Science Published Inc., 1968.

8. Greszczuk, L. B. "Stress Concentrations and Failure Criteria for Orthotropic and Anisotropic Plates with Circular Openings", _Composite Materials: Testing and Design (Second Conference)_. 363-381, ASTM STP 497, American Society for Testing and Materials, 1972.

9. Mar, J. W. and Lin, K. Y. "Fracture of Boron/Aluminum Composites with Discontinuities", _Journal of Composite Materials_, 11, 405-421, (October 1977)

10. Poe C. C. Jr. and Sova J.A. "Fracture Toughness of Boron/Aluminum Laminates with Various Proportions of 0° and ±45° Plies", NASA TP-1707, November 1980.

11. Johnson, W. S. et al. "Experimental and Analytical Investigation of the Fracture Processes of Boron/Aluminum Laminates Containing Notches", NASA TP-2187, September 1983.

12. Naik, R. A. and Johnson, W. S. "Observations of Fatigue Crack Initiation and Damage Growth in Notched Titanium Matrix Composites", Proceedings of the Third Symposium on Composite Materials: Fatigue and Fracture. November 1989.

13. Jones, Robert M. Mechanics of Composite Materials, New York, Hemisphere Publishing Corporation, 1975.

14. Halpin, J. C. and Tsai, S. W. Environmental Factors on Composite Materials. AFML-TR67-423, (June 1969).

15. Williams, David B. Practical Analytical Electron Microscopy in Materials Science. Deerfield Beach, Florida: Electron Optics Pub. Co., 1984.

16. Chamis, C. C., Murthy, L. N., and Hopkins, D. A. "Computational Simulation of High-Temperature Metal Matrix Composites Cyclic Temperature," Thermal and Mechanical Behavior of Metal Matrix and Ceramic Natrix Composites, 56-69, ASTM 1080, Kennedy, Moeller, and Johnson, Ed., American Society of Testing and Materials, Philadelphia, 1990 .

17. Larsen, James J., Director Metal Matrix Composites Branch. Personal interview. Wright Laboratories, Dayton OH, 23 September 1991.

18. Khobaib, M., University of Dayton Research Institute. Personal interview. Wright Laboratories, Dayton OH, 30 October 1991.

19. Roman, Itzhak, Visiting Scientist, Wright Laboratories. Personal Interviews. Materials Directorate Wright Laboratories, WPAFB OH, 15 Sep through 30 October 1991.

20. Tan, Seng C. "Finite-Width Correction Factors for Anisotropic Plate Containing a Central Opening," Journal of Composite Materials, 22: 1080-1097 (November 1988).

21. Whitney, J. M. and Nuismer, R. J. "Stress Fracture for Laminated Composites Containing Stress Concentrations," Journal of Composite Materials, 8. (July 1974).

22. Khobaib, M. "Creep Behavior of SCS-6/Ti-24Al-11Nb Composite," _Titanium Aluminide Composites - Workshop Proceedings_. 450-466. WL-TR-91-4020, Materials Directorate Wright Laboratories, 1991.

23. Garrett, A. S. and Harmon, D. M. "Thermomechanical Load History Effects in Metal Matrix Composites," Air Force Materials Laboratory, Air Force Systems Command. Contract F33615-87-C-3219 with McDonnell Aircraft Company. Wright-Patterson AFB OH, October 1988.

24. Awerbuch, J. and Madhukar, M. S. "Notched Strength of Composite Laminates; Prediction and Experiments - A Review," _Journal of Reinforced Plastics and Composites,4_. (1985).

APPENDIX A

Laminate Properties of Quasi-isotropic SCS-6/Beta 21S

Classical laminated plate theory is applied using the lamina properties. This results in a Young's modulus which correlates closely with the initial experimental modulus. Following this, the Halpin-Tsai and total discount methods are used to model the modulus after debonding.

Engineering Constants for as delivered SCS-6/Beta 21-S

$$E1 := 194 \cdot 10^9 \quad E2 := 136 \cdot 10^9 \quad v12 := .27 \quad G12 := 48 \cdot 10^9$$

$$S := \begin{bmatrix} \dfrac{1}{E1} & \dfrac{-v12}{E1} & 0 \\ \dfrac{-v12}{E1} & \dfrac{1}{E2} & 0 \\ 0 & 0 & \dfrac{1}{G12} \end{bmatrix} \qquad q := S^{-1}$$

$$q = \begin{bmatrix} 2.044 \cdot 10^{11} & 3.87 \cdot 10^{10} & 0 \\ 3.87 \cdot 10^{10} & 1.433 \cdot 10^{11} & 0 \\ 0 & 0 & 4.8 \cdot 10^{10} \end{bmatrix}$$

Now the q matrix is rotated to match the other lamina.

$$\theta := \frac{\pi}{4} \qquad t(\theta) := \begin{bmatrix} \cos(\theta)^2 & \sin(\theta)^2 & 2 \cdot \sin(\theta) \cdot \cos(\theta) \\ \sin(\theta)^2 & \cos(\theta)^2 & -2 \cdot \sin(\theta) \cdot \cos(\theta) \\ -\sin(\theta) \cdot \cos(\theta) & \sin(\theta) \cdot \cos(\theta) & \cos(\theta)^2 - \sin(\theta)^2 \end{bmatrix}$$

$$qbar45 := t(\theta)^{-1} \cdot q \cdot \left[t(\theta)^{T^{-1}} \right]$$

$$\theta := \frac{-\pi}{4} \qquad qbarm45 := t(\theta)^{-1} \cdot q \cdot \left[t(\theta)^{T^{-1}} \right]$$

$$\theta := \frac{\pi}{2}$$

$$qbar90 := t(\theta)^{-1} \cdot q \cdot \left[t(\theta)^{T^{-1}} \right]$$

118

a := .000457·(q + qbar45 + qbarm45 + qbar90)

$$
b := \begin{bmatrix} 0 & 0 & 0 \\ 0 & 0 & 0 \\ 0 & 0 & 0 \end{bmatrix}
\qquad
a = \begin{bmatrix} 3 \cdot 10^{8} & 8.865 \cdot 10^{7} & -2.415 \cdot 10^{-10} \\ 8.865 \cdot 10^{7} & 3 \cdot 10^{8} & 1.953 \cdot 10^{-9} \\ -2.415 \cdot 10^{-10} & 1.953 \cdot 10^{-9} & 1.057 \cdot 10^{8} \end{bmatrix}
$$

Now we need the d matrix and to make the equation all fit on one line we will define some coefficients. This converts the distances from inches to meters.

$$
d4 := \frac{.036}{39.37} \qquad d3 := \frac{.027}{39.37} \qquad d2 := \frac{.018}{39.37} \qquad d1 := \frac{.009}{39.37}
$$

qb := qbar45   hb := qbarm45   fb := qbar90

$$
d := \frac{2}{3}\left[\left[d4^{3} - d3^{3}\right]\cdot q + \left[d3^{3} - d2^{3}\right]\cdot qb + \left[d2^{3} - d1^{3}\right]\cdot hb + d1^{3}\cdot fb\right]
$$

$$
d = \begin{bmatrix} 93.336 & 23.782 & 1.46 \\ 23.782 & 75.811 & 1.46 \\ 1.46 & 1.46 & 28.523 \end{bmatrix}
$$

big1 := augment(a,b)   big2 := augment(b,d)

big := augment(big1^{T},big2^{T})

This matrix represents the laminate stiffness.

$$
big = \begin{bmatrix} 3 \cdot 10^{8} & 8.86 \cdot 10^{7} & -2.42 \cdot 10^{-10} & 0 & 0 & 0 \\ 8.86 \cdot 10^{7} & 3 \cdot 10^{8} & 1.95 \cdot 10^{-9} & 0 & 0 & 0 \\ -2.42 \cdot 10^{-10} & 1.95 \cdot 10^{-9} & 1.06 \cdot 10^{8} & 0 & 0 & 0 \\ 0 & 0 & 0 & 93.34 & 23.78 & 1.46 \\ 0 & 0 & 0 & 23.78 & 75.81 & 1.46 \\ 0 & 0 & 0 & 1.46 & 1.46 & 28.52 \end{bmatrix}
$$

$$
NM := \begin{bmatrix} 165 \cdot 10^{6} \cdot .001829 \\ 0 \\ 0 \\ 0 \\ 0 \\ 0 \end{bmatrix}
$$

119

$$\epsilon := \text{big}^{-1} \cdot NM$$

$$\epsilon = \begin{bmatrix} 0.001 \\ -3.258 \cdot 10^{-4} \\ 0 \\ 0 \\ 0 \\ 0 \end{bmatrix} \qquad E := 165 \cdot \frac{10^6}{.0011} \qquad E = 1.5 \cdot 10^{11}$$

The stiffness in the fiber direction is 150 GPa.

Now an attempt is made to model the material after the interface has failed. The debonded moduli are labeled IF for interface failed. The volume fraction for our material is Vf = 0.35. Using the Halpin-Tsai equations gives E1IF = 49 GPa and Poisson's ratio v12IF = .195. Now the other two properties are found and we calculate a new stiffness matrix qIF.

$$Gm := 29.2 \cdot 10^9 \qquad Gf := 0 \qquad \text{Using zeta = 1 for G12}$$

$$G12IF := Gm \cdot \frac{(Gf + Gm) + (Gf - Gm) \cdot .35}{(Gf + Gm) - (Gf - Gm) \cdot .35}$$

$$G12IF = 1.406 \cdot 10^{10}$$

$$Ef := 0 \qquad Em := 76 \cdot 10^9 \qquad \text{Using zeta = 2 for } E2$$

$$E2IF := Em \cdot \frac{(Ef + 2 \cdot Em) + (Ef - Em) \cdot 2 \cdot .35}{(Ef + 2 \cdot Em) - (Ef - Em) \cdot .35} \qquad E2IF = 4.204 \cdot 10^{10}$$

$$E1IF := 49 \cdot 10^9$$

$$\text{use} \quad E2IF := 42 \cdot 10^9 \qquad \text{and} \quad v12IF := 0.195$$

$$SIF := \begin{bmatrix} \dfrac{1}{E1IF} & \dfrac{-v12IF}{E1IF} & 0 \\ \dfrac{-v12IF}{E1IF} & \dfrac{1}{E2IF} & 0 \\ 0 & 0 & \dfrac{1}{G12IF} \end{bmatrix}$$

120

$$qIF := SIF^{-1}$$

$$\theta := \frac{\pi}{4} \qquad qIF45 := t(\theta)^{-1} \cdot qIF \cdot \left[t(\theta)^T {}^{-1} \right]$$

$$\theta := \frac{-\pi}{4} \qquad qIFm45 := t(\theta)^{-1} \cdot qIF \cdot \left[t(\theta)^T {}^{-1} \right]$$

$$\theta := \frac{\pi}{2} \qquad qIF90 := t(\theta)^{-1} \cdot qIF \cdot \left[t(\theta)^T {}^{-1} \right]$$

All the plies except the 0 degree ply are modeled qIF.

a := d2·(q + qIF45 + qIFm45 + qIF90)

i := qIF45   j := qIFm45

$$d := \frac{2}{3} \cdot \left[\left[d4^3 - d3^3 \right] \cdot q + \left[d3^3 - d2^3 \right] \cdot i + \left[d2^3 - d1^3 \right] \cdot j + d1^3 \cdot qIF90 \right]$$

big1 := augment(a,b)   big2 := augment(b,d)

big := augment(big1^T,big2^T)

$$big = \begin{bmatrix} 1.52 \cdot 10^8 & 3.41 \cdot 10^7 & -1.91 \cdot 10^{-10} & 0 & 0 & 0 \\ 3.41 \cdot 10^7 & 1.27 \cdot 10^8 & 3.94 \cdot 10^{-10} & 0 & 0 & 0 \\ -1.91 \cdot 10^{-10} & 3.94 \cdot 10^{-10} & 4.6 \cdot 10^7 & 0 & 0 & 0 \\ 0 & 0 & 0 & 69.25 & 14.31 & 0.17 \\ 0 & 0 & 0 & 14.31 & 51.29 & 0.17 \\ 0 & 0 & 0 & 0.17 & 0.17 & 18.25 \end{bmatrix}$$

$$NM := \begin{bmatrix} 165 \cdot 10^6 \cdot .001829 \\ 0 \\ 0 \\ 0 \\ 0 \\ 0 \end{bmatrix}$$

$$\epsilon := big^{-1} \cdot NM$$

121

$$\epsilon = \begin{bmatrix} 0.00212 \\ -5.69099 \cdot 10^{-4} \\ 0 \\ 0 \\ 0 \\ 0 \end{bmatrix}$$

$$E := 165 \cdot \frac{10^6}{.00212} \qquad E = 7.783 \cdot 10^{10}$$

So the expected modulus after debonding is about 80 GPa.

To be complete, the calculation of the laminate modulus with only the 90 degree plies debonded is included. Obviously, this results in a higher value.

This sets the values of the 45 degree plies back to bonded values.

$$a := d2 \cdot (q + qbar45 + qbarm45 + qIF90)$$

Just to make the equation fit on one line use qb and hb from above.

$$d := \frac{2}{3} \cdot \left[\left[d4^3 - d3^3 \right] \cdot q + \left[d3^3 - d2^3 \right] \cdot qb + \left[d2^3 - d1^3 \right] \cdot hb + d1^3 \cdot qIF90 \right]$$

big1 := augment(a,b)

big2 := augment(b,d)

big := augment(big1^T,big2^T)

$$\epsilon := big^{-1} \cdot NM$$

$$\epsilon = \begin{bmatrix} 0.00131 \\ -4.27493 \cdot 10^{-4} \\ 0 \\ 0 \\ 0 \\ 0 \end{bmatrix}$$

$$E := \frac{165 \cdot 10^6}{.00131} \qquad E = 1.26 \cdot 10^{11}$$

This is well above the experimental values.

Total discount simply sets the off axis plies to be discounted equal to 0. This calculation resulted in values of 115 GPa for only the 90 degree plies discounted and 48 GPa for all off axis plies discounted.

122

APPENDIX B

HIGH TEMPERATURE MODULUS FOR LAMINATE

Engineering Constants for as delivered SCS-6/Beta '21-S

$E1 := 164 \cdot 10^9 \qquad E2 := 111 \cdot 10^9 \qquad v12 := .28 \quad G12 := 37 \cdot 10^9$

$$S := \begin{bmatrix} \dfrac{1}{E1} & \dfrac{-v12}{E1} & 0 \\ \dfrac{-v12}{E1} & \dfrac{1}{E2} & 0 \\ 0 & 0 & \dfrac{1}{G12} \end{bmatrix} \qquad q := S^{-1}$$

$$q = \begin{bmatrix} 1.732 \cdot 10^{11} & 3.282 \cdot 10^{10} & 0 \\ 3.282 \cdot 10^{10} & 1.172 \cdot 10^{11} & 0 \\ 0 & 0 & 3.7 \cdot 10^{10} \end{bmatrix}$$

Now the q matrix is rotated to match the other lamina.

$$\theta := \dfrac{\pi}{4} \qquad t(\theta) := \begin{bmatrix} \cos(\theta)^2 & \sin(\theta)^2 & 2 \cdot \sin(\theta) \cdot \cos(\theta) \\ \sin(\theta)^2 & \cos(\theta)^2 & -2 \cdot \sin(\theta) \cdot \cos(\theta) \\ -\sin(\theta) \cdot \cos(\theta) & \sin(\theta) \cdot \cos(\theta) & \cos(\theta)^2 - \sin(\theta)^2 \end{bmatrix}$$

$$qbar45 := t(\theta)^{-1} \cdot q \cdot \left[t(\theta)^{T^{-1}} \right]$$

$$\theta := \dfrac{-\pi}{4} \qquad qbarm45 := t(\theta)^{-1} \cdot q \cdot \left[t(\theta)^{T^{-1}} \right]$$

$$\theta := \dfrac{\pi}{2}$$

$$qbar90 := t(\theta)^{-1} \cdot q \cdot \left[t(\theta)^{T^{-1}} \right]$$

$a := .000457 \cdot (q + qbar45 + qbarm45 + qbar90)$

$$b := \begin{bmatrix} 0 & 0 & 0 \\ 0 & 0 & 0 \\ 0 & 0 & 0 \end{bmatrix} \qquad a = \begin{bmatrix} 2.479 \cdot 10^8 & 7.754 \cdot 10^7 & -2.911 \cdot 10^{-10} \\ 7.754 \cdot 10^7 & 2.479 \cdot 10^8 & 1.858 \cdot 10^{-9} \\ -2.911 \cdot 10^{-10} & 1.858 \cdot 10^{-9} & 8.518 \cdot 10^7 \end{bmatrix}$$

Now an attempt is made to model the material after the interface has failed. The debonded moduli are labeled IF for interface failed. The volume fraction for our material is Vf = 0.35. Using the Halpin-Tsai equations gives E1IF = 38 GPa and Poisson's ratio v12IF = .2. Now the other two properties are found and we calculate a new stiffness matrix qIF. The equations for

$Gm := 22 \cdot 10^9$ $Gf := 0$ Using zeta = 1 for G12

$$G12IF := Gm \cdot \frac{(Gf + Gm) + (Gf - Gm) \cdot .35}{(Gf + Gm) - (Gf - Gm) \cdot .35}$$

$$G12IF = 1.059 \cdot 10^{10}$$

$Ef := 0$ $Em := 40 \cdot 10^9$ Using zeta = 2 for E2

$$E2IF := Em \cdot \frac{(Ef + 2 \cdot Em) + (Ef - Em) \cdot 2 \cdot .35}{(Ef + 2 \cdot Em) - (Ef - Em) \cdot .35}$$

$$E2IF = 2.213 \cdot 10^{10}$$

$E1IF := 38 \cdot 10^9$

use $E2IF := 22 \cdot 10^9$ and $v12IF := 0.2$

$$SIF := \begin{bmatrix} \dfrac{1}{E1IF} & \dfrac{-v12IF}{E1IF} & 0 \\ \dfrac{-v12IF}{E1IF} & \dfrac{1}{E2IF} & 0 \\ 0 & 0 & \dfrac{1}{G12IF} \end{bmatrix}$$

$qIF := SIF^{-1}$

$\theta := \dfrac{\pi}{4}$ $qIF45 := t(\theta)^{-1} \cdot qIF \cdot \left[t(\theta)\tau^{-1} \right]$

$\theta := \dfrac{-\pi}{4}$ $qIFm45 := t(\theta)^{-1} \cdot qIF \cdot \left[t(\theta)\tau^{-1} \right]$

$\theta := \dfrac{\pi}{2}$ $qIF90 := t(\theta)^{-1} \cdot qIF \cdot \left[t(\theta)\tau^{-1} \right]$

124

To be complete, the calculation of the laminate modulus with only the 90 degree plies debonded is included. Obviously, this results in a higher value.

q4 := qbar45   i := qbarm45

Sets the values of the 45 degree plies back to the original properties.

a := d2·(q + qbar45 + qbarm45 + qIF90)

$$d := \frac{2}{3} \cdot \left[\left[d4^3 - d3^3 \right] \cdot q + \left[d3^3 - d2^3 \right] \cdot qbar45 + \left[d2^3 - d1^3 \right] \cdot qbarm45 + d1^3 \cdot qIF90 \right]$$

big1 := augment(a,b)

big2 := augment(b,d)

big := augment(big1^T,big2^T)

ϵ := big^{-1}·NM

$$\epsilon = \begin{bmatrix} 0.00166 \\ -5.73244 \cdot 10^{-4} \\ 0 \\ 0 \\ 0 \\ 0 \end{bmatrix}$$

$$E := \frac{165 \cdot 10^6}{.00152} \qquad E = 1.086 \cdot 10^{11}$$

These are all above the experimental modulus. The matrix stiffness used may be too high a value or the material may be affected by the rapid temperature change.

126

HIGH TEMPERATURE MODULUS FOR LAMINATE

This appendix shows that some of the off-axis plies must be debonded before the high temperature tensile tests begin. The same calculation which was used for the first two appendices shows that the matrix modulus must be only 7 GPa for the calculated modulus to match the experimental modulus.

Engineering Constants for 650 C as-delivered SCS-6/Beta 21-S to match the initial modulus of only 70 GPa.

$$E1 := 156 \cdot 10^9 \quad E2 := 18 \cdot 10^9 \quad v12 := .28 \quad G12 := 13 \cdot 10^9$$

$$S := \begin{bmatrix} \dfrac{1}{E1} & \dfrac{-v12}{E1} & 0 \\ \dfrac{-v12}{E1} & \dfrac{1}{E2} & 0 \\ 0 & 0 & \dfrac{1}{G12} \end{bmatrix} \qquad q := S^{-1}$$

$$q = \begin{bmatrix} 1.574 \cdot 10^{11} & 5.086 \cdot 10^9 & 0 \\ 5.086 \cdot 10^9 & 1.816 \cdot 10^{10} & 0 \\ 0 & 0 & 1.3 \cdot 10^{10} \end{bmatrix}$$

Now the q matrix is rotated to match the other lamina.

$$\theta := \dfrac{\pi}{4} \qquad t(\theta) := \begin{bmatrix} \cos(\theta)^2 & \sin(\theta)^2 & 2 \cdot \sin(\theta) \cdot \cos(\theta) \\ \sin(\theta)^2 & \cos(\theta)^2 & -2 \cdot \sin(\theta) \cdot \cos(\theta) \\ -\sin(\theta) \cdot \cos(\theta) & \sin(\theta) \cdot \cos(\theta) & \cos(\theta)^2 - \sin(\theta)^2 \end{bmatrix}$$

$$qbar45 := t(\theta)^{-1} \cdot q \cdot \left[t(\theta)^{T^{-1}} \right]$$

$$\theta := \dfrac{-\pi}{4} \qquad qbarm45 := t(\theta)^{-1} \cdot q \cdot \left[t(\theta)^{T^{-1}} \right]$$

$$\theta := \dfrac{\pi}{2} \qquad qbar90 := t(\theta)^{-1} \cdot q \cdot \left[t(\theta)^{T^{-1}} \right]$$

$$a := .000457 \cdot (q + qbar45 + qbarm45 + qbar90)$$

$$b := \begin{bmatrix} 0 & 0 & 0 \\ 0 & 0 & 0 \\ 0 & 0 & 0 \end{bmatrix} \qquad a = \begin{bmatrix} 1.346 \cdot 10^{8} & 3.521 \cdot 10^{7} & 3.617 \cdot 10^{-10} \\ 3.521 \cdot 10^{7} & 1.346 \cdot 10^{8} & 3.537 \cdot 10^{-9} \\ 3.617 \cdot 10^{-10} & 3.537 \cdot 10^{-9} & 4.968 \cdot 10^{7} \end{bmatrix}$$

Now we need the d matrix and to make the equation all fit on one line we will define some coefficients. This also converts the distances from inches to meters.

$$d4 := \frac{.036}{39.37} \qquad d3 := \frac{.027}{39.37} \qquad d2 := \frac{.018}{39.37} \qquad d1 := \frac{.009}{39.37}$$

qb := qbar45   hb := qbarm45   fb := qbar90

$$d := \frac{2}{3} \cdot \left[\left[d4^{3} - d3^{3} \right] \cdot q + \left[d3^{3} - d2^{3} \right] \cdot qb + \left[d2^{3} - d1^{3} \right] \cdot hb + d1^{3} \cdot fb \right]$$

$$d = \begin{bmatrix} 58.842 & 8.464 & 3.327 \\ 8.464 & 18.914 & 3.327 \\ 3.327 & 3.327 & 12.497 \end{bmatrix}$$

big1 := augment(a,b)   big2 := augment(b,d)

big := augment(big1^{T},big2^{T})

This matrix represents the laminate stiffness.

$$big = \begin{bmatrix} 1.35 \cdot 10^{8} & 3.52 \cdot 10^{7} & 3.62 \cdot 10^{-10} & 0 & 0 & 0 \\ 3.52 \cdot 10^{7} & 1.35 \cdot 10^{8} & 3.54 \cdot 10^{-9} & 0 & 0 & 0 \\ 3.62 \cdot 10^{-10} & 3.54 \cdot 10^{-9} & 4.97 \cdot 10^{7} & 0 & 0 & 0 \\ 0 & 0 & 0 & 58.84 & 8.46 & 3.33 \\ 0 & 0 & 0 & 8.46 & 18.91 & 3.33 \\ 0 & 0 & 0 & 3.33 & 3.33 & 12.5 \end{bmatrix}$$

$$NM := \begin{bmatrix} 165 \cdot 10^{6} \cdot .001829 \\ 0 \\ 0 \\ 0 \\ 0 \\ 0 \end{bmatrix}$$

128

$$\epsilon := big^{-1} \cdot NM$$

$$\epsilon = \begin{bmatrix} 0.00241 \\ -6.29928 \cdot 10^{-4} \\ 0 \\ 0 \\ 0 \\ 0 \end{bmatrix}$$

$$E := 165 \cdot \frac{10^6}{.00241} \qquad E = 6.846 \cdot 10^{10}$$

The stiffness in the fiber direction is 70 GPa.

The calculations below were used to obtain the matrix values used for the calculation of the lamina and laminate moduli. Gm and Em were found by iterating and the final values to obtain the laminate modulus of 70 GPa are shown below.

$$Gm := 7 \cdot 10^9$$

$$Gf := 160 \cdot 10^9 \qquad \text{Using zeta = 1 for G12}$$

$$G12 := Gm \cdot \frac{(Gf + Gm) + (Gf - Gm) \cdot .35}{(Gf + Gm) - (Gf - Gm) \cdot .35}$$

$$G12 = 1.361 \cdot 10^{10}$$

$$Em := 7 \cdot 10^9 \qquad Ef := 414 \cdot 10^9 \qquad \text{Using zeta = 2 for E12}$$

$$E2 := Em \cdot \frac{(Ef + Em) + 2 \cdot (Ef - Em) \cdot .35}{(Ef + Em) - (Ef - Em) \cdot .35} \qquad E2 = 1.774 \cdot 10^{10}$$

Only values as small as this for the moduli of the matrix result in a calculated laminate moldulus which comes close to the experimental modulus.

APPENDIX D

WHITNEY-NUISMER AND TAN FWC CALCULATIONS

The calculation of the Whitney-Nuismer point stress failure prediction values was done using a spreadsheet. A short discussion of the equations used is followed by a sample spreadsheet file.

The basic idea behind the point stress prediction is that a critical distance exists as a material property (21). The critical distance is measured from the edge of the hole or crack to the critical point. Once this critical point reaches the unnotched failure stress, the composite will fail. The critical distance is called d_0 (21). Whitney chose to nondimensionalize the equations using the ratio between the radius (R) and the sum of R and d_0.

$$\xi_1 = \frac{R}{R+d_o} \tag{9}$$

This ratio is then used to compute the inverse of the SCF using the notched strength (σ_N) and the unnotched strength (σ_0). This ratio is for an infinite plate and applies to an isotropic material or a quasi-isotropic lay-up

of a composite.

$$\frac{\sigma_N}{\sigma_o} = \frac{2}{\left(2 + \xi_1^2 + 3\xi_1^4\right)}$$ (10)

When the lay-up is not quasi-isotropic, as the material for this study was after debonding occurred, a term is subtracted to account for the change in SCF due to anisotropy. The equation then becomes

$$\frac{\sigma_N}{\sigma_o} = \frac{2}{\left(2 + \xi_1^2 + 3\xi_1^4\right)} = (SCF-3)\left(5\xi_1^6 - 7\xi_1^8\right)$$ (11)

All these values are for infinite width so the experimental data must be converted to infinite width for an appropriate comparison. Tan developed a FWC for anisotropic plates using a complex variable method (20). The final equation for a circular hole is given below.

$$\frac{K_T^\infty}{K_T} = \frac{3\,(1 - 2a/W)}{2 + (1 - 2a/W)^3} + \frac{1}{2}\left(\frac{2a}{W}M\right)^6 (K_T^\infty - 3)\left[1 - \left(\frac{2a}{W}M\right)^2\right]$$ (12)

where

$$M^2 = \frac{\sqrt{1-8\left[\dfrac{3(1-2a/W)}{2+(1-2a/W)^3} - 1\right]} - 1}{2(2a/W)^2} \qquad (13)$$

and

$$K_T^\infty = 1 + \frac{1}{\lambda}\sqrt{\frac{2}{A_{22}}\left(\sqrt{A_{11}A_{22}} - A_{12} + \frac{A_{11}A_{22}-A_{12}^2}{2A_{66}}\right)} \qquad (14)$$

K_T^∞ is the theoretical stress concentration for an infinite plate discussed earlier. Using these equations the following values are computed for the room temperature debonded SCF of 3.18.

When a least squares fit was applied to this data a value of 0.955 was obtained for d_0.

When the SCF is 3, a closed form solution is available (24). Since the stress concentration is close to 3 for this study the closed form solution was applied to the same data shown above.

The equation is

$$R = d_0 \left\{ \sqrt{6}\left[-1+\left(1-24\left(1-\frac{\sigma_0}{\sigma_N^\infty}\right)^{\frac{1}{2}}\right)\right]^{-\frac{1}{2}} - 1 \right\}^{-1} \qquad (15)$$

Table VII   Sample Data From Whitney-Nuismer Calculation

RADIUS	WHITNEY	EXPER DATA	FWC
0	1	1.0080	1
0	1	0.9924	1
0.627	0.8976	0.8821	1.0102
0.648	0.8927	0.8575	1.0112
1.549	0.7146	0.6978	1.0700
1.600	0.7069	0.7119	1.0730
1.892	0.6673	0.6817	1.1124
2.578	0.5973	0.6358	1.2374
2.604	0.5952	0.5879	1.2455

This equation was solved for d_o and the results of all hole sizes were averaged. The result was 0.962 mm. This value was slightly larger than the 0.955 figure obtained by the least squares method. The other d_o values were computed only by the least squares method described above.

REPORT DOCUMENTATION PAGE

Form Approved
OMB No 0704-0188

1. AGENCY USE ONLY (Leave blank)	2. REPORT DATE December 1991	3. REPORT TYPE AND DATES COVERED Master's Thesis

4. TITLE AND SUBTITLE

TENSILE STRENGTH CHARACTERIZATION OF A METAL MATRIX COMPOSITE WITH CIRCULAR HOLES

5. FUNDING NUMBERS

6. AUTHOR(S)

JEFFREY RATTRAY, Captain, USAF

7. PERFORMING ORGANIZATION NAME(S) AND ADDRESS(ES)

Air Force Institute of Technology, WPAFB OH 45433-6583

8. PERFORMING ORGANIZATION REPORT NUMBER

AFIT/GAE/ENY/91D-24

9. SPONSORING / MONITORING AGENCY NAME(S) AND ADDRESS(ES)

Dr. Ted Nicholas
WL/MLLN
WPAFB, OH 45433

10. SPONSORING / MONITORING AGENCY REPORT NUMBER

11. SUPPLEMENTARY NOTES

12a. DISTRIBUTION / AVAILABILITY STATEMENT

Approved for public release; distribution unlimited

12b. DISTRIBUTION CODE

13. ABSTRACT (Maximum 200 words)

Static tensile testing conducted at room temperature and $650^{\circ}C$ shows notch sensitivity for a quasi-isotropic lay-up of a titanium alloy metal matrix composite. The specific material used was SCS-6/Beta 21S. Some unnotched specimens were tested and then the diameter-to-width ratio was varied from 0.1 to 0.4. The room temperature unnotched strength is 840 MPa, and the strength falls to less than half this value at $650^{\circ}C$. The off-axis plies of the $[0,\pm45,90]_s$ lay-up exhibit debonding of the fibers from the matrix at only ten percent of failure stress. This debonding is shown with acetate replicas and acoustic emission. By modeling the debonded plies with the Halpin-Tsai equations, a modulus is calculated for the debonded material which correlates very well with the experimental modulus. A fiber dominated failure exists at both temperatures, but the fiber pullout exists only at $650^{\circ}C$. Etching away the matrix from the 0° fibers showed a small area near the hole where fibers were damaged. The size of this damage zone correlated very well with the critical distance for the Whitney-Nuismer Point Stress failure prediction method.

14. SUBJECT TERMS

Titanium, Metal Matrix Composite, Silicon Carbide Fibers
Tensile Testing, Strength, Composite Materials

15. NUMBER OF PAGES

147

16. PRICE CODE

17. SECURITY CLASSIFICATION OF REPORT	18. SECURITY CLASSIFICATION OF THIS PAGE	19. SECURITY CLASSIFICATION OF ABSTRACT	20. LIMITATION OF ABSTRACT
Unclassified	Unclassified	Unclassified	UL

GENERAL INSTRUCTIONS FOR COMPLETING SF 298

The Report Documentation Page (RDP) is used in announcing and cataloging reports. It is important that this information be consistent with the rest of the report, particularly the cover and title page. Instructions for filling in each block of the form follow. It is important to **stay within the lines to meet optical scanning requirements.**

Block 1. Agency Use Only (Leave Blank)

Block 2. Report Date. Full publication date including day, month, and year, if available (e.g. 1 Jan 88). Must cite at least the year.

Block 3. Type of Report and Dates Covered. State whether report is interim, final, etc. If applicable, enter inclusive report dates (e.g. 10 Jun 87 - 30 Jun 88).

Block 4. Title and Subtitle. A title is taken from the part of the report that provides the most meaningful and complete information. When a report is prepared in more than one volume, repeat the primary title, add volume number, and include subtitle for the specific volume. On classified documents enter the title classification in parentheses.

Block 5. Funding Numbers. To include contract and grant numbers; may include program element number(s), project number(s), task number(s), and work unit number(s). Use the following labels:

C	- Contract	PR	- Project
G	- Grant	TA	- Task
PE	- Program Element	WU	- Work Unit Accession No.

Block 6. Author(s). Name(s) of person(s) responsible for writing the report, performing the research, or credited with the content of the report. If editor or compiler, this should follow the name(s).

Block 7. Performing Organization Name(s) and Address(es). Self-explanatory.

Block 8. Performing Organization Report Number. Enter the unique alphanumeric report number(s) assigned by the organization performing the report.

Block 9. Sponsoring/Monitoring Agency Names(s) and Address(es). Self-explanatory.

Block 10. Sponsoring/Monitoring Agency. Report Number. (If known)

Block 11. Supplementary Notes. Enter information not included elsewhere such as: Prepared in cooperation with...; Trans. of ..., To be published in .... When a report is revised, include a statement whether the new report supersedes or supplements the older report.

Block 12a. Distribution/Availablity Statement. Denote public availability or limitation. Cite any availability to the public. Enter additional limitations or special markings in all capitals (e.g. NOFORN, REL, ITAR)

DOD	-	See DoDD 5230.24, "Distribution Statements on Technical Documents."
DOE	-	See authorities
NASA	-	See Handbook NHB 2200.2.
NTIS	-	Leave blank.

Block 12b. Distribution Code.

DOD	-	DOD - Leave blank
DOE	-	DOE - Enter DOE distribution categories from the Standard Distribution for Unclassified Scientific and Technical Reports
NASA	-	NASA - Leave blank
NTIS	-	NTIS - Leave blank.

Block 13. Abstract. Include a brief (Maximum 200 words) factual summary of the most significant information contained in the report.

Block 14. Subject Terms. Keywords or phrases identifying major subjects in the report.

Block 15. Number of Pages. Enter the total number of pages.

Block 16. Price Code. Enter appropriate price code (NTIS only).

Blocks 17. - 19. Security Classifications. Self-explanatory. Enter U.S. Security Classification in accordance with U.S. Security Regulations (i.e., UNCLASSIFIED). If form contains classified information, stamp classification on the top and bottom of the page.

Block 20. Limitation of Abstract. This block must be completed to assign a limitation to the abstract. Enter either UL (unlimited) or SAR (same as report). An entry in this block is necessary if the abstract is to be limited. If blank, the abstract is assumed to be unlimited.